

# Fiber-Shaped Electronic Devices

Azhar Fakharuddin,\* Haizeng Li,\* Francesco Di Giacomo, Tianyi Zhang, Nicola Gasparini,\* Abdulhakem Y. Elezzabi, Ankita Mohanty, Ananthakumar Ramadoss, JinKiong Ling, Anastasia Soultati, Marinos Tountas, Lukas Schmidt-Mende, Panagiotis Argitis, Rajan Jose, Mohammad Khaja Nazeeruddin, Abd Rashid Bin Mohd Yusoff,\* and Maria Vasilopoulou\*

Textile electronics embedded in clothing represent an exciting new frontier for modern healthcare and communication systems. Fundamental to the development of these textile electronics is the development of the fibers forming the cloths into electronic devices. An electronic fiber must undergo diverse scrutiny for its selection for a multifunctional textile, viz., from the material selection to the device architecture, from the wearability to mechanical stresses, and from the environmental compatibility to the end-use management. Herein, the performance requirements of fiber-shaped electronics are reviewed considering the characteristics of single electronic fibers and their assemblies in smart clothing. Broadly, this article includes i) processing strategies of electronic fibers with required properties from precursor to material, ii) the state-of-art of current fiber-shaped electronics emphasizing light-emitting devices, solar cells, sensors, nanogenerators, supercapacitors storage, and chromatic devices, iii) mechanisms involved in the operation of the above devices, iv) limitations of the current materials and device manufacturing techniques to achieve the target performance, and v) the knowledge gap that must be minimized prior to their deployment. Lessons learned from this review with regard to the challenges and prospects for developing fiber-shaped electronic components are presented as directions for future research on wearable electronics.

## 1. Introduction

The next generation of wearable electronics demands systems to be directly integrated onto a soft and curved human body covered with highly extensible skins (with an average elongation of 3–55%).<sup>[1–3]</sup> As a result, textile electronics has become a fast growing multibillion-dollar industry. The integration of electronic devices directly on the inner or outer surface of single fibers, which have typical thickness of several to tens of micrometers, have been recently reported. Fiber-shaped wearable electronics are flexible, bendable, lightweight, and conformable to conveniently integrate onto textile surfaces. Moreover, fiber-shaped electronic devices with shape-memory and self-healing ability and those with a possibility to be monolithically integrated with complementary devices have also been reported.<sup>[1,4–6]</sup> These are energy harvesting devices such as solar cells, piezoelectric and triboelectric nanogenerators (NGs),<sup>[7,8]</sup> energy storage devices (ESDs) including

Dr. A. Fakharuddin, Prof. L. Schmidt-Mende  
Department of Physics  
University of Konstanz  
78457 Konstanz, Germany  
E-mail: azhar-fakhar.uddin@uni-konstanz.de

Prof. H. Li  
Institute of Frontier and Interdisciplinarity Science  
Shandong University  
Qingdao 266237, China  
E-mail: haizeng@sdu.edu.cn

 The ORCID identification number(s) for the author(s) of this article can be found under <https://doi.org/10.1002/aenm.202101443>.

© 2021 The Authors. Advanced Energy Materials published by Wiley-VCH GmbH. This is an open access article under the terms of the Creative Commons Attribution-NonCommercial License, which permits use, distribution and reproduction in any medium, provided the original work is properly cited and is not used for commercial purposes.

DOI: 10.1002/aenm.202101443

Dr. F. Di Giacomo  
Centre for Hybrid and Organic Solar Energy (CHOSE)  
Department of Electronic Engineering  
University of Rome Tor Vergata  
Rome 00133, Italy

T. Zhang, Dr. N. Gasparini  
Department of Chemistry and Centre for Processable Electronics  
Imperial College London  
London W120BZ, UK  
E-mail: n.gasparini@imperial.ac.uk

Prof. A. Y. Elezzabi  
Ultrafast Optics and Nanophotonics Laboratory  
Department of Electrical and Computer Engineering  
University of Alberta  
Edmonton, Alberta T6G 2V4, Canada

A. Mohanty, Dr. A. Ramadoss  
School for Advanced Research in Petrochemicals  
Laboratory for Advanced Research in Polymeric Materials  
Central Institute of Petrochemicals Engineering and Technology  
Bhubaneswar, Odisha 751024, India

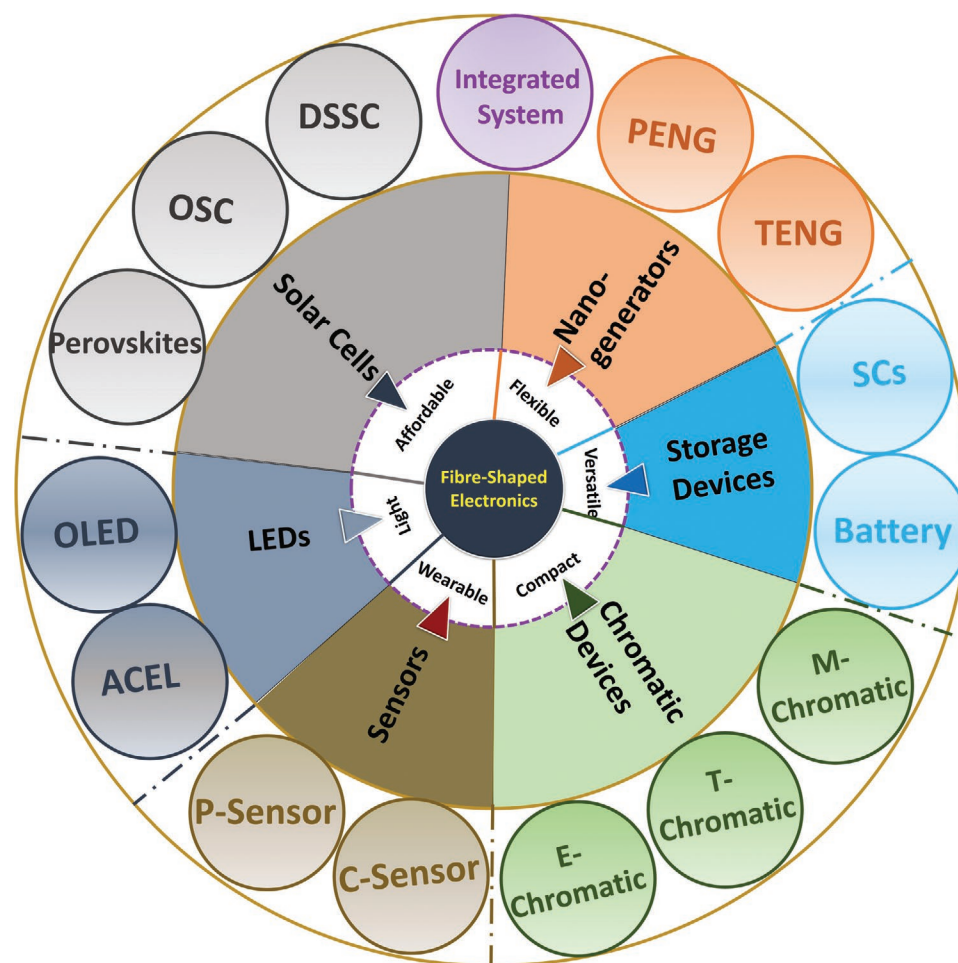


**Figure 1.** An overview of various fiber-based electronic devices discussed in this article. These devices are categorized as energy harvesting (solar cells and nanogenerators), energy storage (supercapacitors and batteries), and functional devices (sensors, light-emitting devices, and chromatic devices).

J.K. Ling, Prof. R. Jose  
Nanostructured Renewable Energy Material Laboratory  
Faculty of Industrial Sciences and Technology  
Universiti Malaysia Pahang  
Pahang Darul Makmur, Kuantan 26300, Malaysia  
Dr. A. Soutati, Dr. P. Argitis, Dr. M. Vasilopoulou  
Institute of Nanoscience and Nanotechnology  
National Center for Scientific Research Demokritos  
Agia Paraskevi, Attica 15341, Greece  
E-mail: m.vasilopoulou@inn.demokritos.gr  
Dr. M. Tountas  
Department of Electrical and Computer Engineering  
Hellenic Mediterranean University  
Estavromenos, Heraklion, Crete GR-71410, Greece  
Prof. M. K. Nazeeruddin  
Group for Molecular Engineering of Functional Materials  
Institute of Chemical Sciences and Engineering  
École Polytechnique Fédérale de Lausanne (EPFL)  
Rue de l'Industrie 17, Sion CH-1951, Switzerland  
Dr. A. R. B. Mohd Yusoff  
Department of Chemical Engineering  
Pohang University of Science and Technology  
(POSTECH)  
Pohang, Gyeongbuk 37673, Republic of Korea  
E-mail: abdrashid@postech.ac.kr

supercapacitors (SCs), and various types of batteries,<sup>[9,10]</sup> light-emitting devices,<sup>[11]</sup> and sensors, used in medical devices<sup>[12]</sup> and diagnostics, civil engineering, and fitness.<sup>[13,14]</sup>

Fiber structure and morphology are important because they set restrictions for the deposition of homogeneous layers onto their curvy surface. This makes controlling the microstructure and composition considerably essential. Compared with bulky electrodes in conventional devices, which are basically stabilized on a rigid substrate during the fabrication process, fiber electrodes with a certain degree of flexibility and robustness to withstand numerous deformations have not been completely achieved yet. Various materials such as metals, elastics covered with metals or composites formed between them, conductive polymers, graphene, carbon nanotubes (CNTs), and metal oxides have been used to fabricate conductive fiber-shaped electrodes.<sup>[15,16]</sup> However, imparting electronic functions to porous, highly deformable, and 3D fiber assemblies and maintaining them during wear represent great challenges in terms of the smart fiber properties and implementation in the electronic devices therein.

In this article, the recent advancements on fiber materials, fabrication techniques, structural design of the fibers, and their applications in a range of wearable electronic devices is reviewed (Figure 1). The performance requirements of fiber-based smart

wearable electronics, especially in terms of correlation among materials, fiber structures, and electronic mechanical functionalities are also elaborated. First, how a concise picture of the relationship between the structure and properties of fiber must be well understood before designing and fabricating fiber-based materials for wearable electronic applications is discussed (Section 2). Section 3 provides a brief overview of the flexible electronic yarn making techniques. Next, three main classes of fiber-shaped electronic devices, namely, energy harvesting, energy storage, and functional devices (Sections 4–7), were explored, with emphasis on the factors affecting their performance, and why it lags behind that of the state-of-the-art planar counterparts is explained. A difficult topic to tackle is the scalability of those electronic devices because making devices only up to several centimeters long is currently possible. Next, fiber-based integrated systems that are made from two or more electronic devices are discussed. Finally, the lessons learnt from this review is presented as outlook of the challenges and perspectives for the future development of fiber-shaped smart electronic devices to overcome the existing obstacles and toward their commercialization (Section 8).

## 2. Choice of Fiber Material and Intrinsic Properties

The intrinsic properties of fibers, such as its structure and morphology, are extremely important as they restrict deposition of homogeneous layers for subsequent device fabrication. This

makes controlling the morphology and composition of fibers essential. Given the high mechanical strength and the high electrical conductivity, stainless steel fibers were initially utilized as the core substrate for the fabrication of wearable electronics.<sup>[17]</sup> However, stainless steel fibers show poor softness and flexibility,<sup>[18]</sup> which significantly limit their weavability into textiles and stretchability for practical applications. Woven stainless steel filter meshes were found to be stretchable when being tailored along a direction of 45° to its weft or the warp.<sup>[19]</sup> For example, stretchable hybrid SCs were fabricated by knitting nonstretchable stainless steel fibers.<sup>[20]</sup> Such knitted networks could transform the angular elasticity of stainless steel meshes into the stretchability of textile electrodes and thus enable the assembly of stretchable solid-state hybrid SCs (Figure 2a). However, the stretchability of stainless steel filter meshes is limited ( $\leq 40\%$  strain). Furthermore, the usage of metals could cause a sensation of rigidity and stiffness when used in wearable electronics. Therefore, developing metal-free stretchable conductive fibers is considerably important.

To address the above-mentioned issues related to pure metal fibers as well as metal–elastomer composite fibers have become particularly attractive for wearable electronics because they show great improvement in flexibility while maintaining good conductivity. For instance, highly stretchable conductive fibers composed of silver nanowires (Ag NWs) and silver nanoparticles (Ag NPs) embedded in a styrene–butadiene–styrene elastomeric matrix have been reported.<sup>[21]</sup> Such fibers exhibit

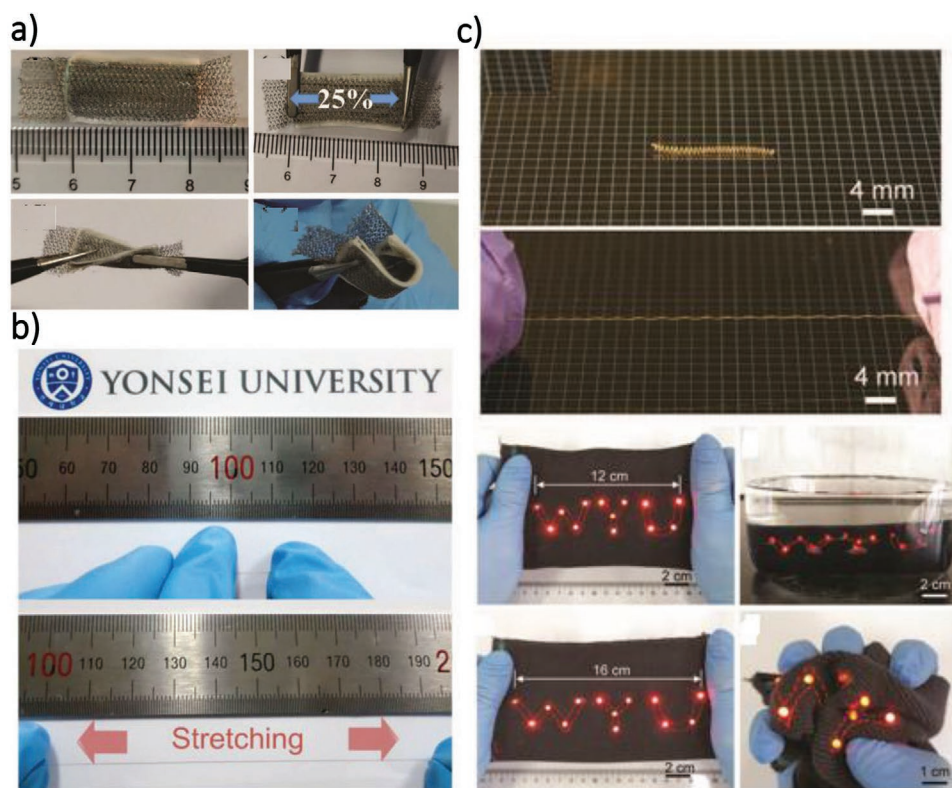


**Figure 2.** a) Stretchable solid-state hybrid supercapacitors using knitted stainless steel meshes. Reproduced with permission.<sup>[20]</sup> Copyright 2020, John Wiley & Sons. b) Stretchable conductive fibers composed of silver nanowires and silver nanoparticles embedded in a styrene–butadiene–styrene elastomeric matrix. Reproduced with permission.<sup>[21]</sup> Copyright 2015, John Wiley & Sons. c) Stretchable conductive fibers composed of elastic polyurethane fibers and conductive Cu fibers, and their demonstration for wearable electronics. Reproduced with permission.<sup>[22]</sup> Copyright 2020, John Wiley & Sons.

superior initial electrical conductivity ( $2450 \text{ S cm}^{-1}$ ) and elongation at break (900% strain) due to the high weight percentage of the conductive fillers and the use of a highly stretchable styrene-butadiene-styrene elastomer matrix, respectively (Figure 2b). Highly stretchable, conductive, and washable fibers that consisted of elastic polyurethane (PU) fibers and conductive Cu-based fibers have been also developed.<sup>[22]</sup> Such fibers have excellent mechanical and electrical properties and they could be readily integrated with fabrics and other functional components to build fabric-based wearable systems (Figure 2c).

Besides utilizing metal as the conductive component, conducting fibers have been developed using carbon-based materials. For example, stretchable conductive fibers were developed using reduced graphene oxide (rGO) as the conductive component and commercially available double-covered yarns as the core-substrate.<sup>[25]</sup> In addition, high-performance fibers were fabricated using a facile and inexpensive method that was based on layer-by-layer spray coating of PU and CNTs or graphene nanoribbons onto Kevlar fibers.<sup>[23]</sup> The spray-coated PU was used as the interlayer between the Kevlar fiber and carbon materials to bind the carbon materials to the Kevlar fiber. The strongly adhering single-walled CNT coatings yielded a durable conductivity of  $65 \text{ S cm}^{-1}$  without significant mechanical

degradation and they could be used as a conducting wire to light a light-emitting diode (LED) (Figure 3a,b). A superelastic and conductive fiber was also constructed by wrapping a flexible conductive CNT/polydimethylsiloxane (PDMS) composite yarn onto a polyester filament.<sup>[26]</sup> The fiber showed a high stretchability (165%), exceptional tensile force (660 cN), extraordinary antiabrasion ability, and remarkable electrical stability under various deformations. Apart from PDMS as the elastic component, cotton spandex could be used to fabricate conductive elastic fibers. For instance, CNT/cotton/spandex composite yarn was demonstrated using airfil spinning via dipping and drying carbon nanotubes into cotton rovings.<sup>[24]</sup> Such fibers showed excellent stretchability (200% strain) and it could be used as a strain sensor to accurately monitor real-time human motions (Figure 3c). Overall, although pure metal fibers showed superior electrical conductivity compared with metal-elastomer composite and carbon materials elastomer composite fibers, they suffer from poor stretchability and limited weavability resulting in a substantial challenge for the fabrication of stretchable electronic devices. As such, conductive fibers utilizing elastomers as the matrix are considered the most promising component for next-generation stretchable electronics.

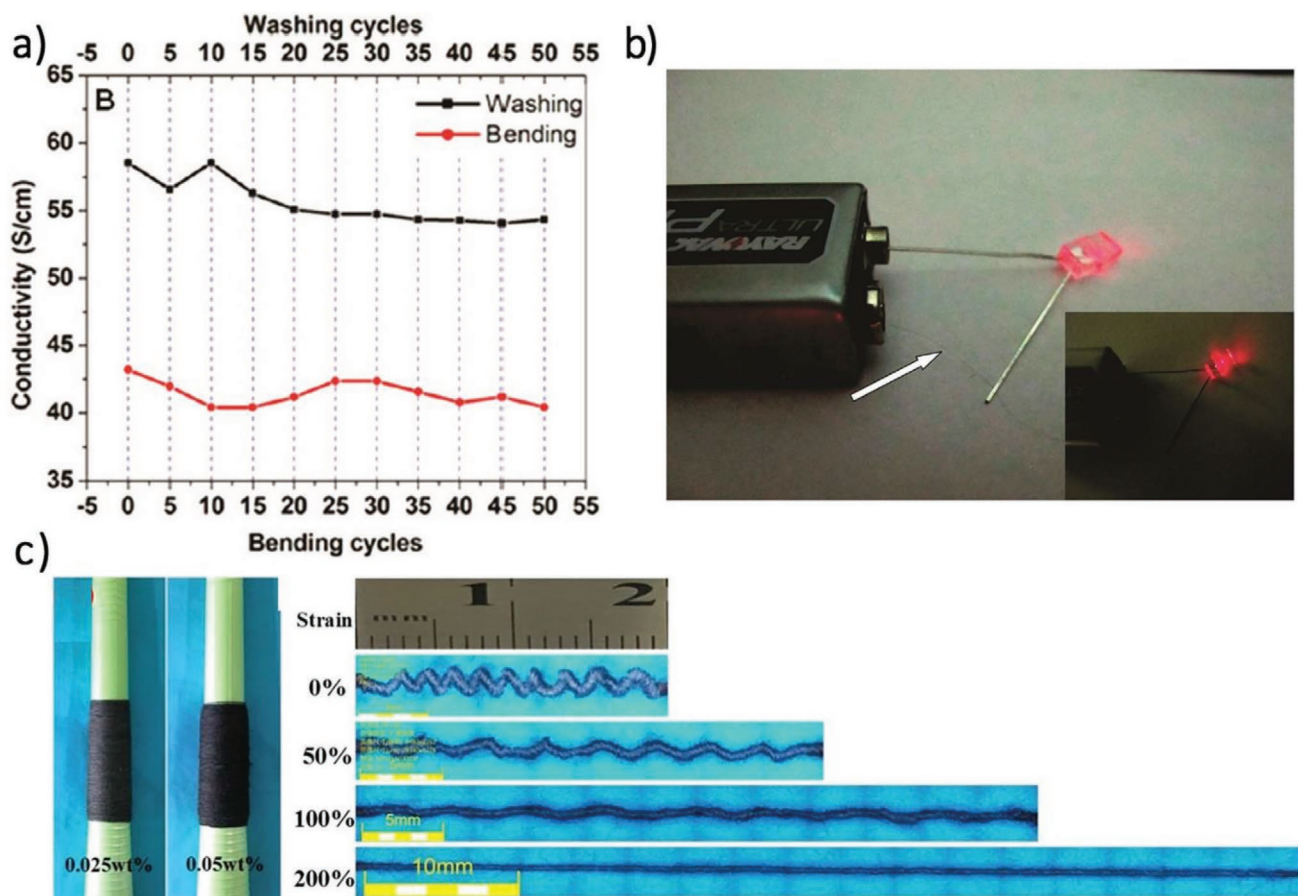


**Figure 3.** a) Electrical conductivity of the single-walled carbon nanotube-coated Kevlar fibers under different mechanical deformations. b) The demonstration of LED emission by using a single-walled carbon nanotube-coated Kevlar fiber. Reproduced with permission.<sup>[23]</sup> Copyright 2012, American Chemical Society. c) Photographs of the stretchable carbon nanotube/cotton/spandex composite yarn and the demonstration of stretchability. Reproduced with permission.<sup>[24]</sup> Copyright 2018, American Chemical Society.

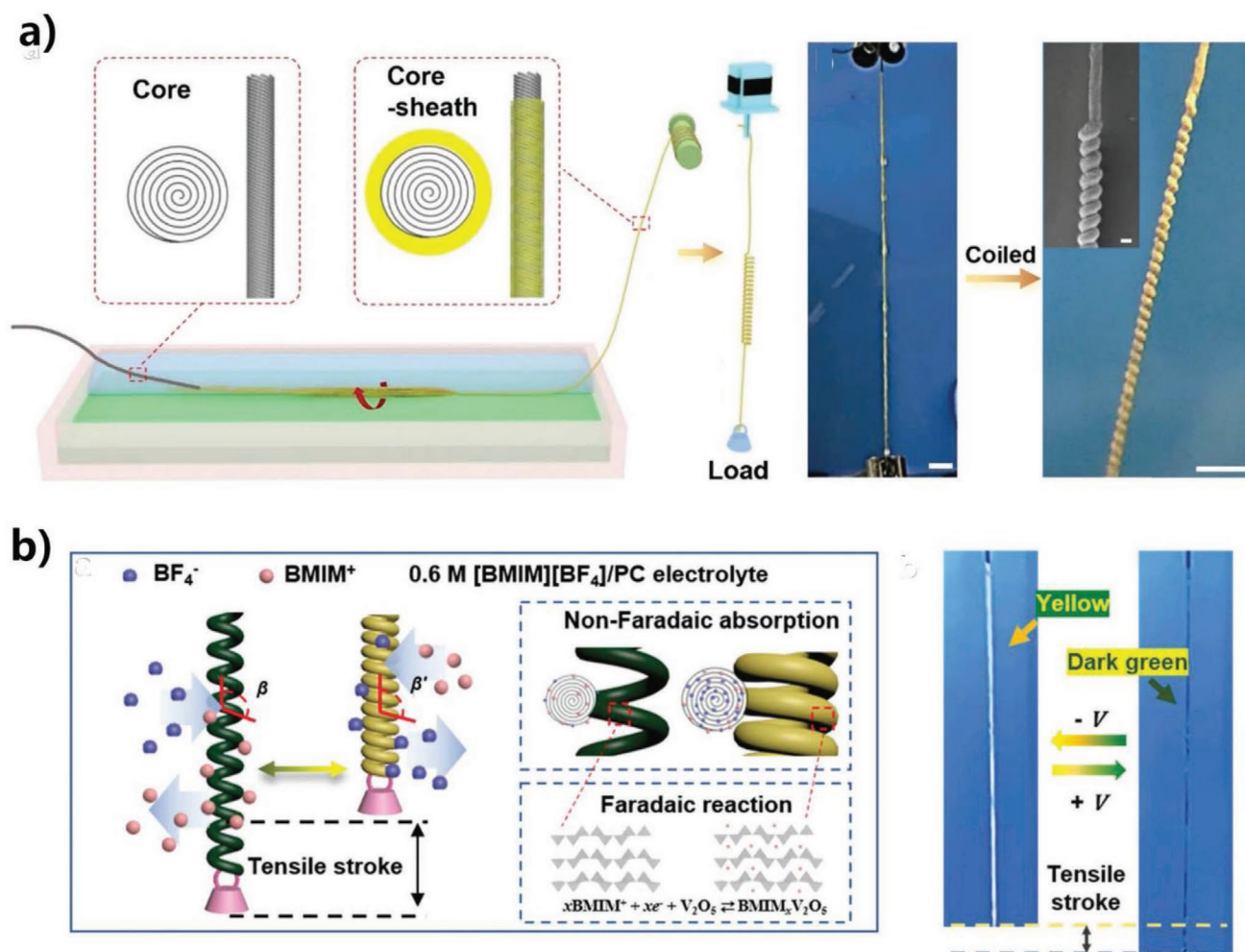


**Figure 4.** a) Fabrication process and structural characterization of the electrochromic fibers. b) Dual-responsive actuating/color-changing performance of the electrochromic fibers. Reproduced with permission.<sup>[27]</sup> Copyright 2021, The Royal Society of Chemistry.

The conductive fibers utilizing carbon materials as the conducting component enable an excellent conductivity along with good stretchability. Therefore, they can be further used for different fiber-shaped electronic devices. Li et al. utilized CNT as a core component for fabricating electrochromic fibers.<sup>[27]</sup> As shown in **Figure 4a**, a CNT fiber serves as the core when fabricating the V<sub>2</sub>O<sub>5</sub>-based electrochromic fibers. Due to the good conductivity and stretchability of the CNT fibers, such electrochromic fibers possess a good color switching between yellow and dark green, along with an actuating character (**Figure 4b**). In addition, conductive fibers can be used for various applications such as fiber-shaped LEDs, fiber-shaped solar cells (FSSCs), fiber-shaped sensors, fiber-shaped supercapacitors (FSCs) and batteries, and fiber-shaped chromatic devices, which are reviewed in respective sections as mentioned in Section 1.

### 3. Fabrication Methods and Assembly of Conductive Fibers

The fabrication methods of conductive fibers play an important role in determining their characteristics, cost, stability,

and scalability. They also govern the performance of the complete fiber-shaped device. In this section, various fabrication approaches are discussed with their relative merits and drawbacks (see brief description in **Table 1**).

#### 3.1. Dip-Coating Method

As pure metal fibers suffer from poor stretchability and weavability, metal-elastomer composite conductive fibers could be an alternative due to their exceptional stretchability and a good electrical conductivity. Among all the reported methods, dip-coating is the easiest to fabricate conductive fibers. **Figure 5a** represents a schematic of a three-step dip-coating process to fabricate the conductive fibers.<sup>[28]</sup> First, commercially available Twaron fibers were dipped into the poly(styrene-*block*-butadiene-styrene) (PSBS) solution to enhance the absorption of the Ag precursor. Second, after being dried, the SBS-coated fibers were immersed in a solution of the silver precursor. Finally, in the third step, the Ag precursor layer is reduced to silver by immersing the fibers into a reducing solution. Thus, an electrically conductive fiber was prepared. Another example of conductive fibers fabricated via dip-coating method is shown in



### 3.3. Continuous Spinning Method

Although the aforementioned dip-coating and spray coating methods could develop many different types of conductive fibers, the development of a continuously processed method (i.e., continuous spinning method) is more attractive due to its advantages, including the possibility of long fiber fabrication and commercialization potential. For example, a microfluidic-spinning method to fabricate conductive polyaniline-wrapped MWCNTs-rGO/thermoplastic PU (PANI/MWCNTs-rGO/

TPU) composite fibers were successfully demonstrated.<sup>[34]</sup> As schematically illustrated in **Figure 6a**, a mixture of MCNTs, rGO, and TPU was dissolved in *N,N*-dimethylformamide by vigorous stirring to form a uniform microfluidic-spinning precursor. Then, the precursor solution was extruded into a T-shape microfluidic chip as an interphase fluid, while the outer-phase channel was filled with pure water. Benefiting from a large specific surface area in the microfluidic chip, a fast exchange of solvents occurred between the pure water and the precursor on the interface and solid fibers. The diameter of

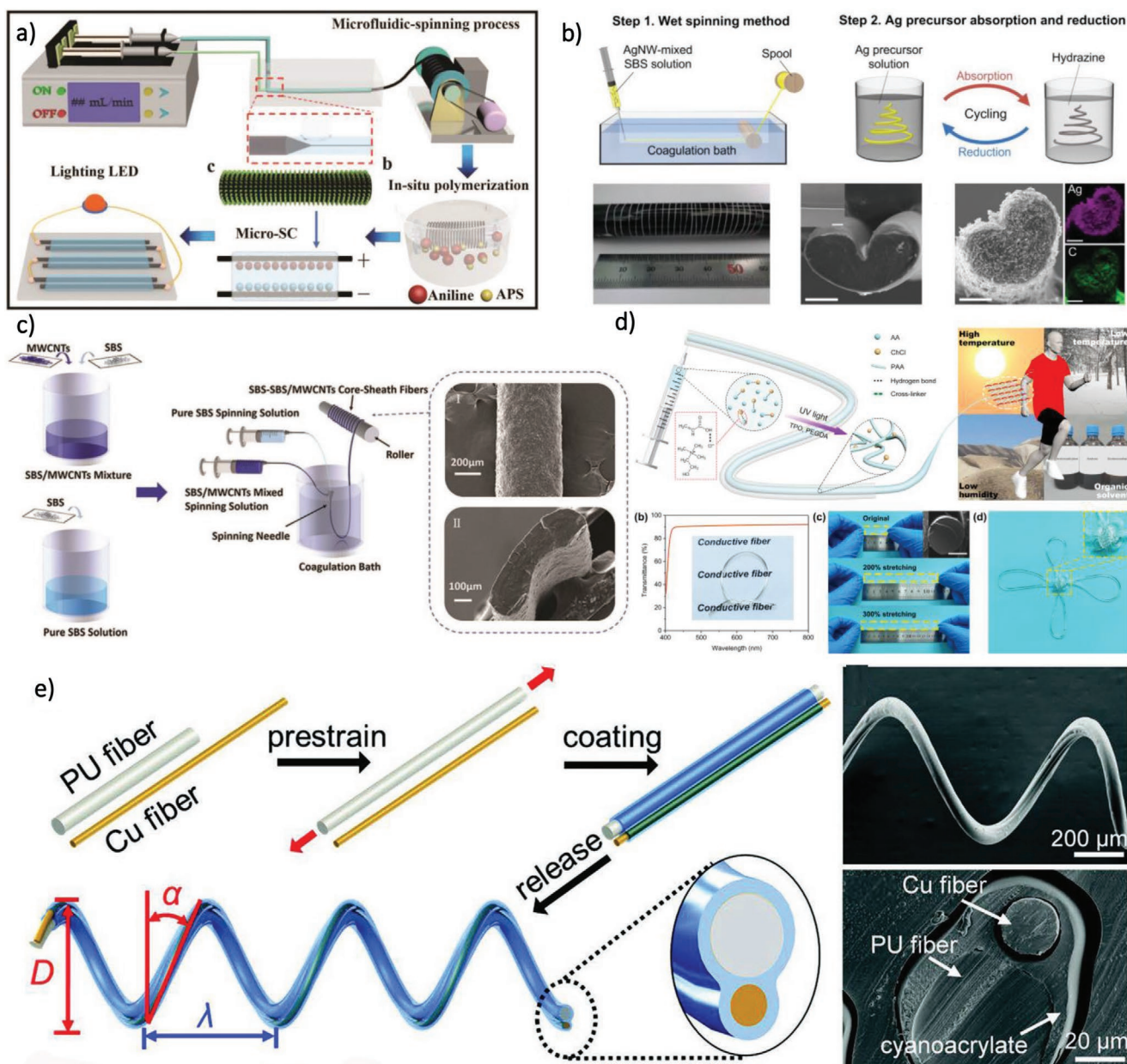


**Figure 6.** a) Schematic illustration of the microfluidic-spinning process. Reproduced with permission.<sup>[34]</sup> Copyright 2018, John Wiley & Sons. b) Schematic illustration of the wet spinning process for the stretchable conductive fiber.<sup>[21]</sup> Copyright 2015, John Wiley & Sons. c) Schematic illustration of the procedure for preparing conductive core–sheath fibers. Reproduced with permission.<sup>[35]</sup> Copyright 2021, John Wiley & Sons. d) Schematic illustration of fabrication and excellent properties of poly (polymerizable deep eutectic solvent (PDES)) fibers, including harsh environment tolerance, transparency, stretchability, and knittability. Reproduced with permission.<sup>[36]</sup> Copyright 2021, American Chemical Society. e) Schematic illustration of the fabrication process of the 3D helical fiber and the corresponding morphology of the fiber. Reproduced with permission.<sup>[22]</sup> Copyright 2020, John Wiley & Sons.

the as-prepared fibers could be controlled by choosing appropriate needles and thus the optimal electrical conductivity ( $874 \text{ S m}^{-1}$ ) can be obtained. The MCNTs-rGO/TPU composite fibers were then immersed into a solution containing acidic aniline monomers to prepare PANI-wrapped fibers and enhance the capacitance of the conductive fibers when used as electrodes for SCs. They exhibited good conductivity and outstanding flexibility, which enabled fiber assembly into wearable SCs.

Besides the carbon-based materials used in the precursor for fabricating conductive fibers, Ag NWs can also be used in the spinning precursor to fabricate stretchable conductive fibers. Lee et al. reported a wet spinning method for fabricating highly stretchable Ag NWs/Ag NPs embedded styrene-butadiene-styrene (SBS) composite fibers. The method involved two steps (Figure 6b): wet-spinning of Ag NW-SBS composite fibers followed by Ag NPs modification of the composite fibers. In the first step, Ag NWs were uniformly mixed with the SBS polymer solution and then the solution was injected in polyvinyl alcohol (PVA) coagulation liquid. The SBS polymer was precipitated immediately as the SBS was injected into the PVA bath. A 100 cm long conductive Ag NW-SBS fibers were successfully obtained and collected on a long cylindrical-shaped spool. A series of sequential processes were then conducted via dipping the fibers into Ag precursor for  $\text{Ag}^+$  absorption and hydrazine reduction, to further enhance the conductivity of the composite fibers. Another representative example regarding the wet spinning method for the fabrication of conductive fibers is shown in Figure 6c.<sup>[35]</sup> SBS solution was first prepared through dissolving SBS pellets in tetrahydrofuran, which served as a precursor to spin the core layer of the fibers. The outer layer of the fibers was prepared from the MWCNTs-SBS mixture suspension. After the coagulation process of the two precursor solutions through a coaxial needle occurred, the fibers were dried and collected on a roller. The as-prepared SBS-SBS/MWCNTs core-sheath fiber displayed outstanding sensing performance and excellent durability (5000 cycles at 10% strain).

Transparent ionic conductive fibers could be also prepared through a continuous spinning strategy.<sup>[36]</sup> As shown in Figure 6d, a spinning solution was prepared by heating a mixture of choline chloride (ChCl) and acrylic acid until a homogenous transparent solution was obtained. Afterward, *d*-phenyl(2,4,6-trimethylbenzoyl)phosphine oxide and poly(ethylene glycol) diacrylate, which serves as a photoinitiator and a crosslinker, respectively, were added into the cooled transparent solution. Then, the spinning solution was loaded into a syringe and injected into a silicone tube, which was exposed to ultraviolet light to trigger the polymerization. At last, an ionically conductive poly(polymerizable deep eutectic solvent) fiber was prepared after taking off the outer silicone tube. Such ionically conductive fibers possessed excellent transparency, high stretchability, and good knittability.

### 3.4. Assembly of Conductive Fibers

Different from the above-mentioned conductive fibers made via chemical transformation, some conductive fibers were

prepared via assembling the off-the-shelf components. The most frequently used strategy to assemble conductive fibers is through wrapping a fine metal wire onto an elastomer. For example, conductive 3D helical fibers were fabricated via the assembly of prestretched PU and Cu fibers.<sup>[22]</sup> This kind of conductive fibers used a highly stretchable PU fiber as an elastic substrate and a Cu fiber as a conductive material. Figure 6e schematically illustrates its fabrication process, where two steps are involved during the procedure. First, the PU fiber was prestretched by a large strain, firmly bonded to an intact Cu fiber via a fast-acting glue (i.e., cyanoacrylate), and then wrapped with the same glue. Then, the conductive 3D helical fiber was prepared via spontaneous relaxation process. As cyanoacrylate is very stable when exposed to moisture and household detergents, such conductive fibers could be used in washable and wearable electronics.

### 3.5. Assembly of 2D Stretchable Substrate

Considering wearable electronics could be viewed as functional textiles, they should potentially be fabricated directly on a 2D stretched substrate. For instance, a smart stretchable supercapacitor was fabricated by depositing conducting polymers (CPs) onto aligned CNT sheets. Figure 7a illustrates the fabrication process of the smart SC.<sup>[37]</sup> First, a stretchable PDMS film was prestretched. Then, a thin layer of aligned CNT sheet was paved onto the prestretched PDMS substrate to make a stretchable, electrically conducting film, followed by electrodeposition of PANI. The stretched electrode was then released and coated with a gel electrolyte. Finally, the stretchable SC was fabricated by assembling the two stretchable electrodes together. A similar pretrained strategy could be used to fabricate elastic transparent conductors. Moreover, a “balloon-blowing” method was developed to provide a multiaxial prestretch of the polymer substrate (i.e., polyacrylic ester) and an elastic transparent conductor was prepared by spraying a highly dispersed rGO solution onto the substrate (Figure 7b). Another representative example of the fabrication of stretchable conductors is shown in Figure 7c, where Ag NWs were spray-coated onto the prestretched PDMS substrate. Then, an electroluminescent device was developed when two pieces of the stretchable conductors were sandwiched as an electroluminescent unit. A notable detail that even though 2D stretchable substrates show a great potential in many applications, they still present challenges for successful utilization in wearable electronics. Most of the 2D stretchable substrates are dense polymer membranes, which suffer from low breathability for wearable electronics. As such, developing stretchable 2D substrates with high breathability is the next target for the wearable electronic community.

## 4. Fiber-Shaped Energy Harvesting Devices

Harvesting energy from the atmosphere and body motion are the most prominent ways. Solar cells are employed to harvest energy from sunlight whereas the energy from body motion can be harvesting via, for example, nanogenerators. In Sections 4.1

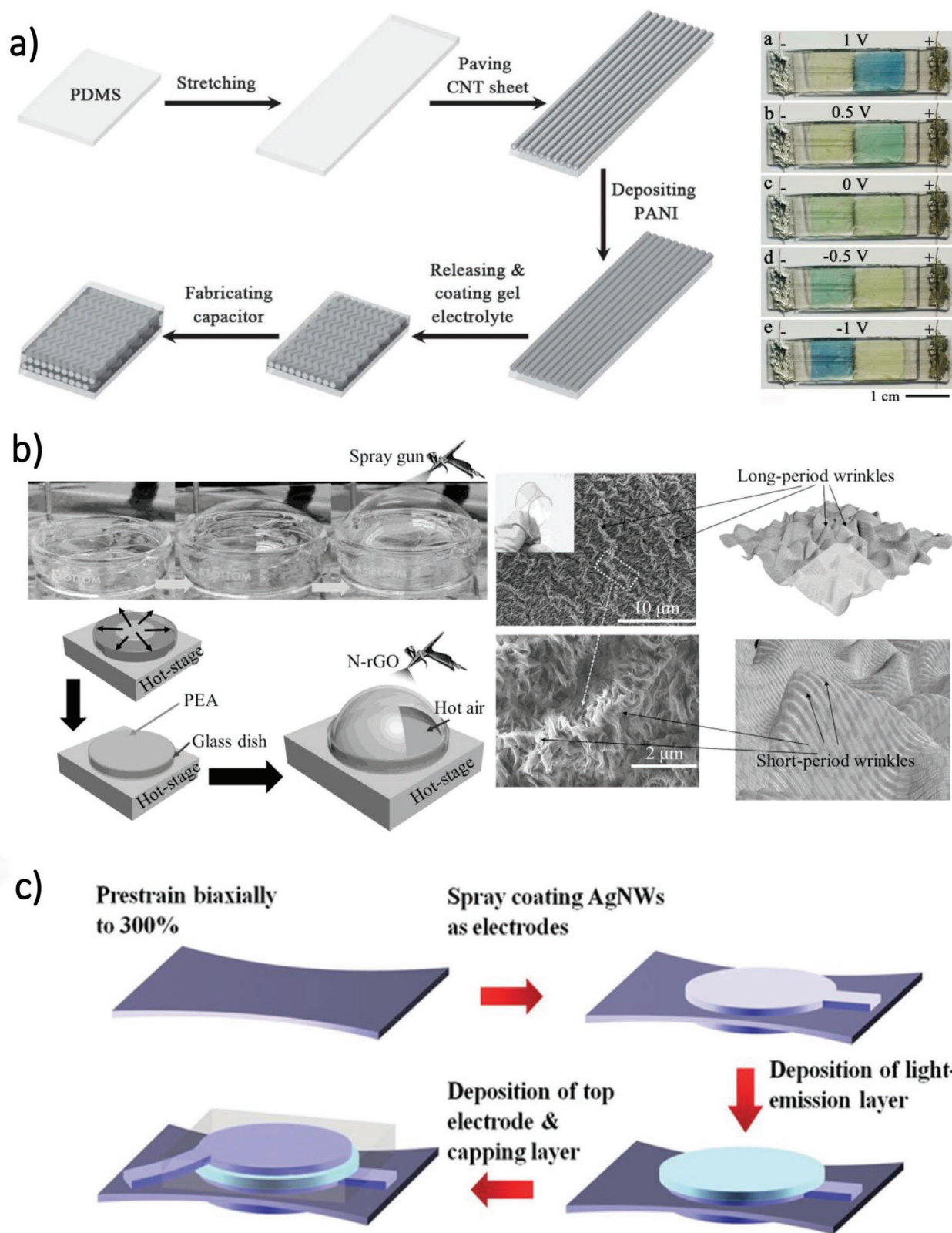


**Figure 7.** a) Schematic illustration of the fabrication process of the stretchable, smart supercapacitor. Reproduced with permission.<sup>[37]</sup> Copyright 2014, John Wiley & Sons. b) Steps for and schematic illustration of transparent conductor preparation. Reproduced with permission.<sup>[38]</sup> Copyright 2016, John Wiley & Sons. c) Schematic interpreting the fabrication procedure of the actively self-deformable electroluminescent device. Reproduced with permission.<sup>[39]</sup> Copyright 2015, John Wiley & Sons.

**Table 2.** Summary of key parameters and features for fiber-shaped DSSC/perovskite/OPV solar cells.

Type	Structure	Design	PCE [%]	Refs.
DSSC	Ti/TiO <sub>2</sub> /N719/I <sup>-</sup> - I <sub>3</sub> /Pt	Twisted	11.22	[47]
DSSC	Ti/TiO <sub>2</sub> /TTZ5/I <sup>-</sup> - I <sub>3</sub> /Pt	Twisted	1.57	[49]
DSSC	Ti/TiO <sub>2</sub> /N719/I <sup>-</sup> - I <sub>3</sub> /core-sheath CF	Twisted	10	[50]
DSSC	P25-rGO/N719/I <sup>-</sup> - I <sub>3</sub> /Pt	Parallel	5.364	[51]
DSSC	Ti/TiO <sub>2</sub> +Ag@SiO <sub>2</sub> NPs/N719/solid-state electrolyte/Pt	Twisted	5.38	[54]
DSSC	Ti/TiO <sub>2</sub> /N719/I <sup>-</sup> - I <sub>3</sub> / CF@PANI@CoSe	Parallel	10.28	[59]
DSSC	Ti/TiO <sub>2</sub> NTA/PVdF-HFP/I <sup>-</sup> - I <sub>3</sub> /Pt	Twisted	6.32	[57]
DSSC	Ti/TiO <sub>2</sub> /N719/Quasi-solid-state electrolyte/MWCNT sheet	Coaxial	2.6	[56]
Perovskite	Ti/TiO <sub>2</sub> /perovskite/spiro-OMeTAD/Au	Twisted	10.79	[61]
Perovskite	Ti/TiO <sub>2</sub> /perovskite/spiro-OMeTAD/Au	Twisted	7.53	[63]
Perovskite	Ag/P3HT/perovskite-PVP nanofiber yarn/SnO <sub>2</sub> -PCBM/CF yarn	Twisted	15.7	[64]
Perovskite	Ti/TiO <sub>2</sub> NTA/perovskite/CNT sheet	Coaxial	7.1	[65]
Perovskite	Ti/TiO <sub>2</sub> /CsPbBr <sub>3</sub> /CNT sheet	Coaxial	5.37	[66]
OPV	Ti/TiO <sub>2</sub> /PEDOT:PSS/P3HT:PCBM/CNT fiber	Twisted	0.15	[73]
OPV	Steel/ZnO/PEDOT:PSS/P3HT:PCBM/graphene	Coaxial	2.53	[74]
OPV	Ti/TiO <sub>2</sub> /P3HT:PCBM/PEDOT:PSS/MWCNT sheet	Twisted	1.23	[45]

and 4.2, we summarize key developments in fiber-shaped energy harvesting devices, e.g., solar cells and nanogenerators, respectively.

#### 4.1. FSSCs

Photovoltaic (PV) devices, also known as solar cells, generate electricity by harvesting photon energy. Their rapid progress in recent decades<sup>[40,41]</sup> has widely attracted attention from the academia and industry to propel the development and implementation of next-generation renewable energy sources. Unlike a traditional solar cell in which the active layer is sandwiched between two electrodes in a planar structure, an FSSC adopts an unconventional approach to form a fiber- or wire-shaped structure, which renders the geometrical advantage to harvest photons regardless of incident angles.<sup>[42]</sup> When evaluating solar cell performances, its power conversion efficiency (PCE), open-circuit voltage ( $V_{oc}$ ), short-circuit current ( $I_{sc}$ ), and fill factor (FF) are critical figures of merits that entail its light-to-current capability, charge separation, charge collection, and charge recombination performance.<sup>[43]</sup> Specifically, PCE is defined as the ratio of output electrical power to the incident light power

( $PCE = \frac{P_{out}}{P_{in}} = \frac{FF \times I_{sc} \times V_{oc}}{P_{in}}$ ) and FF is the quotient of maximum power output divided by  $I_{sc}$  and  $V_{oc}$ . Therefore, obtaining a holistic understanding of how these figures of merits are related to the unique structure of FSSC is imperative. Commonly categorized into either twisted or coaxial form, the 1D configuration of FSSC inevitably induces tension to the entire device. Thus, the choice of materials should consider the durability and bendability while maintaining high light harvesting. To date, the most widely studied options for FSSC are organic solar cells (OPVs)<sup>[44–46]</sup> dye-sensitized solar cells (DSSCs),<sup>[47,48,49–55,56–59]</sup> and perovskite solar cells (PSCs)<sup>[60–62,63–66]</sup> (Table 2). The past decades have witnessed a great deal of interest in the fiber-based PVs based on the latter two material categories. As plotted in Figure 8, DSSC and perovskite FSSCs correspondingly reached remarkable PCEs of 10.28%<sup>[59]</sup> and 15.7%,<sup>[64]</sup> respectively, and decent levels of  $J_{sc}$ ,  $V_{oc}$ , and FF, as shown in Figure 8b–d. Apart from photoactive layer, judicious design and selection of contacts, charge transporting layers are required to maintain charge transport and collection. Thus, the recent progress of FSSC was summarized in this section from the perspective of OPV, DSSC and perovskite to shed light on the material selection and device fabrication. Moreover, the photo-physics and mechanical properties were considered to provide constructive insights to further improve FSSC performance for a wider range of applications.

##### 4.1.1. Fiber-Shaped Dye-Sensitized Solar Cell (FSDSSCs)

DSSCs based on glass electrode were first invented in the 1980s.<sup>[67]</sup> They are known for their facile manufacturing process, low cost, and versatile integration. DSSC PV performance shows noticeably less sensitivity to light intensity than traditional p–n junction solar performance.<sup>[68]</sup> This unique characteristic, along with its reasonable stability makes DSSC a competitive candidate for indoor light harvesting.<sup>[69]</sup> A DSSC comprises a photoanode, a semiconductor layer, an organic or inorganic dye, an electrolyte, and a counter-electrode to complete the entire light-to-current conversion process. Depending on the specific structure design, the incident photons may penetrate through the electrolyte from the counter-electrode side or directly impinge upon the photoanode. In the case of organic dye, the photons are ultimately absorbed and excite the electrons from the highest occupied molecular orbital level to the lowest unoccupied molecular level. The electrons are subsequently injected into the adjacent semiconductor layer, where the electrons are transported to the conduction band. Then, the electrons go through the external circuit and they are eventually collected at the counter-electrode where they are used to regenerate the dye through the reduction of triiodide to iodide. Given the unique structure and mechanism of the DSSCs for light-harvesting, separation, and charge transport, efforts have been made to strengthen the charge transfer efficiency and suppress the charge recombination.<sup>[70]</sup> The energy difference between the semiconductor's Fermi level and redox potential determines the device  $V_{oc}$ <sup>[68]</sup> and serves as the primary energetic step for dye regeneration. The most commonly adopted semiconductor is titanium dioxide (TiO<sub>2</sub>), which

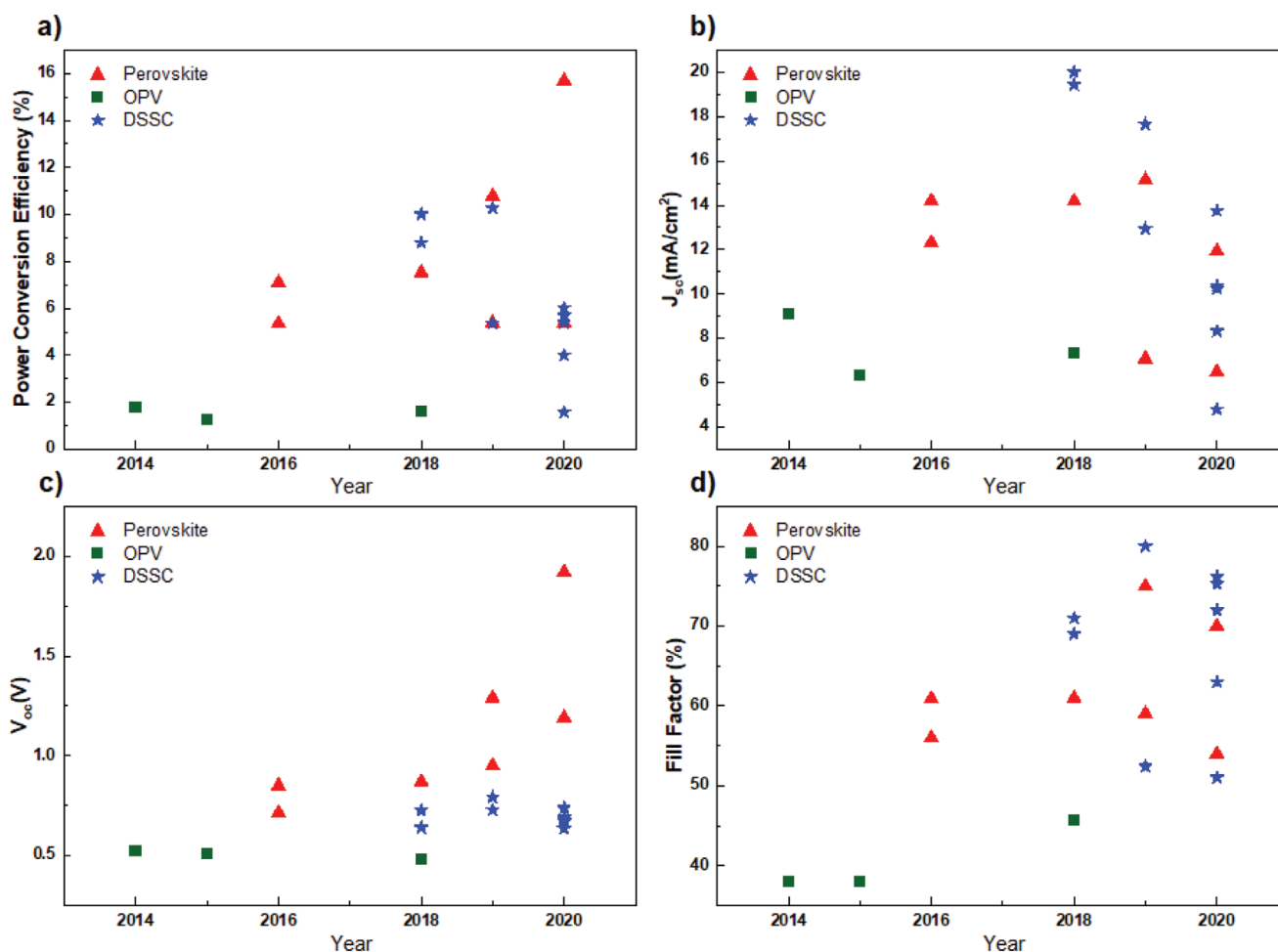


Figure 8. Recent yearly progress of a) PCE, b)  $J_{sc}$ , c)  $V_{oc}$ , and d) FF for OPV, DSSC, and perovskite FSSCs.

has been presented in the form of nanoparticles, nanowires, and nanofibers.<sup>[71]</sup> The recently emerging mesoporous TiO<sub>2</sub> structure creates an elevated capability for dye loading and thus enhances the charge injection (Figure 9a). In addition, the core–sheath-like porous network could achieve in situ growth with Ti wire beneath it (Figure 9b), which increases its mechanical strength toward deformation to suppress charge recombination.<sup>[72]</sup> However, the thickness of the semiconductor layer should be addressed properly so as not to inhibit the charge collection and compromise its conductivity.

Other semiconductors such as ZnO<sup>[75]</sup> have also been used in DSSCs. Despite their decent electron mobility, the susceptibility to electrochemical reactions and unsustainability to acid and base limit their use as an alternative photoanode material for TiO<sub>2</sub>. Other surface engineering techniques have also been explored to modify the Fermi level for improved photoanode performance. Kim et al.<sup>[54]</sup> demonstrated the strong localized surface plasmon resonance effect of Ag-coated SiO<sub>2</sub> nanoparticles on mesoporous TiO<sub>2</sub> network, resulting in PCE of 5.38% and a strong increase in the  $J_{sc}$ . Apart from charge injection, charge recombination is of great concern for efficient charge carrier collection. Techniques such as electrochemical impedance spectroscopy and transient photovoltage/photocurrent measurements have been widely

implemented for quantitative analysis of the charge recombination.<sup>[51,53,54,57,76]</sup> The charge recombination mainly occurs at injection interfaces, electrolyte/dye/semiconductor interfaces, and/or contaminant-induced traps inside the system.

Xiao and Lin<sup>[57]</sup> employed a quasi-solid-state poly(vinylidene fluoride) (PVdF)–Hexafluoropropylene (HFP) gelator electrolyte in a spiral FSSC structure and obtained a PCE of 6.32% (Figure 9c). By optimizing the gel electrolyte concentration, the device managed to achieve a well-constructed pore structure to reduce the charge transfer resistance and suppress charge recombination. Moreover, the iodine concentration was found to play a key role in the charge recombination, in which the mobile electrons may interact with oxidized triiodide at the electrolyte/photoanode interfaces. The authors also pointed out the transmittance relationship with iodine concentration for effective light absorption. Recently, solid-state or quasi-solid-state electrolytes are emerging to find a balance between high conductivity and low viscosity while suppressing volatility and corrosion as well as improving mechanical stability for enhanced flexibility (Figure 9d).<sup>[76,78]</sup> A recent work employed quantum dots (QDs) with N719 dye to boost the PCE to 7.39% through novel core–sheath design and the incorporation of carbon-based electrodes.<sup>[58]</sup> However,

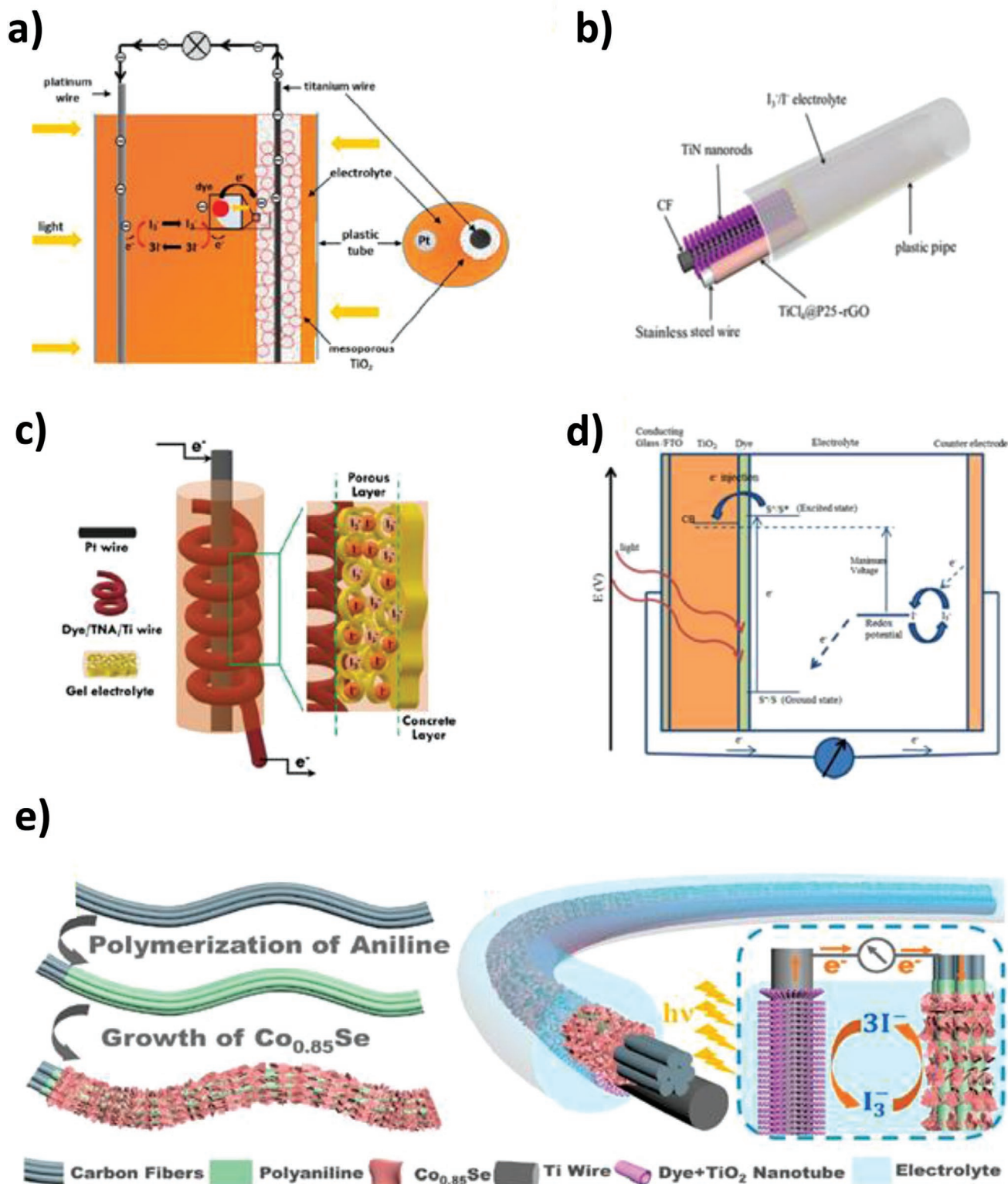


**Figure 9.** Device structure for a) long-thin FSDSSC with Ti and Pt electrodes. Reproduced with permission.<sup>[49]</sup> Copyright 2021, Elsevier. b) Titanium nitride (TiN)-CF FSDSSC. Reproduced with permission.<sup>[52]</sup> Copyright 2021, American Institute of Physics. c) FSDSSC with spirally wrapped photoanode. Reproduced with permission.<sup>[57]</sup> Copyright 2020, Elsevier. d) FSDSSC with ITO as photoanode. Reproduced under the terms of the CC BY license.<sup>[77]</sup> Copyright 2018, Springer Nature. e) FSDSSC with electrocatalytic components. Reproduced with permission.<sup>[59]</sup> Copyright 2019, American Chemical Society.

the charge-transfer intermediate layer formed in solid-state FSDSSC may present optical loss in lower wavelength region,<sup>[54]</sup> indicating the necessity for a thinner and low-loss material for enhanced photon harvesting. Besides electrolytes, photoanode and counter-electrodes are critical for charge collection and effective catalytic reactions. For further enhancement, CNT fibers (CNTFs)/sheet/yarn have been introduced as substitutes for Ti- and Pt-counterparts. These new alternatives offer nontoxicity, lightweight, superior conductivity, a higher tensile strength, and large specific surface area favorable for dye loading (than Ti), and catalytic components incorporation.<sup>[48,56]</sup> By sequentially growing PANI layers and Co<sub>0.85</sub>Se nanosheets on the surface of carbon fibers (CFs) as the counter-electrodes, Zhang et al. successfully pushed the PCE of FSDSSC to a remarkable 10.28% (Figure 9e),<sup>[59]</sup> which is the highest up to date, and it provides key insights for designing next-generation high-performance FSDSSCs.

#### 4.1.2. Fiber-Shaped Organic Solar Cells (FSOPVs)

The past decade has witnessed the unprecedented growth and breakthrough of OPV technology.<sup>[41]</sup> With high performance and specific advantages of low-cost, printability, lightweight, and nontoxicity, these devices have successfully attracted industry for potential commercialization. Unlike DSSC, a typical OPV is made of a photoactive organic semiconductor layer sandwiched between two electrodes. The active layer consists of donor and acceptor components, which can either be in a

planar structure or an interpenetrating bulk configuration to form a heterojunction.<sup>[79]</sup> When light irradiates the photoactive layer, it generates excitons that are tightly bonded by Coulombic force. Those excitons then diffuse to the donor/acceptor interface to complete the charge dissociation process, which is subsequently followed by the charge transport and charge collection to produce electricity. Due to the intrinsic low dielectric constant of organic materials, the amount of energy required for charge separation is much higher than that of inorganic counterparts. Therefore, relatively lower charge mobility and a higher charge recombination is expected. For FSSC, reported OPVs usually present in the form of polymer or polymer:fullerene, for example, poly(3-hexylthiophene) (P3HT) or poly(3-hexylthiophene):[6,6]-phenyl-C61-butyric acid methyl ester (P3HT:PCBM). An ordered structure can be obtained through facile optimization of morphology, which could promote the stability and lifetime of the photoactive layer<sup>[80]</sup> for fiber application. However, few attempts that justified its limited PCE of 3.87%, the highest value for FSSCs to date, have been made on the photoactive layer (Figure 10a).<sup>[81]</sup> Given the copious amount of recently developed high-performance polymer and small molecules, along with numerous promising small bandgap derivatives and nonfullerene acceptor alternatives, a much more versatile approach could be implemented to boost efficiency.<sup>[82]</sup> Meanwhile, much progress has been made on electrode engineering to improve charge transport and light absorption. Multiple carbon-based materials such as CNT, CNT fiber, and graphene were exploited as light-weight conductive alternatives for contacts.<sup>[44,73,74,81]</sup>

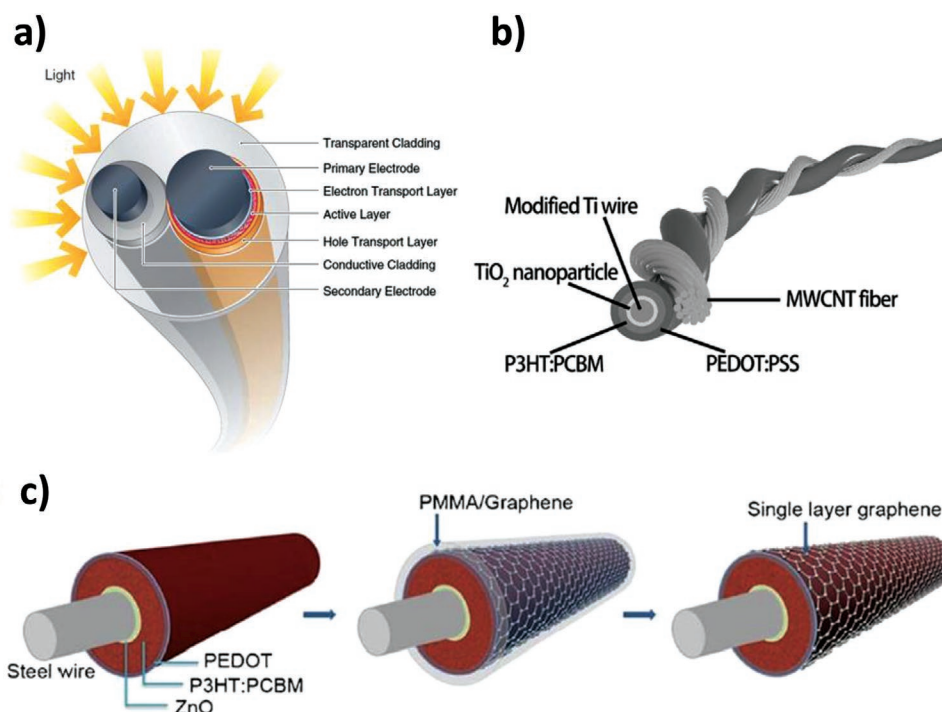


**Figure 10.** Device configuration of a) double-twisted FSOSC primary–secondary electrode with cladding. Reproduced with permission.<sup>[81]</sup> Copyright 2009, The American Association for the Advancement of Science. b) Double-twisted FSOSC with MWCNT fiber electrode. Reproduced with permission.<sup>[46]</sup> Copyright 2014, John Wiley & Sons. c) Coaxial FSOSC with single-layer graphene. Reproduced with permission.<sup>[74]</sup> Copyright 2012, The Royal Society of Chemistry.

The specific manner of twisting configuration noticeably plays a vital role in its performance. As shown in Figure 10a, Lee et al.<sup>[81]</sup> adopted a primary and secondary electrode double-twisting approach to form an encapsulated FSOPV. Even though fiber-shape was supposed to be designed for 3D light harvesting, the photoactive primary could be completely shadowed at certain angles, thus prohibiting effective light absorption. By incorporating a larger cladding with a high refractive index, the authors managed to improve the absorption by 18%. A similar twisting technique reported by Zhang et al.<sup>[46]</sup> deployed MWCNT fiber as the electrode (Figure 10b). The results pointed out that a short pitch distance could potentially give rise to enlarged shading effect, which also increased the distance for charge carrier transport and the tensile force of the device. However, a longer pitch distance could be unfavorable for forming stable and sufficient contacts for charge collection.

The diameter of MWCNT fiber also plays a vital role. While a thicker MWCNT wire could induce shading, a thinner fiber produces larger electric resistance, which compromises the  $J_{sc}$  level. Unlike double-twisted configuration, single-wire structure preserves the uniform coverage of the contact layer through dip-coating or chemical vapor deposition. Liu et al.<sup>[74]</sup> presented a coaxial structure with single-layer graphene as the transparent electrode. By optimizing the electrode thickness and doping with Au, the advantage from high conductivity and superior optical transmittance rendered a stable FSOPV with a PCE of 2.53% (Figure 10c). Apart from achieving a highly conductive and flexible contact, the interfaces with adjacent layers were meticulously addressed to ensure the uniform deposition to avoid shunts and short-circuit issues. Tuning the work function of anode and cathodes was also essential for optimum charge transfer and collection. In light of the high performance and versatility of carbon-based materials for fiber integration, realizing a novel all carbon-based FSOPV is plausible. However, problems such as strain-induced cracks, chain alignments, orientation, and reduced degree of crystallinity remain challenging<sup>[83]</sup> but they are all detrimental for maintaining high efficiency.

#### 4.1.3. Fiber-Shaped Perovskite Solar Cells (FSPSCs)

Solar cells based on perovskite material have attracted tremendous interest in recent years,<sup>[84]</sup> achieving a PCE that is comparable with silicon.<sup>[85]</sup> A commonly adopted composition for perovskite is  $ABX_3$  configuration, where A is a monovalent cation such as methylammonium ( $CH_3NH_3^-$ , MA-), formamidinium ( $CH(NH_2)_2^-$ , FA-), and cesium (Cs); B is a divalent metal such as Pb and Sn and X is a halide anion. Benefiting from their unique structure, perovskites demonstrate high charge carrier mobility, long diffusion length, superior lifetime, and small exciton binding energy.<sup>[86]</sup> Moreover, the tunability achieved by engineering the halide ratio and emerging substitutes for Pb creates prospects for promising applications. In an effort to develop lead free FSPSCs, Balilonda et al.<sup>[87]</sup> recently developed perovskite solar yarns using methylammonium tin halide-polyvinylpyrrolidone (PVP) composite nanofibers doped with PC61BM as the light harvester. A knitted solar fabric of active area  $\approx 4.5 \text{ cm} \times 3.5 \text{ cm}$  developed using the above solar yarn

showed a maximum power density of  $1.21 \text{ mW cm}^{-2}$  under standard testing conditions. For FSPSCs, the past few years also witnessed the incorporation of perovskite into high-performance fiber PV devices. Nanostructured perovskites are also believed to obtain enhanced optical and electronic properties due to the quantum confinement effect, which is absent in the bulk form.<sup>[60,88]</sup> Apart from optimizing the contacts and incorporation of carbon-based material for improved conductivity and flexibility, recent research stressed on the effective method to preserve the quality of the perovskite layer. As shown in Figure 11a, Deng et al.<sup>[89]</sup> presented a unique structure composed of a spring-like Ti wire and a CNT-based fiber, with an average PCE of 5.01%. The introduced addition of 1,8-diiodooctane (DIO) to the process, contributed to the enhanced crystallinity and film coverage.

In addition, unconventional spring-shaped electrodes could help alleviate the stress induced by stretching and bending, thereby justifying their stable performance after numerous testing cycles. Hu et al.<sup>[63]</sup> successfully improved the morphology of the perovskite absorber layer by using lead acetate,  $Pb(CH_3COO)_2$  to realize a PCE of 7.53%. The solvent annealing enabled much larger grains and less grain boundary density, which are conducive traits for reducing traps and charge recombination sites, than thermal annealing (Figure 11b). Annealing time is also reported to be crucial in improving film morphology. A long time does not necessarily guarantee improved crystallinity, it could also instigate low surface coverage. While material synthesis and processing are crucial, fabricating techniques are also of paramount importance. The widely adopted dip-coating methods are proven to potentially cause low crystallinity and prohibit efficient charge transport, which eventually compromises the output current. Dong et al.<sup>[61]</sup> instead implemented vapor-assisted deposition, which is favorable for  $PbI_2$  coating and subsequent solid-gas reaction with methyl ammonium iodide (Figure 11c). Followed by direct thermal annealing to remove the residue without additional solvent, the device reached a remarkable PCE of 10.79%. Li et al.<sup>[64]</sup> formed an unconventional electrospun nanofiber web composed of perovskite and PVP (Figure 11d). The novel hybrid active layer structure exploited the flexible support from the polymer to ensure the uniform and compact growth of perovskite, which prompted the purer and larger domain size at later stages. The interconnected fibrous web favored the multireflection inside the layer to further promote light harvesting. With the encapsulation of polymethyl methacrylate (PMMA), the authors managed to realize a champion PCE of 15.7% and demonstrate the capability of the web to be woven into weft and warps for further textile electronics applications. The success of the incorporation of organic hole transport layer and hybrid electron transport layer noticeably paved the way for low-temperature processing options to reduce the manufacturing cost. As far as FSPSC is concerned, efficient deposition of the active layer on a fibrous surface while maintaining excellent morphology remains an ongoing challenge. Judicious processing techniques and material combinations are required to form the desired perovskite composition. With proper encapsulation and novel contacts, FSPSCs could herald the future of next-generation high-performance fiber-shaped electronics. Furthermore,

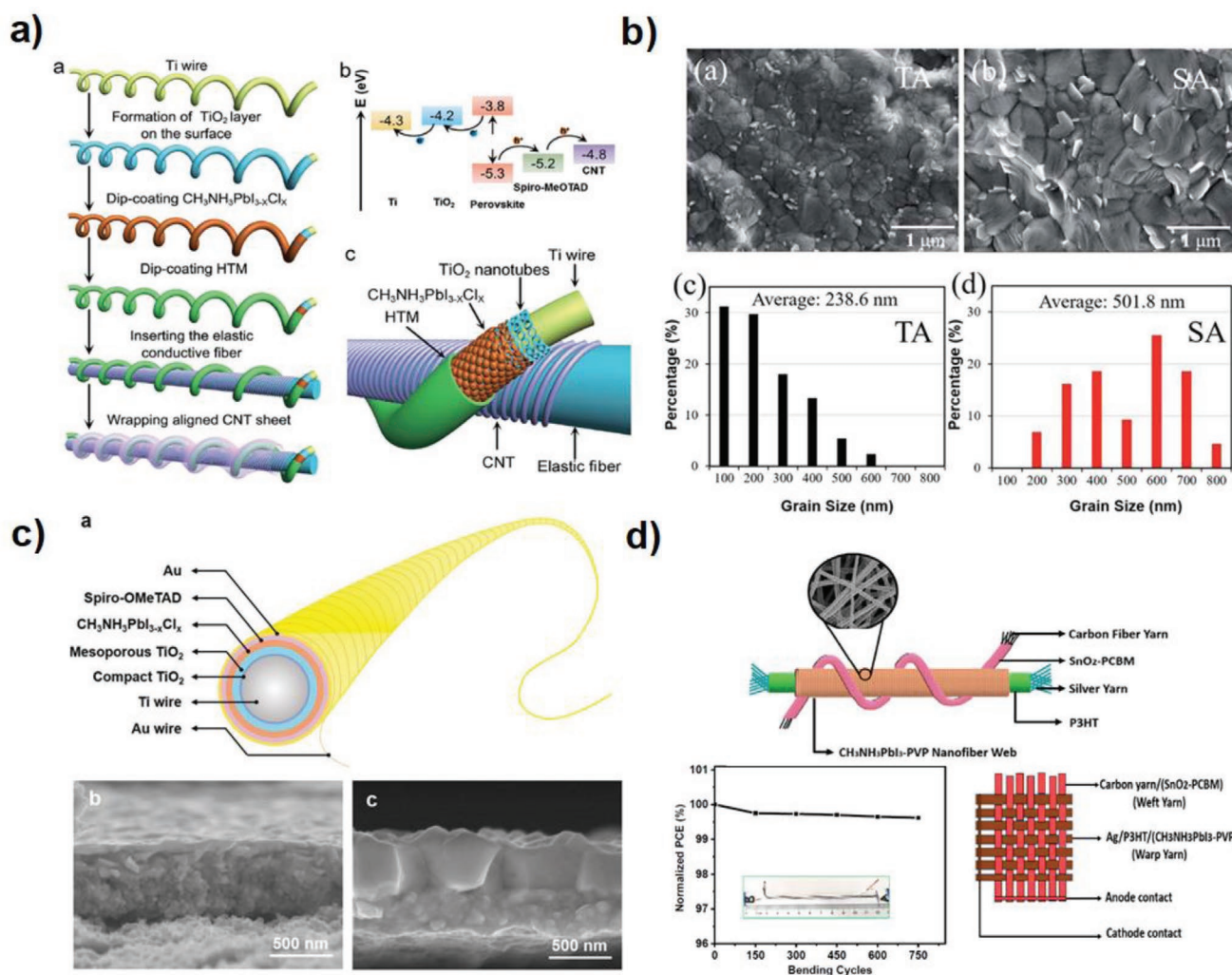


**Figure 11.** a) Spiral-like Ti wire-based FSPSC structure, energy diagram, and configuration. Reproduced with permission.<sup>[89]</sup> Copyright 2015, The Royal Society of Chemistry. b) Grain size comparisons after thermal annealing (TA) and solvent annealing (SA). Reproduced with permission.<sup>[63]</sup> Copyright 2018, The Royal Society of Chemistry. c) Device structure and vapor-assisted deposition SEM cross-section image. Reproduced with permission.<sup>[61]</sup> Copyright 2019, John Wiley & Sons. d) Device structure of flexible solar yarn based on electrospun perovskite composite nanofibers along with the bending cycles and weaving application schematics. Reproduced with permission.<sup>[64]</sup> Copyright 2020, John Wiley & Sons.

Balilonda et al.<sup>[60]</sup> pointed out the importance of passivation of traps at individual junctions to mitigate charge accumulation for reduced recombination, as well as the necessity of thermal induced degradation analysis on perovskite layer for long-term stable FSPSCs.

In conclusion, we have critically reviewed recent advances for FSDSSCs, FSOPVs, and FSPSCs. In light of their uprising performances, FSSCs have demonstrated their presence in novel wearable applications.<sup>[6,90]</sup> As pointed out by several review articles,<sup>[6,91]</sup> geometric feasibility as well as key figure of merits should be equally emphasized to achieve further commercial applications. In addition, even though scalability is vital for general solar cells fabrication, the suitability of device structure, choice of materials, along with flexibility and degradation should also be considered for optimum design. In this way can we maximize the advantage of fiber-shape properties

and approach with user-oriented perspective to bridge the gap between lab and industry.

## 4.2. Fiber-Shaped NGs

As the fiber-shaped optoelectronic and sensor's technology makes great strides and the demand for flexibility, mobility, and stretchability of these multitudes of light emitting and sensing devices is rapidly increased, the necessity of energy sources and self-powered systems is of great importance. Over the last 20 years, research has turned to eco-friendly, "green," and renewable energy sources, such as solar,<sup>[92]</sup> magnetic,<sup>[93]</sup> thermal,<sup>[94]</sup> and chemical<sup>[95]</sup> energies, to supply enormous energy consumption in the modern society on the basis of portable and wearable electronic devices, while prohibiting the pollution-proneness

**Table 3.** Summary of fiber-shaped PENGs and F-TENGs.

Structure of F-PENG	Electrode	Active materials	Power outputs	Refs
Spiral twining	Au	ZnO NWs	5 pA, 1 mV, 20 mW m <sup>-2</sup>	[98]
Coaxial	Carbon fiber (inner), Ag (outer)	ZnO	3.2 V, 0.15 μW cm <sup>-2</sup>	[7]
Core–sheath	CF (inner), Au (outer)	ZnO	0.09 μA cm <sup>-2</sup> , 17 mV	[99]
Coaxial	Cr-coated Kevlar	ZnO NWs	4.8 pA, 1.8 mV	[100]
Coaxial	Carbon (inner), indium (outer)	PVDF–TrFE	1 V	[101]
Coaxial	Ag-coated nylon (inner), CNT sheet (outer)	PVDF–TrFE	2.6 V	[102]
Twisted	Aluminum foils	PVDF–TrFE	20 mV	[103]
Core–shell	Au/Cr/PI film	PTO NT array	1.0 nA cm <sup>-2</sup> , 623 mV	[104]
Woven	Ag-coated PI/stainless steel	PVDF (melt-spun)	3.5 V, 130 nW	[105]
Coaxial	Ag-coated nylon yarn	PVDF (NFs and film)	18.76 nA, 0.52 V	[106]
Triaxial-braided	Ag-plated PA yarns	PVDF (fiber)	380 mV, 29.62 μW cm <sup>-3</sup>	[107]

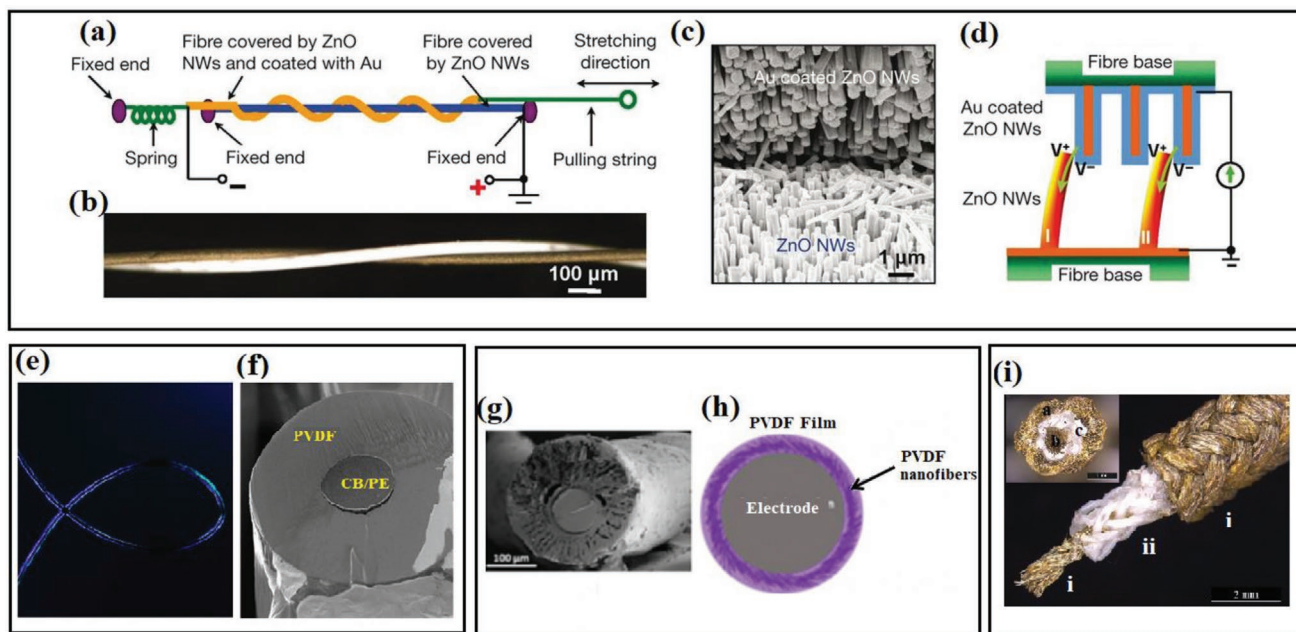
  

F-TENG				
Structure of F-TENG	Device's components		Power outputs	Refs.
Coaxial	Stainless steel/PET-blended fibers wrapped by silicone rubber		0.3 μA, 18 V	[108]
Coaxial	Cu-coated PET fiber covered by PDMS		–	[109]
Coaxial	CNTs as the core fiber and silk fibroin as the sheath layer		18 mW m <sup>-2</sup>	[110]
Coaxial	Carbon fiber bundles covered with silicone rubber		0.5 μA, 42 V	[112]
Woven	Silicone rubber and Au-coated Cu threads		34.4 μW cm <sup>-2</sup>	[113]
Helical	Silicone rubber tubes and stainless steel yarns		12.5 μW m <sup>-1</sup>	[114]
Spiral	Spiral steel wire covered by silicone rubber		2.67 μA, 59.7 V, 2.13 μW	[115]
Coaxial	Nylon fiber wrapped Cu fiber and PTFE fiber wrapped Cu fiber	1.42 mA m <sup>-2</sup> , 2.15 V (vertical separating mode)		[116]
Coaxial	PDMS core coated with a carbon electrode and an outer silicon rubber tube		1.15 μA, 32.2 V	[117]
Coaxial	Liquid metal Galinstan injected in silicone rubber		15.6 μA, 8.43 mW m <sup>-2</sup> (area of 6 × 3 cm <sup>2</sup> )	[118]
Coaxial	Organogel injected in silicone hollow fiber		550 μA m <sup>-2</sup> , 40 V	[119]
Core–shell	CNT films wrapped on silicone rubber fiber, further covered by silicone rubber film Cu wires		0.18 μA m <sup>-1</sup> , 140 V	[120]
Coaxial	Ag NW and PTFE coatings on a bare PU fiber, and a sheath electrode PDMS–Ag NW		2.25 nW cm <sup>-2</sup>	[121]
Core–shell	Ag-coated nylon fibers wound on PU fiber and PVDF–TrFE mats covered by CNT sheets		8 nA, 24 mV	[122]
Core–shell	Ni-coated polyester conductive textile wrapped around a silicone tube		11 μA, 380 V, 1.638 mW	[123]
Core–shell	CNT/PANI covered on silicone rubber fiber and varnished wire containing insulation varnish		12.5 nA, 0.2 V	[124]
Core–shell	Ag-coated nylon fibers spirally twined around silicone rubber fiber		0.43 μA, 19 V	[125]
Core–shell	Cu/Ag PET fibers spirally twisted PU fibers		5.8 μA, 84 V	[126]

of convention fossil fuels. However, their high dependence on external factors such as environmental conditions and their rigidity and heavy-weight, make them unsuitable for large-scale and wearable applications. NGs are an emerging energy-harvesting technology, suitable for lightweight, flexible, and environmental friendly wearable electronics, based on the conversion of mechanical energy to electrical energy.<sup>[96]</sup> In terms of the working principle, the materials and the device structure, NGs could be categorized into pyroelectric NGs,<sup>[97]</sup> piezoelectric NGs (PENGs),<sup>[98]</sup> and triboelectric NGs (TENGs) (see **Table 3**).<sup>[99]</sup> Pyroelectric NGs utilize the pyroelectric effect to convert the thermal energy into electricity, while PENGs could effectively convert the applied mechanical strain inside the material into electrical energy. TENGs conjoint the contact electrification

process with the electrostatic induction for the successful power conversion of mechanical energy into electricity. Among their many advantages, the ability of NGs to harvest energy that is daily wasted has boosted research interest and their broad application in wearable electronics and self-powered systems.

NGs have been successfully developed and incorporated in wearable electronics to harvest and convert body motion energy into electricity. In particular, the integration of NGs into conventional textiles contributed to the full usage of their properties attributed to the comfortability of the textile and the high integration with the human body. However, the stretchability is one of the main drawbacks of textile-NGs. Fiber-shaped NGs have been extensively studied due to the fibers advantage such as small-dimension, lightweight, flexible, bendable, permeable,



**Figure 12.** Fiber-shaped piezoelectric nanogenerators. a) Schematic experimental setup of the fiber-based nanogenerator. b) An optical micrograph of a pair of entangled fibers, one of which is coated with Au (in darker contrast). c) SEM image at the “teeth-to-teeth” interface of two fibers covered by nanowires (NWs), with the top one coated with Au. The Au-coated nanowires at the top serve as the conductive “tips” that deflect/bend the nanowires at the bottom. d) The piezoelectric potential created across nanowires I and II under the pulling of the top fiber by an external force. Reproduced with permission.<sup>[101]</sup> Copyright 2008, Springer Nature. e) Cross-polarized optical micrograph (scale bar of 200  $\mu\text{m}$ ) and f) SEM image (scale bar of 20  $\mu\text{m}$ ) of the cross-section of a flexible piezoelectric yarn consisting of a layer of electrospun PVDF nanofibers integrated with PVDF film. Reproduced under the terms of the CC-BY Creative Commons Attribution 4.0 International License.<sup>[108]</sup> Copyright 2018, Nature Publishing Group. g) Cross-section SEM image and h) schematic illustration of a melt-spun piezoelectric microfiber consisting of a conducting carbon black/polyethylene core surrounded by  $\beta$ -phase PVDF polymer. Reproduced with permission.<sup>[109]</sup> Copyright 2018, IOP Publishing. i-b) Optical photograph of the as-developed triaxial braided piezoelectric generator; i) silver coated nylon as inner and outer electrodes and ii) braided PVDF fibers as the intermediate layer. Photograph of the cross-section of the fabricated energy harvesting generator based on triaxial braided PVDF fibers; a,b) silver coated nylon as outer and inner electrodes, respectively, and c) braided piezoelectric PVDF fiber, presented as inset of panel (i). Reproduced with permission.<sup>[110]</sup> Copyright 2019, The Royal Society of Chemistry.

and washable properties.<sup>[100]</sup> The first reported fiber-based PENG (F-PENG)<sup>[101]</sup> was fabricated using ZnO NWs radially grown on Kevlar fibers which were then coated with Au to serve as electrode. The proposed F-PENG, as illustrated in **Figure 12a–d**, was based on the entangling of two fibers, one as-grown and one coated with Au, and on the relative brushing of the two fibers to power generation due to piezoelectric effect combined with a semiconductor process. However, this approach is unsuitable for long-term wearable use. Various F-PENGs using inorganic<sup>[7,102]</sup> and organic-polymer<sup>[103,104]</sup> piezoelectric materials have been developed afterward for effective harvesting of inexhaustible mechanical energy and the conversion into electricity. PVDF is one of the most widely used polymer in PENGs to enhance mechanical endurance and power generation.<sup>[105–107]</sup> In particular,  $\beta$ -phase PVDF exhibits high piezoelectric activity attributed to the large polarization.

A high-power-output F-PENG was recently demonstrated using melt-spun continuous microfibers with a conducting core consisting of carbon black/polyethylene and a PVDF-sheath, while the outer electrode was spirally winding (Figure 12e,f).<sup>[108]</sup> The fabricated F-PENG effectively harvested body motion energies even in rainy days compared with other energy harvesting textiles that shows shorting under water contact. Moreover, a flexible F-PENG with good power output was reported, where

PVDF electrospun nanofibers wound around the conductive core, were coated with PVDF film (Figure 14g,h).<sup>[109]</sup> The dual role of the nanofibers to serve as piezoelectrical materials and as porous scaffolds for the polymer absorption to form high-quality PVDF films improved the energy conversion ability of the F-PENG. A novel type of energy harvesting devices based on triaxial braided F-PENG with enhanced mechanical and piezoelectric properties and improved stability in the terms of the metallic electrode’s durability was recently demonstrated (Figure 12i).<sup>[110]</sup> This new F-PENG using the triaxial structure, where melt-spun PVDF fibers were braided with Ag-coated nylon yarns, followed by a second braiding with Ag-coated nylon fibers exhibited a maximum output voltage of 380 mV and a power density of 29.62  $\mu\text{W cm}^{-3}$ .

Forouzan et al.<sup>[111]</sup> undertook a comprehensive study on the effect of geometrical parameters, viz. yarn linear density (measured as  $T_{\text{ex}}$ ), twist per meter (TPM), plying, as well as weft and warp density on the piezoelectric voltage of aligned electrospun yarns of PVDF polymer and poly[(vinylidene fluoride)-*co*-trifluoroethylene] [P(VDF-TrFE)] copolymer. Yarns were developed by twisting and plying electrospun nanofibers and their mechanical and piezoelectric properties are systematically investigated. This work shows that piezoresponse of the woven nanogenerators can be enhanced by decreasing  $T_{\text{ex}}$  and

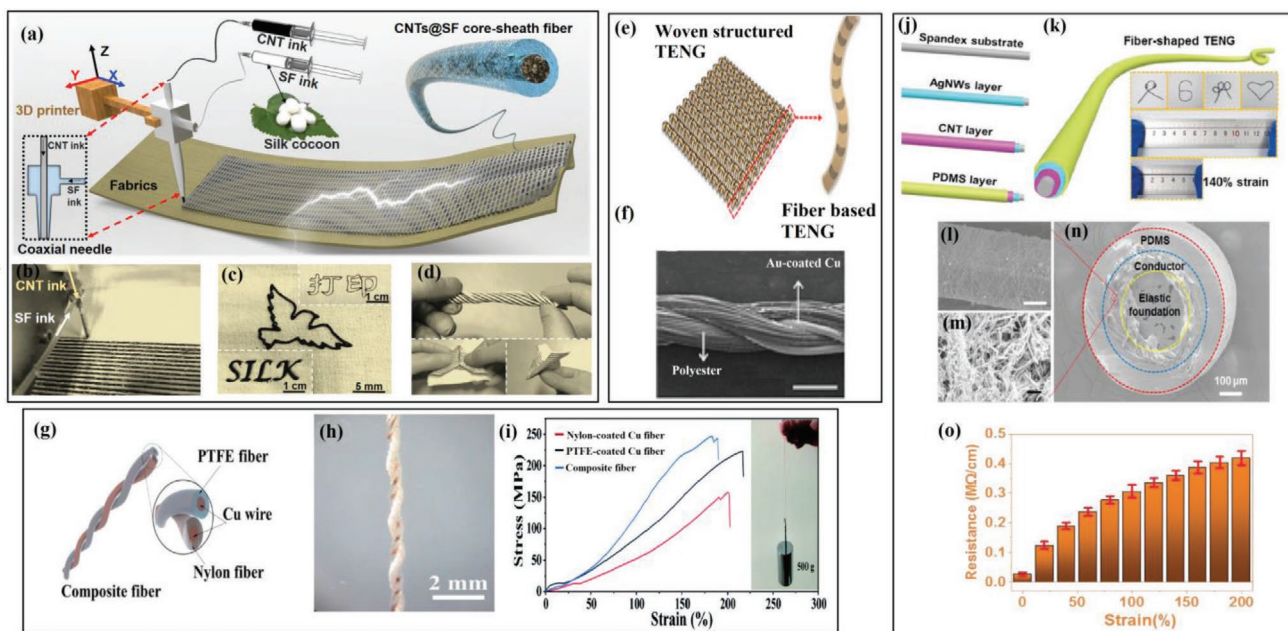


**Figure 13.** Direct printing of core-sheath fiber-based patterns on fabrics for energy-management smart textile. a) Schematic illustration showing the 3D printing process using a coaxial spinneret. b) Photograph of the 3D printing process. c) Photographs of customer-designed patterns on textile, including English letters of SILK, a pattern of a pigeon, and Chinese characters of PRINTING. d) A smart textile under twisting and folding, showing its high flexibility. Reproduced with permission.<sup>[114]</sup> Copyright 2019, Elsevier. e) Schematic illustration of the flexible single-strand fiber-based woven-structured TENG; the figure on the right is the fiber-based TENG. f) Top-view SEM image of the Au-coated Cu thread; scale bar: 300  $\mu\text{m}$ . Reproduced with permission.<sup>[116]</sup> Copyright 2018, American Institute of Physics. g) The structure of the F-TENG with a coaxial double helix structure. h) Digital photograph of the F-TENG. i) Stress-strain curves of the nylon-wrapped Cu fiber, PTFE-wrapped Cu fiber, and the composite FTNG fiber. The inset is a digital photograph of the FTNG hanging a 500 g weight. Reproduced with permission.<sup>[119]</sup> Copyright 2020, The Royal Society of Chemistry. j) The preparation process of the highly flexible and mechanically stable F-TENG with coaxial structure, in which the conductive silver nanowires/carbon nanotubes core was encapsulated by PDMS. k) Schematic diagram and photographs of the flexible and stretchable F-TENG. The F-TENGs can be well maintained after being stretched with a strain up to 140%, and can also be folded into different shapes. SEM images of l) Ag NWs electrode (scale bar: 5  $\mu\text{m}$ ) and m) CNTs electrode (scale bar: 500 nm) coated on the spandex fiber. n) Cross-sectional SEM images of the F-TENGs. o) The electric resistance changes of the F-TENG with the initial length of 100 mm at various strain levels (0–200%). Reproduced with permission.<sup>[127]</sup> Copyright 2020, Wiley-VCH GmbH.

increasing the TPM, the plying number, and the fabric density. A record piezovoltage of  $\approx 2.5$  V is achieved through this work.

In addition, fiber-shaped triboelectric NGs (F-TENGs) have been extensively studied and various F-TENGs have been designed and developed in accordance with the coaxial or core shell structure. Based on the working mode, F-TENGs could be divided into two groups, namely single-electrode (SE) F-TENGs and vertical contact-separation (CS) devices. In the former case, an inner fiber electrode serving as the dielectric material and the protective layer is encapsulated by an outer layer. The CS F-TENGs usually adopt the core-sheath design, where the inner core of the device is separated with the sheath by a gap. According to the simple design of SE F-TENGs, the core fiber electrode is wrapped by dielectric polymers, such as silicone rubber<sup>[112]</sup> and PDMS.<sup>[113]</sup> However, the absence of absolute matching of the outer polymer layer with the human skin and the increase in fiber size due to polymer coating led to the use of commercial fibers winding the core electrode. For instance, high-performance fiber-shaped TENG consisting of CNTs as the core electrode coated with silk fibroin directly printed on fabric were developed.<sup>[114]</sup> Figure 13a–d shows the direct printing of core-sheath fiber-based patterns on fabrics for energy-management smart textile. Despite the simple and

practical use of direct printing and the achieved high-power density of  $18 \text{ mW m}^{-2}$ , the device exhibited poor stretchability attributed to the straight core electrode. One strategy to improve stretchability is the use of stretchable fibers wrapped with fiber electrodes.<sup>[115]</sup> The F-TENG based on this approach with Au-coated Ag electrode woven with silicone rubber fiber (Figure 13e,f) showed good flexibility, a high power generation performance of  $\approx 34.4 \mu\text{W cm}^{-2}$ , and excellent durability.<sup>[116]</sup> Meanwhile, improved stretchability was achieved by a helix design method,<sup>[117,118]</sup> where a spiral steel wire, which served as the electrode, was coated with silicone rubber that acted as the triboelectric layer. The fabricated F-TENGs exhibited high flexibility and improved stability and tailorability. Besides stretchability, the helical design was explored to improve the robustness of F-TENGs, where nylon/Cu and PTFE/Cu fibers were wound in a coaxial double helix structure (Figure 13g–i).<sup>[119]</sup> Furthermore, flexible SE fiber-shaped TENGs have been developed using stretchable components,<sup>[120]</sup> including PDMS, carbon, and silicone rubber. Highly flexible and mechanically stable F-TENGs with coaxial structure, in which the conductive Ag NWs/CNT core was encapsulated by PDMS (Figure 15j–o),<sup>[127]</sup> were recently reported. In another work, poly(3,4-ethylenedioxythiophene)-poly(styrenesulfonate) (PEDOT:PSS) combined

with silicon rubber, which served as liquid electrode and triboelectric layer, respectively, was introduced in liquid electrode-based stretchable and highly efficient F-TENGs with an average power density of  $8.43 \text{ mW m}^{-2}$  at 3 Hz.<sup>[121]</sup> Triboelectric fibers with an organogel/silicone core/shell structure recently presented good stretchability and also limited the cracking issues of the metallic core wires used in most F-TENGs.<sup>[122]</sup> The solid form of the organogel was beneficial to the device, confining the liquid conductor.

Despite the simple and easy fabrication process of single-electrode F-TENGs, these devices suffer from low and unstable power output, thereby limiting their prospect for wide application. Thus, vertical contact-separation F-TENGs were developed on the basis of the core-shell structure. Depending on the device structure, CS fiber-shaped TENGs could be categorized into four different types and many materials with different properties have been used as core and shell layers. For example, in the simplest first type, a F-TENG was prepared using CNTs twined by silicone rubber serving as the core of the device and copper wire as the shell (Figure 14a).<sup>[123]</sup> In the case of the second type, the core is consisted by a dielectric layer twined around the inner electrode, while the shell has the same configuration, such as PTFE-coated PU/Ag NWs and Ag NWs/PDMS (Figure 14b).<sup>[124]</sup> The third type is the reversible construction of the second type. In this type, a F-TENG was fabricated with a core consisting of Ag-coated nylon fiber wrapped on PU fiber and a shell of CNTs coated with PVDF-TrFE (Figure 14c).<sup>[125]</sup> The fourth type is the most commonly used. A F-TENG based on this type (Figure 14d) was developed using a silicone rubber tube/Ni-coated polyester textile-based core and CNT-layer inserted between two silicone rubber layers serving as the shell.<sup>[126]</sup> The corresponding F-TENG with a length of 6 cm exhibited high  $I_{SC}$  of 11  $\mu\text{A}$  and  $V_{OC}$  of 380 V, hence a high power of 1.638 mW. In the same framework, a varnished wire served as one electrode wrapped around another electrode consisting of CNT/PANI-coated silicone rubber (Figure 14e).<sup>[128]</sup> A flexible F-TENG was also fabricated on the basis of the twining process of both inner and outer fibers.<sup>[129]</sup> A yarn network composed of three-ply-twisted nylon/Ag fiber with a zigzag structure incorporated in an elastomer dielectric improved the stretchability and mechanical stability of the F-TENG. The helical structure was also applied in the inner electrode of a core-shell F-TENG (Figure 14f), where a conductive fiber was wined around a urethane fiber that served as the core, exhibiting a maximum open-circuit voltage of 169 V and a short-circuit current of 18.9  $\mu\text{A}$ .<sup>[130]</sup>

In summary, various fiber-shaped NGs have been developed and studied with main differences on working principles and respective mechanisms. A large variety of materials and structures was also summarized. Although fiber-shaped NGs have attracted much interest among the scientific society, in the last decade, and great progress has been achieved in this field, there are still obstacles on the way of their commercialization, such as long-term stability, wearability, stretchability, and low power output. However, their vigorous development solving these issues makes fiber-shaped NGs a promising energy-harvesting technology highly suited for wearable applications.

## 5. Fiber-Shaped Energy Storage Devices

Energy storage is inevitably an important future technology, with its role mounting following a stronger entanglement between human activities and cyber technologies. In this section, we discuss key updates regarding the fiber-shaped energy storage devices, namely, supercapacitor (Section 5.1) and batteries (Section 5.2).

### 5.1. FSCs

The high demand of energy in the 21st century mandatorily necessitates sustainable and high-performance ESDs aside from renewable energy sources. SCs are energy storage devices known for high power density, cyclic stability, and environment safety.<sup>[131]</sup> In particular, FSCs are potential candidates for high-performance wearable electronic devices as traditional planar SCs could not meet the lightweight, compactness, flexibility, portability, etc., requirements. An FSC comprises a cathode, an anode and an electrolyte, exactly as conventional SC. FSCs require flexible current collectors, firm attachment or coating of active material over current collectors, sol-gel or semiaqueous electrolytes, flexible packaging, and most importantly a fiber-like shape. A wearable FSC needs fiber-shaped current collectors that could be able to withstand frequent wear and tear, squeezing, bending, air, and moisture resistance. However, fiber-shaped electrodes lack in electrochemical performance compared with conventional planar electrodes due to their less active surface area. In other words, assembling a wearable FSC with all its required features give rise to decreased electrochemical performance compared with traditional SCs, i.e., lower energy density, inferior power density and cyclic stability. Several innovative steps are being adopted by many research groups to enhance the performance of FSCs. In accordance with the device architecture, FSCs could be categorized into planar (PFSCs), twisted (TFSCs), coaxial (CFSCs), and roll-typed (RFSCs). A schematic of four types of FSCs is shown in Figure 15. These devices could be easily used for wearable electronics via knitting or weaving with textiles or garments. The different types of FSCs are described hereafter with their merits, demerits, device design, and electrochemical performance.

#### 5.1.1. PFSCs

In PFSCs, the two fiber-shaped electrodes, i.e., anode and cathode, are placed parallel in one plane over a flexible substrate and coated with some gel electrolyte. An FSC for wearable application may undergo several mechanical deformations such as bending, twisting, stretching, or squeezing. Thus, 1D SCs are preferable for FSC application as they endow less weight, flexibility and compactness than 2D or 3D bulky SCs. However, the small dimension of electrodes reduces the active surface area and ion storage space thus diminishing the energy density. Therefore, high mass loading is required to achieve the target electrochemical performance, which, however, may hinder ion diffusion and decrease capacitance retention. Constructing

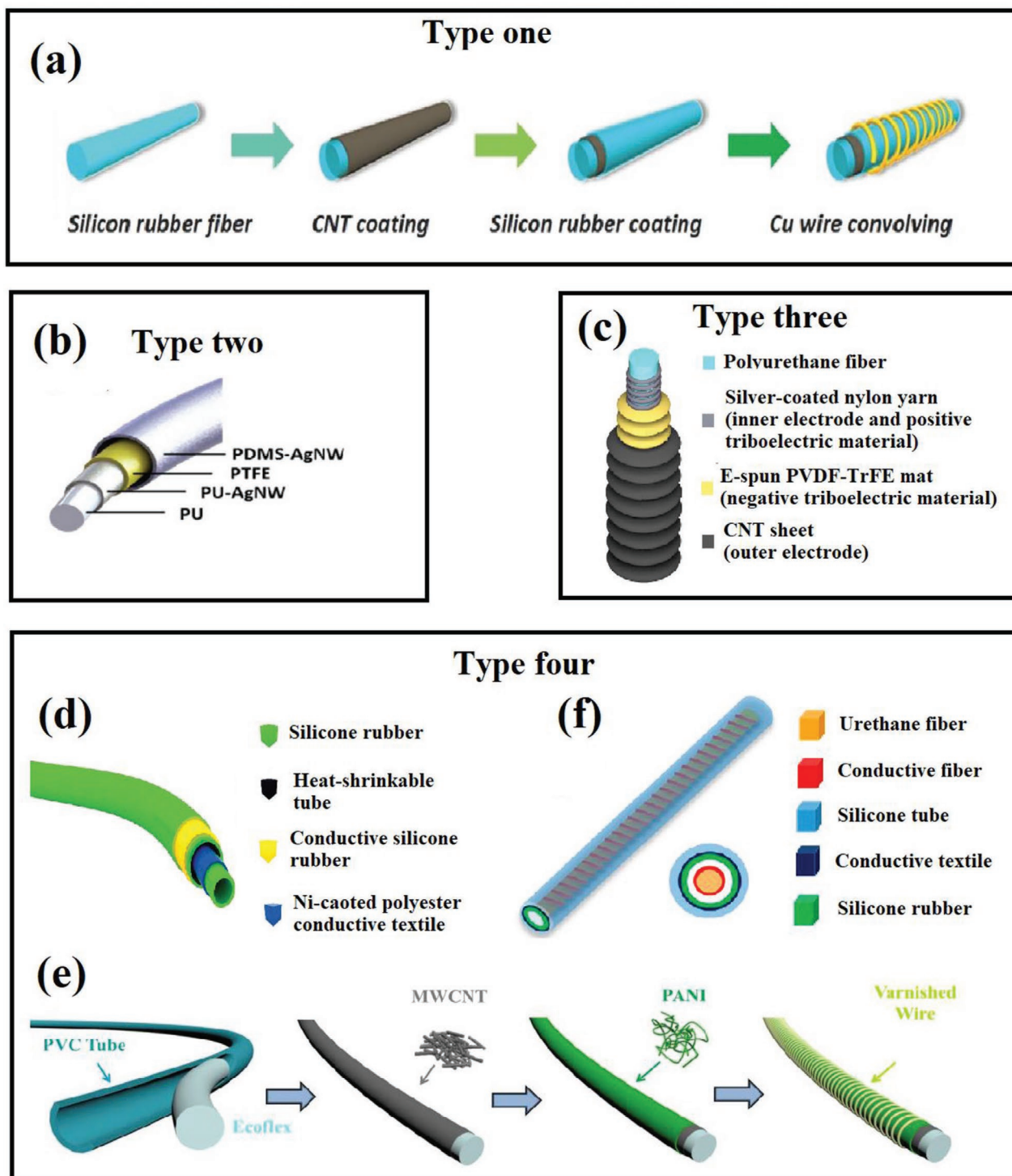


**Figure 14.** Four different types of CS fiber-shaped TENGs depending on the device structure. a) A highly stretchable F-TENG fabricated by wrapping Cu microwire around a stretchable CNT/silicone rubber fiber. Reproduced with permission.<sup>[123]</sup> Copyright 2017, Wiley-VCH. b) A stretchable F-TENG with a core–sheath fiber structure assembled from a core fiber comprising Ag NW and PTFE coatings on a bare PU fiber, and a sheath electrode of PDMS–Ag–NW film. Reproduced with permission.<sup>[124]</sup> Copyright 2017, Elsevier. c) A stretchable triboelectric fiber with multilayered core–shell and wrinkle structures designed with Ag-coated nylon fiber twining around PU fiber as the core and wrinkled PVDF–TrFE/CNT layer as the shell. Reproduced under the terms of the CC-BY Creative Commons Attribution 4.0 International License.<sup>[125]</sup> Copyright 2016, Nature Publishing group. d) A core–shell coaxially structured F-TENG designed with conductive textile wrapped silicone rubber tube as the core and CNT sandwiched between two silicone rubber layers as the shell. Reproduced with permission.<sup>[126]</sup> Copyright 2018, The Royal Society of Chemistry. e) A self-powered wearable sensing fiber presented by coating multiwall CNT and PANI derivatives on silicone rubber fiber, and further twining with varnished wires. Reproduced with permission.<sup>[128]</sup> Copyright 2018, IOP Publishing. f) A core–shell and helical-structured cylindrical TENG with a conductive fiber was winded around a urethane fiber served as the core. Reproduced with permission.<sup>[130]</sup> Copyright 2019, American Chemical Society.

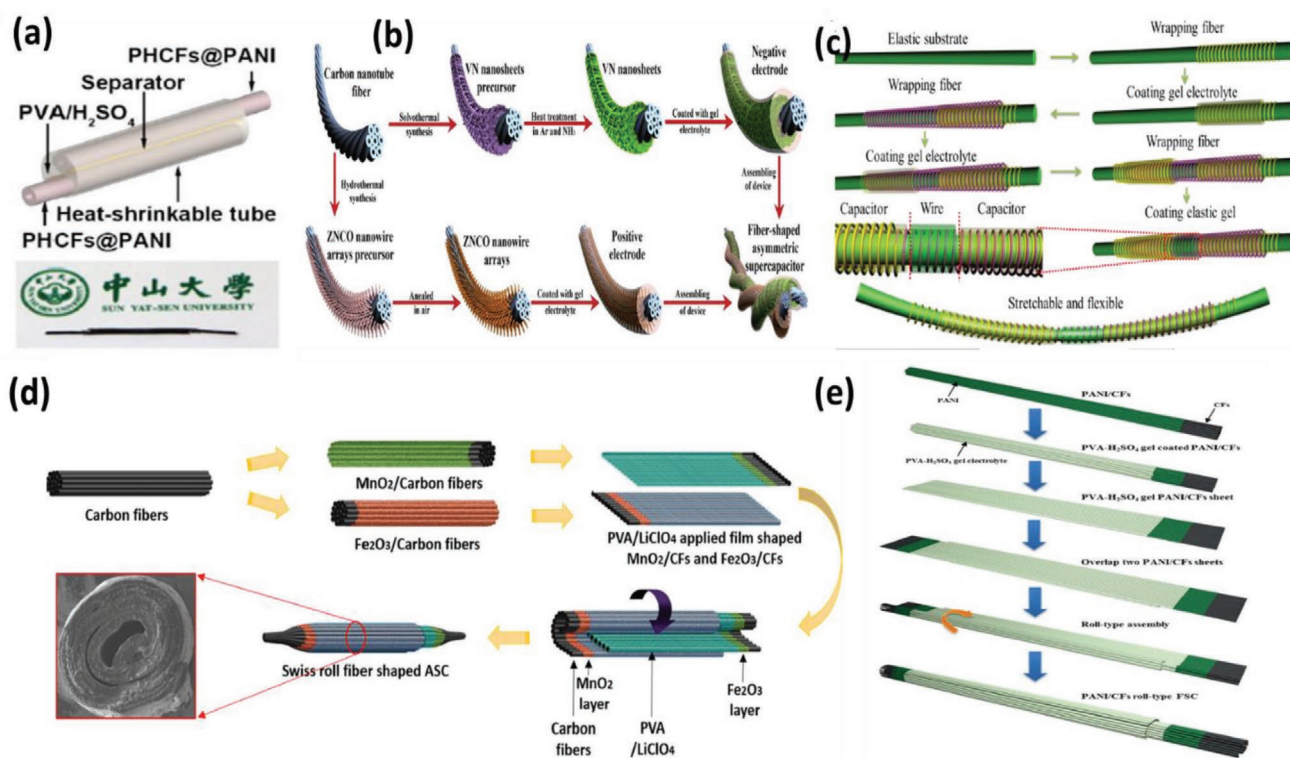


**Figure 15.** Schematic illustration of a) PFSC, Reproduced with permission.<sup>[132]</sup> Copyright 2018, The Royal Society of Chemistry, b) TFSC, Reproduced with permission.<sup>[133]</sup> Copyright 2018, Elsevier, c) FPSC Reproduced with permission.<sup>[134]</sup> Copyright 2018, Elsevier d) CFSC, Reproduced with permission.<sup>[135]</sup> Copyright 2018, Elsevier, and e) RFSC, Reproduced with permission.<sup>[191]</sup> Copyright 2018, Elsevier.

hierarchical porous architecture in the 1D fiber electrode is an effective solution to address these issues. Based on this concept, Zhang et al. designed a composite fiber (PHCFs) with good porosity and hollowness.<sup>[132]</sup> To add up electrical conductivity of the fiber, PANI was composited electrochemically to form PHCFs@PANI electrode. This electrode delivered an aerial capacitance of  $2723 \text{ mF cm}^{-2}$  at a scan rate of  $2 \text{ mV s}^{-1}$ . For realization of the true performance of the electrode, a symmetric PFSC was assembled by keeping two PHCF electrodes in parallel and coating with PVA/ $\text{H}_2\text{SO}_4$  gel electrolyte. This device exhibited a highest energy density of  $55.3 \text{ } \mu\text{Wh cm}^{-2}$  at a power density value  $447 \text{ } \mu\text{W cm}^{-2}$  along with 95% capacitance retention even after 20 bending cycles.<sup>[132]</sup>

Graphene fibers (GFs) have been widely adopted in PFSCs due to their wide availability, low price, facile functionalization, and tailorable structure.<sup>[136]</sup> Theoretically, GFs possess high specific surface area of  $2630 \text{ m}^2 \text{ g}^{-1}$ , but only a low surface area of only  $13.4\text{--}35.8 \text{ m}^2 \text{ g}^{-1}$  originating from the restacking phenomenon is obtained in graphene sheets.<sup>[137]</sup> This reduced surface area of GFs lowers the ion interaction active area and decreases the charge storage ability. Enhancing the porosity by adding carbon-based material is an effective method to address this problem. Zheng et al. fabricated a hierarchically porous GF-based electrode with core–sheath structure by introducing carbonized phenol formaldehyde into it.<sup>[138]</sup> The hierarchically porous structure facilitated ion transport and storage ability and good electrical conductivity in the developed electrode. A symmetrical PFSC was fabricated and it exhibited a specific capacitance of  $311.2 \text{ mF cm}^{-2}$  at a current density of  $0.1 \text{ mA cm}^{-2}$ ,

with a potential window of  $0.8 \text{ V}$  in PVA/ $\text{H}_2\text{SO}_4$  electrolyte. The maximum energy density delivered by this device was  $66.4 \text{ } \mu\text{Wh cm}^{-2}$  at a power density value  $540 \text{ } \mu\text{W cm}^{-2}$  in an organic electrolyte.<sup>[138]</sup> Further, Lu et al. introduced holey graphene in N-doped 3D porous GFs for complete exploitation of graphene.<sup>[139]</sup> The 3D hierarchical porous structure of the GF provided fast electrolyte ion diffusion, whereas N-doping and holey graphene impeded the restacking of the graphene sheets and provided high charge storage efficiency. This optimal GF, i.e., N-doped 40% holey graphene revealed reliable electrochemical performance when assembled into a symmetric PFSC. This device exhibited 95.65% capacitance retention even after 10 000 cycles.<sup>[139]</sup>

CFs are also used as current collectors for supercapacitor fabrication due to their good electrical conductivity, high mechanical stability, lightweight, and low price. However, FSCs based on CFs usually show poor efficiency due to low mass loading over CF current collectors. Gong et al. electrochemically fabricated CNT/ $\text{MnO}_2$  hybrids with an optimal thickness of  $1.44 \text{ } \mu\text{m}$  coated over the CF.<sup>[140]</sup> The symmetric PFSC delivered a high specific energy of  $8.14 \text{ mWh cm}^{-3}$  and an optimum specific power of  $463.8 \text{ mW cm}^{-3}$  in PVA/LiCl electrolyte.<sup>[140]</sup> Apart from CNT/ $\text{MnO}_2$ , various composite materials embedding 3D porous transition metal oxides (TMOs) have also been combined with CFs. A unique approach was adopted by Liu et al. to fabricate negative electrode in flexible FSCs.<sup>[141]</sup> They applied sulfur (S)-doping to atomically modulate  $\text{MoO}_3$  and prepared S- $\text{MoO}_{3-x}$  nanobelts, which improved the charge storage capacity. The oxygen vacancies created in  $\text{MoO}_3$  upon S-doping

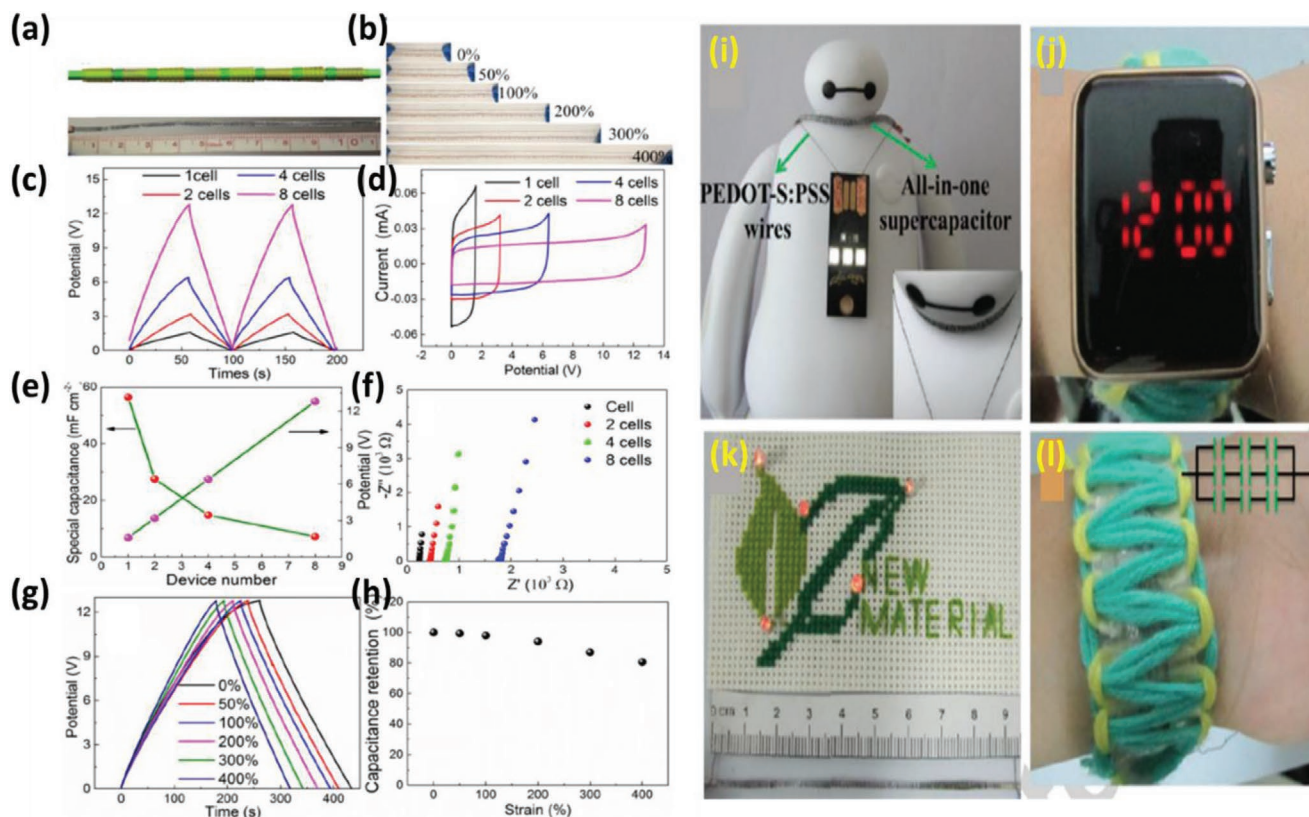


**Figure 16.** a) Pictorial display and digital image of T-SFSSs assembled of eight SFSSs connected in series. b) Image of T-SFSSs assembled of SFSSs connected in series under ascending strains from 0% to 400%. c) The GCD curves of the T-SFSSs with 1, 2, 4, and 8 SFSS cells connected in series quantified at  $1 \text{ mA cm}^{-2}$  current density. d) CV profiles of T-SFSSs with the ascending cells at  $50 \text{ mV s}^{-1}$  scan rate. e) Curves of voltage and capacitance versus device number. f) Nyquist plots of T-SFSSs assembled of 1, 2, 4, and 8 cells connected in series. g) GCD curves of T-SFSSs assembled of eight SFSSs connected in series under ascending strains from 0% to 400%. h) Capacitance retention versus tensile strain from GCD profiles. i) Digital photos of T-SFSSs to glow a commercial USB light. j) Digital image of the T-SFSSs assembled of three SFSSs connected in series to glow a logo abbreviation with five LEDs. k) Digital image of a digital watch powered by three T-SFSSs connected in series woven into a fabric. Reproduced with permission.<sup>[134]</sup> Copyright 2018, Elsevier.

acted as shallow donors increasing the carrier concentration and charge transport kinetics. The fabricated asymmetric PFSC  $\text{MnO}_2/\text{TiN}/\text{S-MoO}_{3-x}/\text{CF}$  showed a high volumetric energy of  $2.79 \text{ mWh cm}^{-3}$  in PVA/LiCl gel electrolyte.<sup>[141]</sup>

CPs such as PEDOT:PSS are used in fibers well known for their high flexibility, good chemical stability, and excellent film forming nature.<sup>[142]</sup> However, the poor electrical conductivity and specific capacitance of PEDOT:PSS are bottlenecks for its successful application in SCs.<sup>[143]</sup> Hybridization or deposition of conductive material over PEDOT:PSS may boost up the electrical conductivity and specific capacitance. Li et al. fabricated a rGO-PEDOT:PSS composite via wet-spinning method.<sup>[144]</sup> The presence of PEDOT:PSS helped avoid restacking of rGO nanosheets whereas rGO improved the electrical conductivity (up to  $590 \text{ S cm}^{-1}$ ) of the composite electrode, which also possessed high flexibility, mechanical strength, enhanced electrolyte absorbing capacity, and good electrochemical performance. A symmetric PFSC was designed using PVA/ $\text{H}_3\text{PO}_4$  gel electrolyte and the device displayed a high specific capacitance of  $131 \text{ mF cm}^{-2}$  at current density of  $20 \text{ } \mu\text{A cm}^{-2}$  and maximum specific energy value  $4.55 \text{ } \mu\text{Wh cm}^{-2}$ . This highly wrinkled PFSC also possessed excellent stability against various

mechanical deformations.<sup>[144]</sup> The proper functionality of FSCs relies on the ability to stretch or bend the device without affecting the electrochemical performance. An acid ( $\text{H}_2\text{SO}_4$ ) modified PEDOT:PSS-based fiber was designed by Wang et al. to achieve high stretchability.<sup>[134]</sup> These electrodes, exhibited a tensile strength of  $112.7 \text{ MPa}$  and an electrical conductivity of  $1771.8 \text{ S cm}^{-1}$ . A symmetric PFSC device assembled using this electrode showed a high specific energy of  $41.1 \text{ } \mu\text{Wh cm}^{-2}$  at a specific power of  $3520 \text{ } \mu\text{W cm}^{-2}$  with exceptional capacitance retention up to 400% elongation (Figure 16).<sup>[134]</sup> Apart from PEDOT:PSS, other CPs such as PANI, PPy, polyacetylene (PA), and polythiophenes (PTs) have been used as electrode materials due to their good intrinsic electrical conductivity.<sup>[145]</sup>

Freestanding fiber electrodes may provide good electrical conductivity because of their superior ion transportation behavior. For flexible FSCs, aerogels have been considered as good freestanding electrodes with excellent mechanical stability to deformation. Serrapede et al. synthesized a hematite:rGO composite-based aerogel via hydrothermal method for FSC electrode application.<sup>[146]</sup> An asymmetric PFSC was also fabricated using  $\text{MnO}_x$  as positive electrode and the device delivered very good flexibility with excellent electrochemical performance. Another

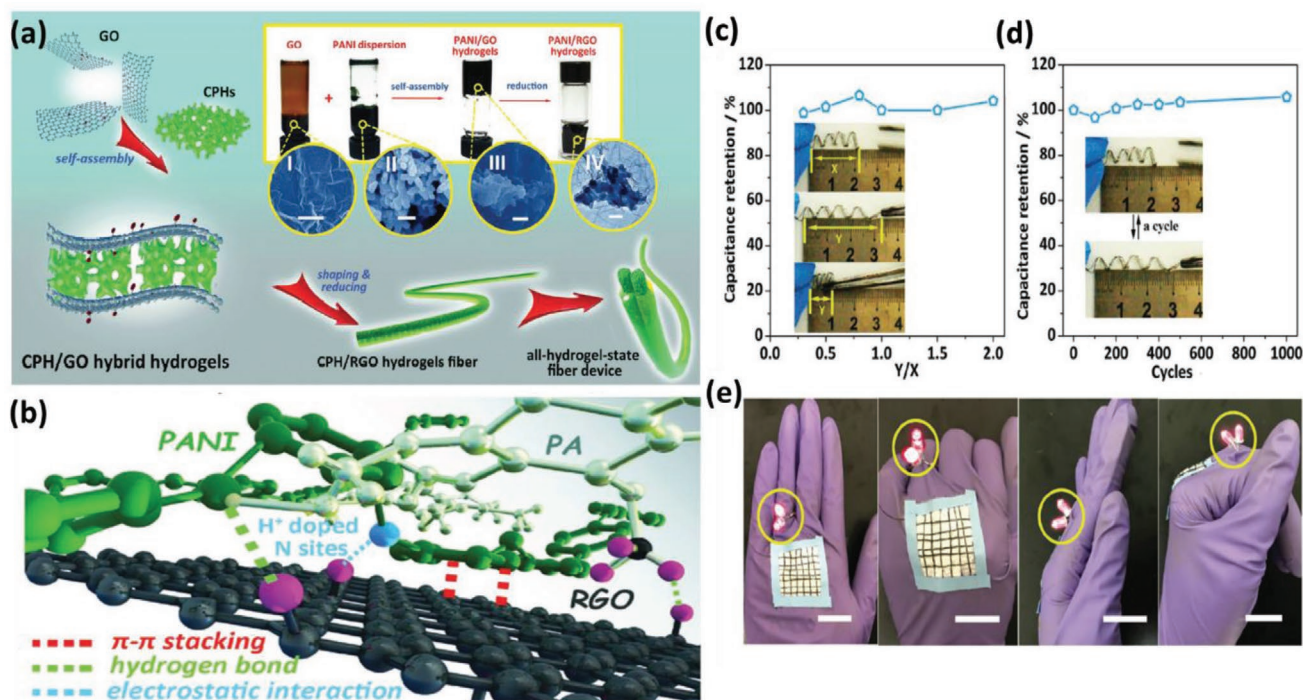


**Figure 17.** a) Pictorial display of PANI/GO hybrid hydrogels preparation followed by shaping/reduction process, b) black: RGO; green: PANI chain; silver white: PA molecule; purple: oxygen contained groups. c,d) The elasticity of the spring-like device. e) A display of a synthesized yarn glowing two LEDs in the actual and bending states (the scale bars are 2 cm). Adapted with permission.<sup>[16]</sup> Copyright 2018, John Wiley & Sons.

freestanding fiber electrode was assembled by He et al. by using rGO and MXene hybrid through wet spinning approach.<sup>[147]</sup> These highly conductive 2D nanosheets proved to be excellent fiber electrodes for FSC application. A nonvolatile  $\text{H}_2\text{SO}_4$  electrolyte was inserted into the layers of MXene and rGO to enhance the ion access in the inner pores of these fibers. A symmetric PFSC was also developed and it delivered a volumetric energy of  $12 \mu\text{Wh cm}^{-2}$  at a power density of  $8.8 \text{ mW cm}^{-2}$  with 85% capacitance retention after 10 000 GCD cycles.<sup>[147]</sup> A MWCNT–PEDOT:PSS hybrid solution was employed by Meng et al. to develop a freestanding fiber electrode via a wet spinning method.<sup>[148]</sup> By regulating the percentage of MWCNT in the solution, the electrical conductivity of the electrode was highly improved up to  $1394 \text{ S cm}^{-1}$ . The fabricated PFSC delivered a maximum specific energy of  $16.3 \mu\text{Wh cm}^{-2}$  and 87% capacitance retention after 1000 bending cycles.<sup>[148]</sup> Natural fibers could also be used in these freestanding electrodes owing to their various features such as good weavability, high flexibility, low cost, and abundance. *Bombyx mori* silks were adopted as fiber current collector by Song et al. upon coating carboxyl mediated MWCNT:PANI composite over them.<sup>[149]</sup> The fabricated electrode, PANI@F-MWCNT@silks revealed the highest areal capacitance of  $95.5 \text{ mF cm}^{-2}$  at a current density of  $5.3 \text{ mA cm}^{-2}$ , with 33% elongation efficiency and 225 MPa tensile strength. Further, a symmetric PFSC was derived using this electrode and it demonstrated the highest energy density of  $1.22 \text{ mWh cm}^{-2}$  at a specific power of  $127 \text{ mW cm}^{-2}$  in PVA/ $\text{H}_3\text{PO}_4$  electrolyte.<sup>[149]</sup> However, most freestanding films and fibers are based on rGO, which undergoes restacking and clumpy pore size distribution and thus provides poor

electrochemical efficiency. The formation of 3D graphene CP hydrogel (CPH) by self-assembly of rGO nanostructures and CPHs by Li et al. resulted in high performing FSC electrode.<sup>[16]</sup> The as-fabricated PFSC device with the structure rGO/PANI/rGO/PANI in PVA/ $\text{H}_2\text{SO}_4$  electrolyte exhibited a high volumetric energy of  $8.8 \text{ mWh cm}^{-3}$  at a power density of  $30.77 \text{ mW cm}^{-3}$ , with magnificent stability up to 86% capacitance retention even after 17 000 charge–discharge cycles and mechanical strength (strain  $\approx 40\%$ )<sup>[16]</sup> (Figure 17).

Metal wires possess high conductivity which makes them excellent candidates for freestanding fibers for FSCs although they have poor flexibility and high resistance to mechanical deformations. Introducing heterogenous porous architectures in metal wires and depositing electroactive materials in them may uplift their electrochemical performance by promoting their specific surface area, flexibility and mechanical stability. Wang et al. assembled a symmetric PFSC device by using  $\text{MnO}_2$  deposited over direct flame and implemented on micrometer cellular Ni wire (MPNW) and PVA/ $\text{Na}_2\text{SO}_4$  gel electrolyte.<sup>[150]</sup> Similarly, a bimetallic sulfide ( $\text{CuCo}_2\text{S}_4$ ) was directly prepared over Ni NW via hydrothermal synthesis to fabricate  $\text{CuCo}_2\text{S}_4/\text{NW}$  electrode, which exhibited an optimal areal capacitance of  $367 \text{ mF cm}^{-2}$  at a current density of  $0.5 \text{ mA cm}^{-2}$ .<sup>[151]</sup> The as-assembled symmetric PFSC derived a maximum specific energy of  $7.2 \mu\text{Wh cm}^{-2}$  at a specific power of  $599.9 \mu\text{W cm}^{-2}$  in PVA/KOH gel electrolyte.<sup>[151]</sup> Furthermore, to create strong attachment between the current collector and active material, a Ni wire was converted into NiO, which acted as a strong nanogluue to grow MnCo-layered double hydroxide (LDH) over it. This NiO layer added supplementary capacitance to the overall

electrode. The asymmetric PFSC (NiO@MnCo-LDH//AC) by Gao et al. exhibited a high specific energy of  $0.0198 \text{ mWh cm}^{-2}$  at a specific power of  $0.38 \text{ mW cm}^{-2}$  in PVA/KOH gel electrolyte.<sup>[152]</sup> Employing a bimetallic 3D conductive network could result in decreased contact resistance, faster ion diffusion, and better ion intercalation and deintercalation.<sup>[153]</sup> For example, Zhang et al. derived 3D N-doped carbon composited  $\text{Fe}_2\text{O}_3$  nanocubes derived from metal-organic framework (MOF) over CFs via binder-free method.<sup>[154]</sup> This unique fiber was fabricated by high-temperature annealing of PPy nanowire-deposited CFs under  $\text{N}_2$  atmosphere. The negative electrode exhibited a volumetric capacitance of  $39.6 \text{ mF cm}^{-3}$  at a scan rate  $10 \text{ mV s}^{-1}$ . An asymmetric PFSC  $\text{MnO}_2@\text{TiN}/\text{Fe}_2\text{O}_3/\text{NCWs}/\text{CFs}$  also showed 75.5% capacitance retention even after 5000 cycles with a high energy density of  $2.7 \text{ mWh cm}^{-3}$  in LiCl-PVA electrolyte.<sup>[154]</sup> Yarn-based fibers are excellent current collectors for FSCs due to their high flexibility, lightweight, and cost-effectiveness. However, the less surface area of interaction between the active material and current collector impedes the energy density in yarn-based FSCs. Vertically aligned 3D structure with pseudocapacitive nature could be grown directly over SC yarns to improve their specific surface area. This strategy was applied by Le et al. to fabricate NiCo-OH/ZnO-nanorod (NR)/CNT yarn electrode by coating ZnO NRs over CNT yarns and then growing NiCo-OH over them.<sup>[155]</sup> A symmetric PFSC designed by this elec-

trode exhibited 100% capacitance retention after  $150^\circ$  bending angle and a maximum energy density of  $0.897 \text{ } \mu\text{Wh cm}^{-2}$  at power density of  $1170 \text{ } \mu\text{W cm}^{-2}$  in PVA-LiOH gel electrolyte.

Several nanocarbons are being adopted as scaffold for SC application. However, their low specific capacitance and poor long-term stability are the bottlenecks in achieving efficient electrochemical performance. Using metal nanotube array as electrode template may provide excellent surface area and remarkable cyclability. Li et al. assembled a titanium nanotube arrays (TNTAs) as the template for fiber like electrode.<sup>[156]</sup> The wide bandgap issue of  $\text{TiO}_2$  ( $\approx 3.2 \text{ eV}$ ) was addressed via advanced interfacial engineering, i.e., with S-doping of TNTAs.<sup>[157,158]</sup> PANI was further coated over TNTAs to avail the electrode with flexibility, conductivity, and structural stability. The as-prepared PANI/S-TiO<sub>2</sub> electrode was used to fabricate a symmetric PFSC in PVA-H<sub>3</sub>PO<sub>4</sub> electrolyte, which delivered maximum specific capacitance of  $91.9 \text{ mF cm}^{-2}$ , an energy density of  $3.2 \text{ } \mu\text{Wh cm}^{-2}$  and 93.8% capacitance retention even after 12 000 charge-discharge cycles<sup>[156]</sup> (Figure 18). A novel strategy was followed by Wang et al. to address sluggish charge storage kinetics, slow ion diffusion due to the thickening of electrolytes, and decomposition of active material from the current collector in FSCs at extreme climatic condition.<sup>[159]</sup> This group adopted a core-shell conductive polymer electrode coated with  $\text{RuO}_2$  in between, where the outer PEDOT:PSS layer

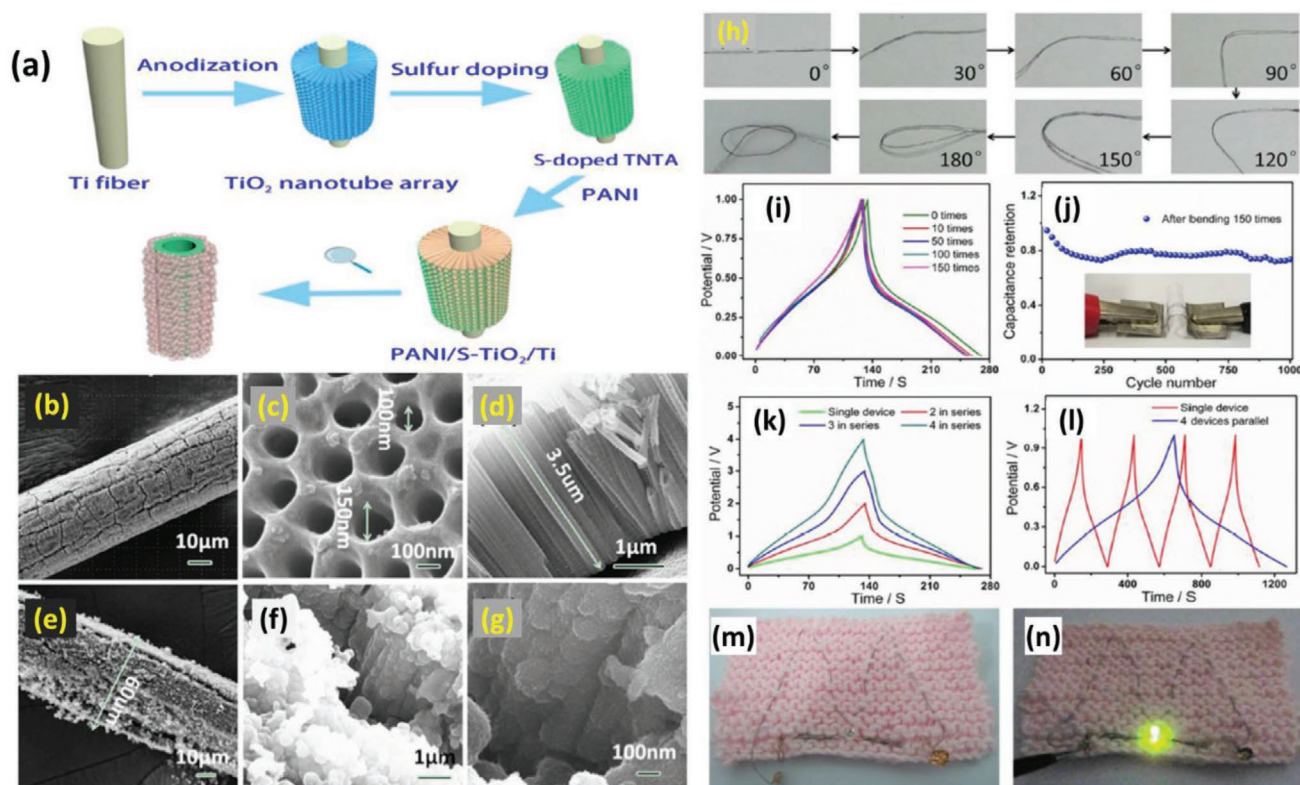


**Figure 18.** a) Pictorial depiction of the step-by-step preparation of the PANI/S-TiO<sub>2</sub>/Ti fiber. b–d) SEM photographs of the top and cross-section of the S-TiO<sub>2</sub>/Ti fiber. e–g) SEM pictures of the top and cross-section of the PANI/S-TiO<sub>2</sub>/Ti fiber. h) Digital images of the PFSCs at various bending angles and a tied PFSC. i) GCD profiles at current density of  $0.2 \text{ mA cm}^{-2}$  after several bending cycles. j) Cycling stability test of the PFSCs after 150 bending cycles at  $0.2 \text{ mA cm}^{-2}$  (inset shows a digital image of the PFSCs at a bending angle of  $180^\circ$ ). k, l) GCD profiles of the four PFSC devices connected in series and parallel at a current density of  $0.2 \text{ mA cm}^{-2}$ . m, n) Digital pictures of the letter “M” woven on a cotton fabric surface, and all-solid-state PFSCs woven on cotton fabric glowing a green LED. Reproduced with permission.<sup>[156]</sup> Copyright 2018, American Chemical Society.

worked as the current collector and obstructed the electrode from pulverization and the inner PEDOT:PSS/RuO<sub>2</sub> provided sufficient electrical conductivity and pseudocapacitive behavior. The as-fabricated symmetric PFSC revealed high energy density values of 14.2 and 22.9 μWh cm<sup>-2</sup> at temperatures -60 and 75 °C, respectively, in LiCl-PVA gel electrolyte.<sup>[159]</sup>

The use of aqueous electrolyte for FSC application is safe, environmentally friendly, and easy to synthesize.<sup>[247–252]</sup> However, the working potential window of these electrolytes is limited only up to 1.23 V, i.e., (water decomposition potential).<sup>[160]</sup> Organic electrolytes could work in the potential range of 3 V but their complex synthesis, toxicity and noneco-friendliness restrict their use in FSCs.<sup>[161]</sup> An effective solution to overcome this issue is to enhance the stability of aqueous electrolytes by exceeding the oxygen evolution reaction and hydrogen evolution reaction overpotential by incorporating a high concentration of active ions to combine with water to modulate its hydration energy.<sup>[162]</sup> Liu et al. fabricated water-in-salt gel polymer electrolyte with optimized ion concentration (8.96 M LiCl/PVA) and incorporated a N-doped RGO fiber (NRGF) with wrinkled surface morphology.<sup>[162]</sup> The high concentration of Li<sup>+</sup> ions combined with water (Li<sup>+</sup> H<sub>2</sub>O) improved the hydration energy of water and thus provided a wide potential window of 2.2 V to the symmetric PFSC. The maximum energy density achieved by this quasi-solid-state PFSC was 25.6 μWh cm<sup>-2</sup>, with 84% capacitance retention even after 20 000 GCD cycles.<sup>[162]</sup>

### 5.1.2. TFSCs

In the case of TFSCs, the fiber-shaped cathode and anode are twisted with each other and precoated with gel electrolyte. CNTFs are promising fiber candidates owing to their appreciable electrical conductivity, high flexibility, good surface area, and lightweight.<sup>[5,163]</sup> Instead of using bare CNTFs, composites with electroactive materials could potentially enhance the potential window of device and thus the overall electrochemical performance. The interfacial growth of 3D electroactive structure of CNTFs may endow the electrode with high electrical conductivity, appreciable specific surface area, high structural stability, and good energy density.<sup>[164,165]</sup> Direct deposition of ternary metal oxides over CNTFs enabled efficient flexible electrode for supercapacitor application. Multiple metals possessing various oxidation states could induce redox reaction mechanisms and fast charge–discharge ability. Accordingly, Guo et al. adopted solvothermal synthesis followed by annealing to grow Zn–Ni–Co oxide nanowires over CNTFs as positive electrode and vanadium nitride (VN) over CNTFs as a potential negative electrode to assemble a TFSC device.<sup>[133]</sup> This device showed a wide potential range of 1.6 V in PVA/KOH electrolyte while maintaining a high volumetric capacitance of 50 F cm<sup>-3</sup> and specific energy of 1778 mWh cm<sup>-3</sup> (53.33 μWh cm<sup>-2</sup>). Further, it sustained 91% of its original specific capacitance even after 3000 bending cycles at 90° bending angle.<sup>[133]</sup> Wang et al. synthesized a manganese–nickel–cobalt–sulfide (MNCS) hybrid with CNTFs forming a nanotube array morphology.<sup>[166]</sup> The fabricated MNCS NTAs/CNTF electrode exhibited maximum volumetric capacitance of 2554.5 F cm<sup>-3</sup> and an asymmetric TFSC device was fabricated using VN coated CNTF as negative electrode. The assembled TFSC delivered a high specific capacitance of 1473 F cm<sup>-3</sup> and a

specific energy of 52.4 mWh cm<sup>-3</sup> in PVA/KOH gel electrolyte with a 1.6 V potential window. Even after 5000 bending cycles, this device retained 92.9% of its original capacitance value, thus proving itself as an excellent FSC.<sup>[166]</sup> A hierarchical nanowire array (HNWA) morphology could endow the electrode with huge active sites for ion intercalation and deintercalation, fast ion electron path length and high energy density. Wang et al. designed Ni(OH)<sub>2</sub>-wrapped NiCo<sub>2</sub>O<sub>4</sub>, i.e., HNWA over CNTF as positive electrode and VN/CNTF as negative electrode.<sup>[167]</sup> The assembled TFSC showed a maximum areal energy of 103.8 μWh cm<sup>-2</sup> with 90% capacitance retention even after 3000 bending cycles in PVA/KOH gel electrolyte.<sup>[167]</sup>

As in the case of PFSCs, many TFSCs use CPs, such as PPy microfibers, which could not achieve competitive electrochemical performance due to their poor conductivity unless they are hybridized with carbon-based materials. Mo et al. conducted wet-spinning synthesis to assemble cellulose nanofibers (CNFs) modified with graphene/PPy as an FSC electrode.<sup>[168]</sup> These CNFs played the role of spacer between the graphene sheets and enabled strong hydrogen bond interactions to toughen the interlaminar force between the sheets. The fabricated microfibers possessed a tensile strength of 364.3 MPa and the assembled symmetric TFSC delivered a high areal capacitance of 218 mF cm<sup>-2</sup> at a current density of 0.1 mA cm<sup>-2</sup> in PVA/H<sub>3</sub>PO<sub>4</sub> gel electrolyte.<sup>[168]</sup> Conjugated microporous polymers (CMPs) are novel materials formed by expanded π-conjugation and persistent porosity; they exhibit tailored porosity, huge specific surface area, redox reaction ability, and excellent chemical stability.<sup>[169]</sup> The high surface area benefits the storage of large amount of charge, whereas the implementation of several atoms possessing redox active sites provides pseudocapacitive nature to these materials.<sup>[170]</sup> The major bottleneck in their implementation in FSCs is their inherent insolubility. Therefore, Lyu et al. directly grafted CMPs over CNTFs and the as-prepared electrode exhibited a maximum specific capacitance of 671.9 mF cm<sup>-2</sup> at a current density of 1 mA cm<sup>-2</sup>.<sup>[171]</sup> The assembled symmetric TFSC demonstrated a high energy density of 18.33 μWh cm<sup>-2</sup> at a power density of 0.99 mW cm<sup>-2</sup>, with 84.5% capacitance retention even after 10 000 bending cycles.<sup>[171]</sup>

Various novel materials such as holey tungsten oxynitride nanowires,<sup>[172]</sup> MOFs, MXenes, LDHs, CFs,<sup>[173]</sup> and GFs<sup>[174]</sup> have been recently applied as fiber-shaped current collectors for assembling TFSCs.<sup>[175,176]</sup> MOFs provide excellent specific surface area, good porosity, and tailored structures and they may form electrodes with good charge storage ability and ample ion diffusion pathway.<sup>[175]</sup> The binder-free growth of MOF from metal oxides over flexible current collectors is an effective method to achieve high performance FSCs. Zhou et al. fabricated a MIL-88-Fe (iron-based MOF) derived from α-Fe<sub>2</sub>O<sub>3</sub> through carbonization. This α-Fe<sub>2</sub>O<sub>3</sub>/C was directly grown over CNTF, which possessed a spindle structure.<sup>[177]</sup> Further, this negative electrode underwent S-doping to obtain S-α-Fe<sub>2</sub>O<sub>3</sub>@C/oxidized carbon nanotubes grown on carbon fiber (OCNTF) electrode, which exhibited a high specific capacitance of 1232.4 mF cm<sup>-2</sup> at a current density of 2 mA cm<sup>-2</sup>. A TFSC was designed using Na–MnO<sub>2</sub> NS<sub>s</sub>/CNTF via binder-free method. The asymmetric TFSC delivered maximum areal capacitance and energy density of 201.3 mF cm<sup>-2</sup> and 135.3 μWh cm<sup>-2</sup>, respectively, with 97.1% capacitance retention even after 4000 bending cycles at 90°.<sup>[177]</sup>

Various surface-treated flexible polymer fibers co-deposited with electroactive materials have also been proven to be beneficial electrodes for TFSCs. Ba et al. utilized commercial polyethylene terephthalate (PET) thread as template to coat CuS followed by PANI via chemical bath deposition and electro-deposition.<sup>[178]</sup> The cost-effectiveness, chemical inertness, high mechanical strength, and abundance of PET has caught the attention of research groups working in the field of FSCs.<sup>[179]</sup> The fabricated PANI/CuS/PET electrodes twisted together to form a symmetric TFSC and this device delivered a high specific capacitance of  $29 \text{ mF cm}^{-2}$  and 93.1% capacitance retention after 1000 cycles in PVA- $\text{H}_3\text{PO}_4$  electrolyte.<sup>[178]</sup> The high electrical conductivity of PANI is favorable in aiding high specific capacitance to the electrode. In another attempt, a core-sheath porous structure that consisted of 1D PANI nanorods, which relieved the volume expansion during the charge-discharge process offered good stability to the electrode<sup>[180]</sup> (Figure 19). The assembled symmetrical TFSC provided the highest specific capacitance of  $3571 \text{ mF cm}^{-2}$  and a maximum areal energy density of  $7.93 \text{ } \mu\text{Wh cm}^{-2}$  in PVA/ $\text{H}_2\text{SO}_4$  electrolyte.<sup>[180]</sup> Moreover, Zhao et al. designed a high-performance flexible electrode by dry spinning a PANI coating over Au nanowires.<sup>[181]</sup> A symmetrical TFSC, which was stretchable up to 360% with a specific capacitance of  $16.8 \text{ mF cm}^{-2}$ , was devised using this electrode.

With continuous efforts to improve the electrochemical performance of FSCs, various novel strategies are being adopted

by many research groups. For example, Gao et al. employed commercially available sewing threads as fiber to derive TFSC.<sup>[182]</sup> In situ polymerization was adopted to coat PEDOT over the threads. Consequently,  $\text{MnO}_2$  was covered over these conductive threads electrochemically. Finally, one additional PEDOT layer was coated over it. A symmetric TFSC PEDOT/ $\text{MnO}_2$ /PEDOT//PEDOT/ $\text{MnO}_2$ /PEDOT exhibited a maximum areal capacitance value of  $132.02 \text{ mF cm}^{-2}$  with knittability and stability in PVA/LiCl electrolyte.<sup>[182]</sup> Furthermore, phosphorization and sulfurization were proven to be fruitful in achieving reliable flexible electrodes for FSCs. Liu et al. fabricated iron oxide nanowire arrays ( $\text{Fe}_2\text{O}_3$  NWAs) over CNTFs and this electrode underwent phosphorization and sulfurization to prepare FeP and  $\text{FeS}_2$  NWAs, respectively.<sup>[183]</sup> These negative electrodes possessed a maximum areal capacitance of  $1135 \text{ mF cm}^{-2}$  (FeP) and  $833 \text{ mF cm}^{-2}$  ( $\text{FeS}_2$ ) at a current density of  $1 \text{ mA cm}^{-2}$ . With excellent weavability and mechanical flexibility, the assembled asymmetric TFSCs, FeP NWAs/ $\text{MnO}_2$  CNTF, and  $\text{FeS}_2$  NWAs/ $\text{MnO}_2$  CNTF showed high energy density values of 23.4 and  $18.72 \text{ mWh cm}^{-3}$  in LiCl-PVA electrolyte, respectively.<sup>[183]</sup>

### 5.1.3. CFSCs

CFSCs consist of a core fiber electrode where an active material is coated followed by coating of gel electrolyte. CFs are widely

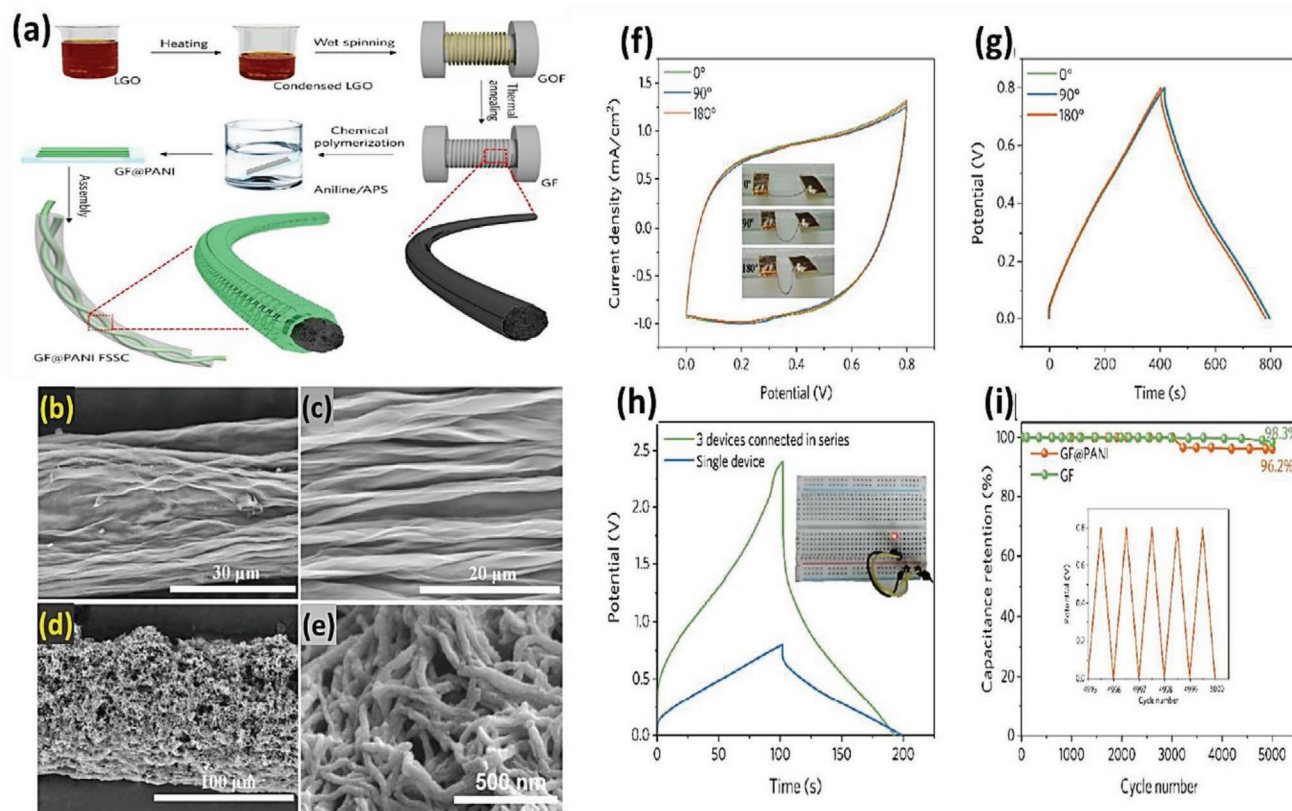


**Figure 19.** a) Step-by-step synthesis of GF@PANI, the assembled full cell, and the morphology of GF@PANI. b,c) Longitudinal SEM picture of GF. d,e) Longitudinal SEM photo of GF@PANI. f) CV profiles and g) GCD profiles of GF@PANI-based FSSC at different bending angles. h) GCD profiles of single and three GF@PANI FSSCs in series connection. i) Stability test of GF and GF@PANI FSSCs ( $1 \text{ mA cm}^{-2}$ ). Reproduced with permission.<sup>[180]</sup> Copyright 2019, American Chemical Society.

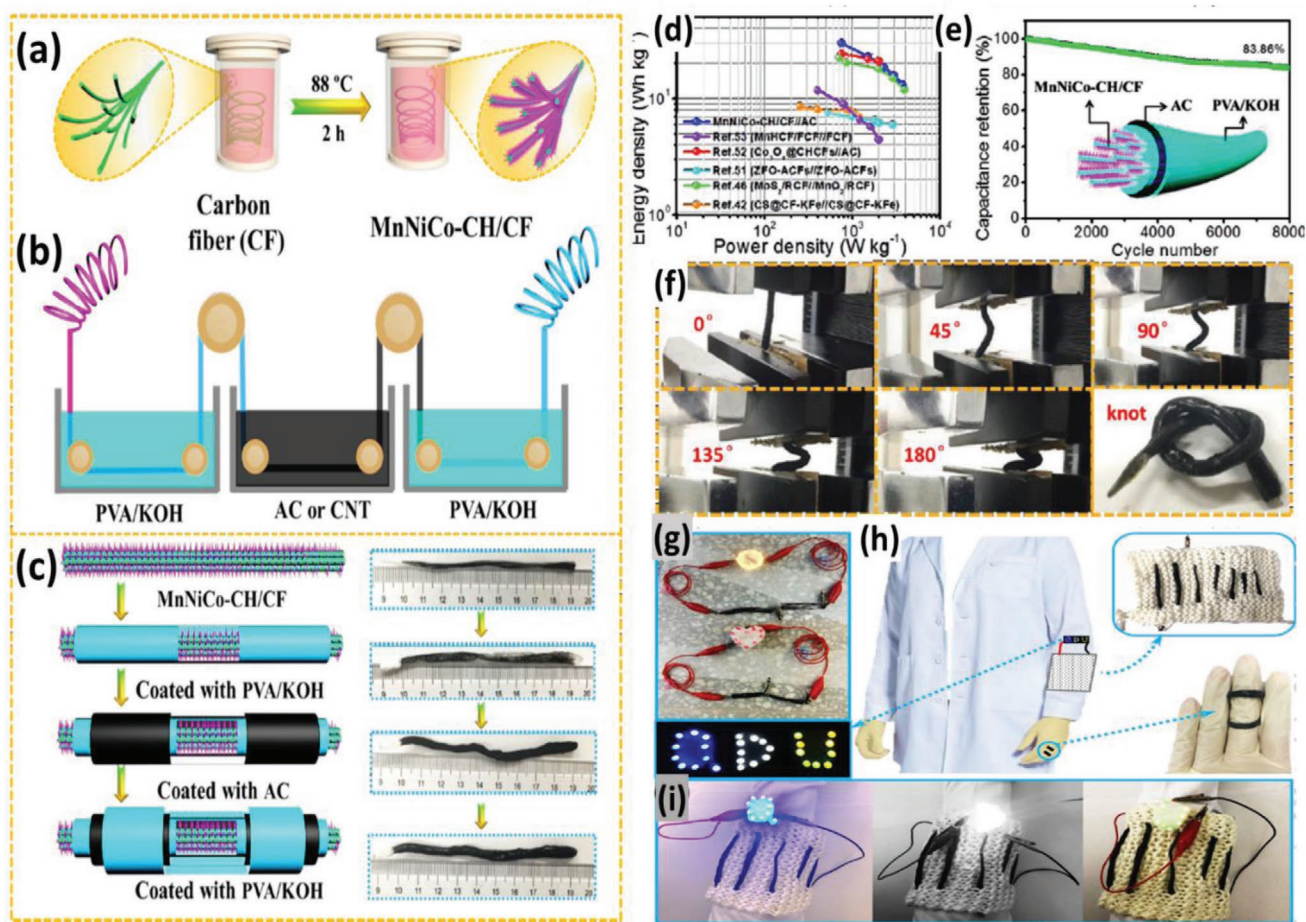


**Figure 20.** Graphical depiction of a) synthesis of MnNiCo-CH nanoneedles array on CFs and b) fabrication method of CFSC. c) Step-by-step graphical (left) and photos (right) of the fabrication process of the CFSC. d) Ragone profile of the CFSC. e) Stability test of CFSC at  $5 \text{ A g}^{-1}$ . f) Pictures of the CFSC under different bending conditions. Designed applications of the CFSCs: g) two CFSCs in series connection glowing different shaped LEDs; h) seven CFSCs stitched into the cotton fabrics and attached in series and parallel connection to glow LEDs; i) seven CFSCs connected in group of series and parallel glowing "Q", "D", "U" LEDs, respectively. Reproduced with permission.<sup>[187]</sup> Copyright 2020, The Royal Society of Chemistry.

used in CFSCs due to their flexibility, mechanical strength, low mass, and good electrical conductivity.<sup>[184]</sup> The binder-free deposition of high-performance electroactive materials over these CFs was proven as an excellent strategy to achieve reliable FSCs.<sup>[135]</sup> For example, a Swiss-roll type CFSC was developed by utilizing  $\text{Fe}_2\text{O}_3/\text{CF}$  and  $\text{MnO}_2/\text{CF}$  electrodes in PVA– $\text{LiClO}_4$  gel electrolyte. A wide potential window of 2.0 V and a high energy density of  $33.1 \text{ Wh kg}^{-1}$  ( $0.16 \text{ mWh cm}^{-3}$ ) at a power density of  $1.32 \text{ kW kg}^{-1}$  was achieved by this CFSC. The device layout diminished the contact resistance between the electrodes, thereby enabling enhanced ion transport between the electrode and electrolyte. The following mathematical relation was adopted to calculate the volume of CFSC:  $\vartheta = \pi(\frac{D}{2})^2 h$ ; where  $\vartheta$  is the volume of the device,  $D$  is the device diameter, and  $h$  is the length of the full cell.<sup>[135]</sup> A significant difference in the equivalent series resistance  $12.6$  and  $19.7 \Omega$  was observed in CFSC and PFSC assembled using the same electrodes, respectively.

High performance sustainable FSCs require a wide potential window, a firm attachment of the active material with the current collector, an ample area of interaction between the electrode and maintenance of uniform distance between them to avoid

short circuit, proper device packaging to avoid leakage current and full flexibility. Patil et al. synthesized  $\text{Fe}_2\text{O}_3$  over CF and  $\text{MnO}_2$  over CNT-web paper via binder-free method to achieve all these criteria in a single FSC device.<sup>[185]</sup> The as-fabricated  $\text{Fe}_2\text{O}_3/\text{CF}/\text{MnO}_2/\text{CNT}$  asymmetric CFSC achieved an energy density of  $0.43 \text{ mWh cm}^{-3}$  at a specific power of  $0.02 \text{ W cm}^{-3}$  in PVA– $\text{LiClO}_4$  electrolyte. With a wide potential window of 2.2 V, this device retained 80% of its initial specific capacitance even after 10 000 charge–discharge cycles.<sup>[185]</sup> Multiple TMO hybrids with hydroxides or carbonate hydroxides prepared by doping diversified metal cations into the host can lead to electrodes with superior electrochemical performance due to multiple redox sites that favor high ion intercalation–deintercalation efficiency.<sup>[186]</sup> Binder-free coatings of these multi metal oxide/hydroxide and carbonate hydroxide composites over flexible conductive CFs may furnish 3D hierarchical arrays with core–shell structure. For example, a Mn, Ni co-substituted cobalt carbonate hydroxide fabricated over CFs (MnNiCo-CH/CF) with nanoneedle array morphology was developed by Cao et al. (Figure 20).<sup>[187]</sup> An asymmetric CFSC (MnNiCo-CH/CF//AC) was assembled, which exhibited wide potential window

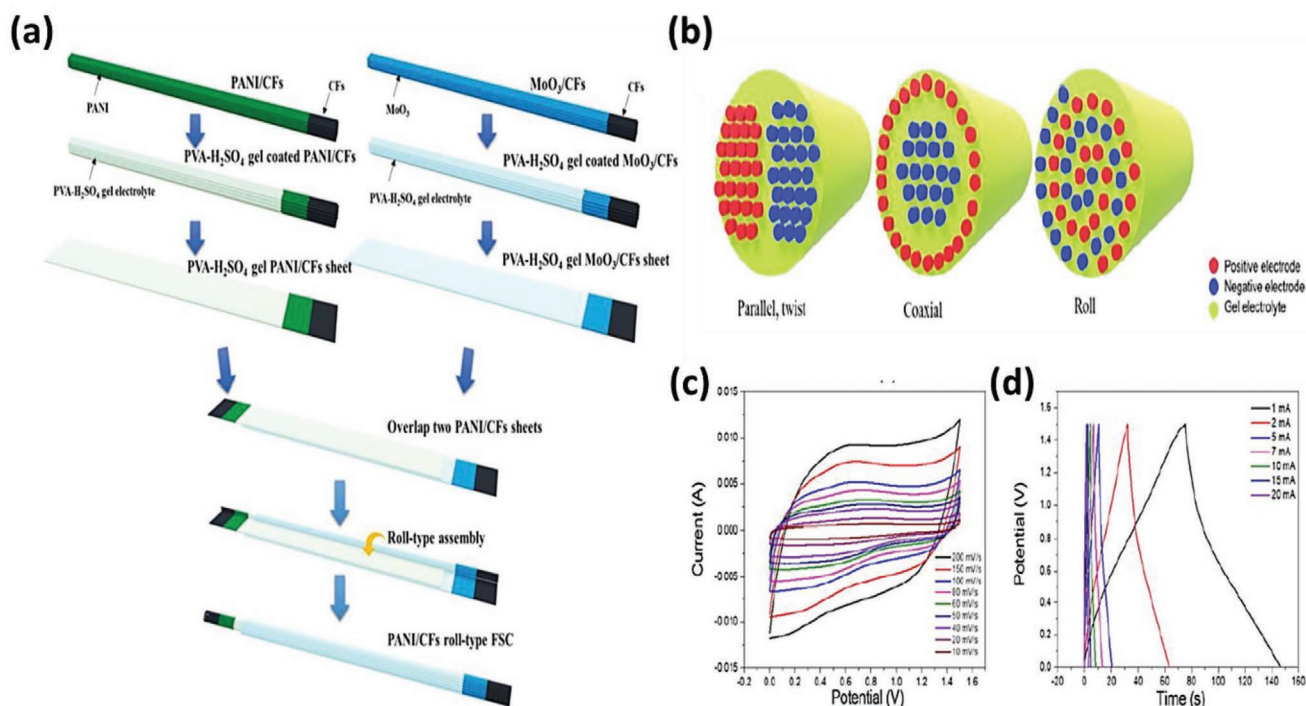


**Figure 21.** a) Pictorial depiction of the method of synthesis of asymmetric RFSCs. b) Cross-sections of parallel and twist-, coaxial-, and roll-type FSCs. c) CV and d) GCD profiles of PANI//MoO<sub>3</sub> RFSC executed in a potential window of 1.5 V. Adapted with permission.<sup>[189]</sup> Copyright 2020, The Korean Fiber Society.

of 1.5 V with a maximum energy density of 30.04 Wh kg<sup>-1</sup> at power density of 749.9 W kg<sup>-1</sup> in PVA/KOH gel electrolyte.<sup>[187]</sup> Additionally, Zhao et al. synthesized 3D MnO<sub>2</sub>@Ni cones over CNTFs,<sup>[188]</sup> and the fabricated 3D MnO<sub>2</sub>@Ni/CNTF electrode delivered a maximum areal capacitance value of 609.06 mF cm<sup>-2</sup> at a current density of 0.5 mA cm<sup>-2</sup>. An asymmetric CFSC was fabricated using MoS<sub>2</sub>/CNTF as negative electrode and the device exhibited a maximum specific capacitance of 195.38 mF cm<sup>-2</sup> at an energy density of 83.59 μWh cm<sup>-2</sup> in PVA/KOH electrolyte.<sup>[188]</sup> CFSCs possess higher electrochemical efficiency than PFSCs and TFSCs. However, CFSCs have some shortcomings related to the separators used in these devices, which usually have high thickness and increase the internal resistance between the electrode and electrolyte. A thickness controlled thin and hugely wrinkled polymer electrolyte was coated over GFs by Yang et al. to address this issue.<sup>[195]</sup> Wet spinning strategy was applied to fabricate PVDF nanofiber as separator for graphene-based CFSCs. The assembled symmetric CFSC showed a maximum energy density of 30.8 μWh cm<sup>-2</sup> with 94% capacitance retention after 10 000 cycles.<sup>[195]</sup>

#### 5.1.4. RFSCs

Two thin-film flexible electrodes are placed one over the other and rolled at a time to form RFSCs (Figure 21). As shown in Figure 21b, the interaction between positive and negative electrodes is higher in CFSCs and RFSCs than in parallel FSCs. CFSCs commonly adopt a concentric circle structure. Thus, effective interactive surface area is formed. However,

their layer-by-layer assembly makes them tedious to fabricate. Therefore, RFSCs are good alternatives to CFSCs as they could provide the same utilization area and ease of synthesis at a time.

Various fiber-like electrodes are used to fabricate RFSCs including metal wires, CNT fibers, polymer@metal fibers, GFs, etc.<sup>[190]</sup> An RFSC was fabricated via chemical deposition synthesis by Yu et al. who employed PANI coated CFs as binder-free flexible conductive electrode.<sup>[191]</sup> This RFSC provided almost three times higher energy density of 2.97 Wh kg<sup>-1</sup> at a power density of 4 kW kg<sup>-1</sup> in H<sub>2</sub>SO<sub>4</sub>/PVA electrolyte than TFSC. As the power density is inversely related to internal resistance ( $R_{int}$ ),<sup>[192]</sup> having low  $R_{int}$  is a measure to achieve high electrochemical performance.<sup>[193]</sup> In the case of RFSCs, the distance between the cathode and anode is consistent and uniform, thus creating good diffusion path length between the electrode and electrolyte, decreased  $R_{int}$ , and increased power density.<sup>[191]</sup> Yu et al. fabricated another asymmetric RFSC by using PANI@CF as positive electrode and MoO<sub>3</sub>@CF as negative electrodes (Figure 23).<sup>[189]</sup> PANI and MoO<sub>3</sub> were coated over CFs via chemical bath deposition. Finally, PVA/H<sub>2</sub>SO<sub>4</sub> gel electrolyte was utilized as electrolyte to the fabricated RFSC. This device exhibited an optimum energy density of 67.51 μWh cm<sup>-3</sup> and the highest power density of 59.71 mW cm<sup>-3</sup>.<sup>[189]</sup>

Overall, this section summarized the recent progress in FSCs (Table 4), including electrode synthesis and four types of device assembly with strategies to multiply the electrochemical performance. Several FSCs have been designed and incorporated as smart wearable textiles. However, their specific capacitance and energy density are inferior to the conventional planar

**Table 4.** Overview of electrochemical performance of different FSCs.

Type of FSC	Electrode	Potential window [V]	Electrolyte	Specific capacitance at current density/scan rate	Maximum energy density at power density	Capacitance retention (cycle numbers)	Refs.
PFSC	S-MoO <sub>3-x</sub> //MnO <sub>2</sub> @TiN	1.8	PVA/LiCl	6.19 F cm <sup>-3</sup> at 0.5 mA cm <sup>-1</sup>	2.79 mWh cm <sup>-3</sup> at 2.11 W cm <sup>-3</sup>	NA	[141]
	MWCNT/PEDOT:PSS//MWCNT/PEDOT:PSS	1.0	PVA/H <sub>3</sub> PO <sub>4</sub>	117.0 mF cm <sup>-2</sup> at 0.1 mA cm <sup>-2</sup>	16.3 μWh cm <sup>-2</sup> at 0.05 mW cm <sup>-2</sup>	90% (2000 cycles)	[148]
	PANI@F-MWCNT@silk//PANI@F-MWCNT@silk	0.8	PVA/H <sub>3</sub> PO <sub>4</sub>	95.5 mF cm <sup>-2</sup> at a current 0.1 mA	1.22 mWh m <sup>-2</sup> at 127 mW m <sup>-2</sup>	80% (under an applied strain of 20%)	[149]
	EM-rGO/MXene//EM-rGO/MXene	0.8	PVA/H <sub>2</sub> SO <sub>4</sub>	304.5 mF cm <sup>-2</sup> at 0.08 mA cm <sup>-2</sup>	12 μWh cm <sup>-2</sup> at 8.8 mW cm <sup>-2</sup>	85% (10 000 cycles)	[147]
	LiCl/PVA GPE//LiCl/PVA GPE	2.2	PVA/LiCl	152.1 mF cm <sup>-2</sup> at 1 mA cm <sup>-2</sup>	25.6 μWh cm <sup>-2</sup> at 275 μW cm <sup>-2</sup>	84% (20 000 cycles)	[162]
	NiCo-OH/ZnO-NR/CNT-yarn//NiCo-OH/ZnO-NR/CNT-yarn	1.2	PVA/LiOH	1065 mF cm <sup>-2</sup> at 5 mV s <sup>-1</sup>	1.38 μWh cm <sup>-2</sup> at 117 μW cm <sup>-2</sup>	60.5% (7000 cycles)	[155]
	Holey graphene/graphene fibers (HG@GFs)//holey graphene/graphene fibers (HG@GFs)	0.8	PVA/H <sub>2</sub> SO <sub>4</sub>	254.3 F cm <sup>-3</sup> at 0.1 A cm <sup>-3</sup>	5.7 mWh cm <sup>-3</sup> at 17 W cm <sup>-3</sup>	95.65% (10 000 cycles)	[139]
	PEDOT/MnO <sub>2</sub> /PEDOT//PEDOT/MnO <sub>2</sub> /PEDOT	0.8	PVA/Na <sub>2</sub> SO <sub>4</sub>	132.02 mF cm <sup>-2</sup> at 0.067 mA cm <sup>-1</sup>	7.51 μWh cm <sup>-2</sup> at 117 μW cm <sup>-2</sup>	83% (300 bending cycles)	[182]
	AC//NiO@MnCo-LDH	1.5	PVA/KOH	63.3 mF cm <sup>-2</sup> at 0.5 mA cm <sup>-2</sup>	0.0198 mWh cm <sup>-2</sup> at 0.38 mW cm <sup>-2</sup>	95.1% (7000 cycles)	[152]
	TFSC	CNF@PTPA//CNF@PTPA	1.4	PVA/H <sub>3</sub> PO <sub>4</sub>	398 mF cm <sup>-2</sup> at 0.28 mA cm <sup>-2</sup>	18.33 μWh cm <sup>-2</sup> at 0.99 mW cm <sup>-2</sup>	84.5% (10 000 cycles)
FeP NWAs/CNTE//MnO <sub>2</sub> NSs/CNTFs		1.8	PVA/LiCl	195 mF cm <sup>-2</sup> at 1 mA cm <sup>-2</sup>	23.4 mWh cm <sup>-3</sup> at 240 mW cm <sup>-3</sup>	86.5% (3000 cycles)	[183]
Self-twisted GFs (ST-GFs)//self-twisted GFs (ST-GFs)		1.0	PVA/H <sub>2</sub> SO <sub>4</sub>	973.1 mF cm <sup>-3</sup> at 10 mV s <sup>-1</sup>	25.5 mWh cm <sup>-3</sup> at 11.1 W cm <sup>-3</sup>	91% (10 000 cycles)	[174]
CoNi <sub>2</sub> S <sub>4</sub> @CFs//AC@CFs		1.0	PVA/KOH	632 F g <sup>-1</sup> at 20 mV s <sup>-1</sup>	NA	NA	[173]
WON NWs@CNT fiber//MnO <sub>x</sub> @CoNi@CNT fiber		1.8	PVA/LiCl	52 F cm <sup>-3</sup> at 0.5 A cm <sup>-3</sup>	23.4 mWh cm <sup>-3</sup> at 0.45 W cm <sup>-3</sup>	82.5% (10 000 cycles)	[172]
GF@PANI//GF@PANI		0.8	PVA/H <sub>2</sub> SO <sub>4</sub>	357.1 mF cm <sup>-2</sup> at 0.23 mW cm <sup>-2</sup>	5.7 mWh cm <sup>-3</sup> at 14.5 mW cm <sup>-3</sup>	96.2% (5000 cycles)	[180]
CFSC and RFSC	VN@CNF//Zn <sub>0.11</sub> CuO@MnO <sub>2</sub>	1.8	Na <sub>2</sub> SO <sub>4</sub> /PVA	296.6 mF cm <sup>-2</sup> at 1 mA cm <sup>-2</sup>	133.5 μWh cm <sup>-2</sup> at 0.9 mW cm <sup>2</sup>	76.57% (10 000 bending cycles)	[194]
	Graphene@PVDF nanofiber@graphene//graphene@PVDF nanofiber@graphene	0.8	PVA/H <sub>3</sub> PO <sub>4</sub>	346.5 mF cm <sup>-2</sup> at 0.6 mA cm <sup>-2</sup>	30.8 μWh cm <sup>-2</sup> at 0.24 mW cm <sup>-2</sup>	94% (10 000 cycles)	[195]
	CNT@Fe <sub>2</sub> O <sub>3</sub> //CNT@NiO@MnO <sub>x</sub>	1.8	PVA/LiCl	10.4 F cm <sup>-3</sup> at 30 mA cm <sup>-3</sup>	4.7 mWh cm <sup>-3</sup> at 27.1 mW cm <sup>-3</sup>	95% (2000 cycles)	[196]
	AC//MnNiCo-CH/CF	1.5	PVA/KOH	96.13 F g <sup>-1</sup> at 1 A g <sup>-1</sup>	30.04 Wh kg <sup>-1</sup> at 749.97 W kg <sup>-1</sup>	83.6% (8000 cycles)	[187]
	CNT/MnO <sub>2</sub> //CNT/MnO <sub>2</sub>	0.8	PVA/LiCl	91.6 F cm <sup>-3</sup> at 104.7 mA cm <sup>-3</sup>	8.14 mWh cm <sup>-3</sup> at 31.7 mW cm <sup>-3</sup>	95.3% (7000 cycles)	[140]
	MoO <sub>3</sub> //PANI	1.5	PVA/H <sub>2</sub> SO <sub>4</sub>	47.4 mF at 1 mA	67.51 μWh cm <sup>-3</sup>	40% (1000 cycles)	[189]

supercapacitors due to the low mass loading over lightweight, flexible, and miniature fibers. Therefore, the fabrication of 3D porous electrode materials with a high surface area and aspect ratio is a potential solution. Most of the FSCs are symmetrical, which manifests a shrunken potential window, and this issue can be handled by integrating supercapacitor-type and battery-type electrodes in a single FSC.

Moreover, most devices are fabricated using carbon-based yarns, concentrating on metallic fibers taken to the next step to solve the conductivity and mechanical viability issues. The implementation of PVA-based gel electrolytes in FSCs leads to higher resistance due to polymer matrix, which needs more attention. On that account, proper packaging of FSCs to protect them from human contact must be followed. Moreover,

uniform and calculated spacing between anode and cathode will protect the FSCs from short circuits. As future work, care should be taken to fabricate stretchable fibers with excellent electrochemical efficiency, high mechanical strength, and lightweight to meet the real time demand. Focusing on nontoxic and biocompatible materials is more suitable for wearable-based devices since the device in contact with the human body. The focus should be assessed to synthesize highly conductive gel electrolytes with a wide potential window and eco-friendliness. Device design, packaging, and scalability must be prioritized with correct evaluation of performance parameters following true standards.

## 5.2. Fiber-Shaped Batteries

With the rise of flexible electronics, especially wearables, the development of flexible batteries was placed under tremendous focus as the primary energy source in powering the other flexible electronics. Numerous flexible batteries were demonstrated previously, with their performance consistently improved in response to extensive development and investigation.<sup>[197]</sup> In this section, the three mainly adopted device configurations, namely, parallel, twisting, and coaxial configurations, are discussed and the pros and cons of these respective configurations are compared.

### 5.2.1. Configuration of Fiber-Shaped Batteries

As shown in **Figure 22a**, fibrous batteries could be further developed from rolling planar structured flexible batteries. However, such technique results in unsuitably larger diameter yarns for weaving, thus contradicting the requirement on weavability. Besides, rolling the planar structured flexible batteries subject the components to tensile and compression stress even before the exertion of external mechanical deformation.<sup>[191]</sup> As a result, poor mechanical integrity of the components could be anticipated, followed by severe capacity degradation when exposed to bending, twisting, or stretching. Therefore, reconfiguration of fibrous batteries is required to ensure standard electrochemical performance while ensuring its flexibility. The most widely adopted device configurations for fibrous batteries could be categorized into paralleling, twisting, and coaxial configurations as illustrated in **Figure 24b–d**, and their pros and cons are summarized in **Table 5**. Parallel configuration involves pairing of two fiber electrodes (cathode and anode) in parallel with a separator separating fibers as illustrated in **Figure 22b**. The anode and cathode fiber electrodes could be separately developed, and they were then aligned in parallel on a polymeric substrate for flexibility.<sup>[198]</sup> The planar polymeric substrate needs to be removed to achieve the fibrous dimensionality, which was demonstrated by Zhou et al. through wrapping parallel electrodes around a polymeric fiber substrate.<sup>[199,200]</sup> The main drawback in parallel configuration is the formation of electric field in the axial direction along the fiber where the effective area of the electrode is limited, significantly reducing the electrochemical performance of fibrous batteries (**Figure 22e**).

Twisting configuration can be obtained by twisting the parallel electrode pair through a rotation-translation setup as illustrated in **Figure 22c**. Given the increased complexity in fabricating twisting configuration and the difficulties in inserting a separator, precoating of solid-state electrolyte as a shell on each fiber electrodes is essential to mitigate short circuiting. Aside from complex manufacturing, the delicate twisting design is susceptible to detachment of electrodes from each other when exposed to frequent mechanical deformation (daily body movement). Such detachment could cause a significant rise in internal resistance, followed by severe electrochemical performance deterioration and low cycling stability. The friction between both electrodes during mechanical deformation could also wear out the gel polymer, causing short-circuit and performance degradation. Fu et al. demonstrated an attractive approach to mitigate the occurrence of short-circuit by wrapping a nonconducting plastic shell around one of the fiber electrodes as spacer.<sup>[201]</sup> Appropriate twisting stress also needs to be considered because increased twisting tightness pushes both electrodes too close to each other, leading to short circuit.<sup>[202]</sup> Otherwise, the distance between both electrodes increases at low twisting tightness, leading to high internal resistance and poor electrochemical performance. With the electrochemical performance of the twisted fibrous batteries heavily depending on the distance between both electrodes, eliminating any variation of distances from either pre- or postmechanical deformation could be crucial in ensuring stable cycling. Such variation in distance could be completely eliminated by developing coaxial configuration.

In coaxial configuration, the components were wrapped on a core fiber electrode, with a design identical to the sandwich structure of their planar structured counterpart, as illustrated in **Figure 22d**. Coaxial configuration could be fabricated through a layer-by-layer deposition of active materials for inner electrode, electrolyte (either aqueous or solid-state electrolyte), separator, and outer electrode layer. Conductive materials were usually adopted as inner core to ensure high performance-to-weight ratio and specific power and energy density of the coaxial fibrous battery, where the core acted as the supporting substrate for the coating of subsequent components and the current collector for the inner electrode. Some examples of materials for the core fiber are metal (such as lithium),<sup>[203]</sup> CPs,<sup>[204]</sup> MWCNT,<sup>[205]</sup> and metal-coated or doped carbon nanofiber.<sup>[206]</sup> One main concern with coaxial configuration is its limited coating thickness as an effort to control the overall diameter of the fibrous battery to be identical with the typical yarns/threads. However, low coating thickness, especially the active material components, is directly related to low energy density and it could be a major drawback in fabricating fibrous batteries for high energy consumption devices. The pros and cons of these configurations are summarized in **Table 5**.

### 5.2.2. Fiber-Shaped Electrodes

Several techniques were suggested to prepare electrodes, i.e., anode and cathode, mostly deposited on a fiber-like core material. For fibrous batteries, the electrode could be fabricated using a non-CP fiber, where two parallel aligned Au current

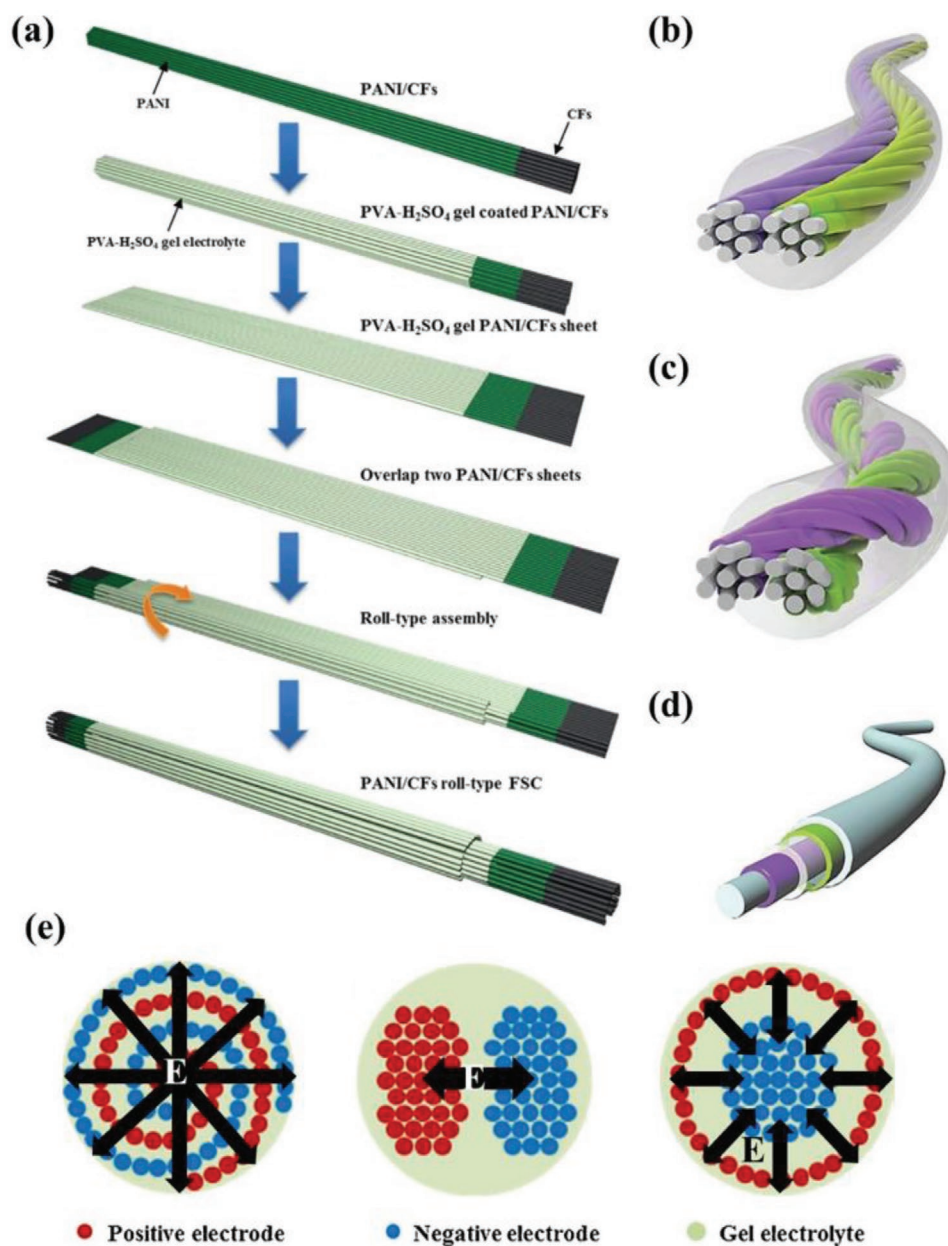


**Figure 22.** a) Schematic illustration showing the rolling of planar PANI/CFs/PVA-H<sub>2</sub>SO<sub>4</sub>/PANI/CFs into fibrous batteries. Reproduced with permission.<sup>[191]</sup> Copyright 2019, Elsevier. A schematic representation of b) paralleling, c) twisting, and d) coaxial configurations. Reproduced with permission.<sup>[3]</sup> Copyright 2020, John Wiley & Sons. e) The pattern of electric field formation across the electrodes for (from left to right) rolling, parallel or twisted, and coaxial configurations. Reproduced with permission.<sup>[191]</sup> Copyright 2019, Elsevier.

**Table 5.** Summary of structure parameters and pros and cons of various fibrous batteries. Adapted with permission.<sup>[207]</sup> Copyright 2020, John Wiley & Sons.

Design	Features	Advantages	Disadvantages	Refs.
Parallel	Parallel aligned electrode on flexible planar or fiber substrate	<ul style="list-style-type: none"> <li>Ease of large-scale production</li> <li>Short distance between electrodes</li> </ul>	<ul style="list-style-type: none"> <li>Bulky in size</li> <li>Less compatibility with other devices</li> </ul>	[200]
Twisting	Intertwisted fiber electrodes	<ul style="list-style-type: none"> <li>Miniature in size</li> <li>Good compatibility with other devices</li> </ul>	<ul style="list-style-type: none"> <li>Lack of long-term durability</li> <li>Less effective contact area</li> <li>Inconsistent distance between electrodes</li> </ul>	[202,208]
Coaxial	Fiber substrates with layer-by-layer coating	<ul style="list-style-type: none"> <li>Intimate contact and compact size</li> <li>Short distance between electrodes</li> <li>Structural stability</li> </ul>	<ul style="list-style-type: none"> <li>Limited coating thickness</li> <li>Complexity in preparation</li> </ul>	[209]

collectors are sputter coated, followed by deposition of active materials (in the paralleling configuration).<sup>[199]</sup> However, non-CP and metal (aluminum, copper, or nickel in their wired form) core substrates only solemnly transfer charges and they do not contribute to the gravimetry specific capacity, leading to decreased specific energy and power density. Therefore, considering conductive materials with intrinsic electrochemical performance as the current collector and electrode is crucial for achieving high specific energy and power density. CPs and CNT, which functioned simultaneously as the active materials and the current collector, were widely accepted as the electrode candidates for fibrous batteries. A summary of the electrochemical performance of electrode materials used in fibrous batteries is provided in **Table 6**.

Polymeric fibers, either intrinsically conductive or embedded with conducting substances such as graphene, were regarded as a suitable candidate for the current collector in fibrous batteries compared with metal wire analogues in term of cost, performance-to-weight ratio, and mechanical flexibility.<sup>[210–212]</sup> However, the low electrical conductivity of polymeric fibers could hamper the electrochemical performance of the fibrous batteries, prompting a switch of focus toward conducting CNTs. In fact, the high electrical conductivity and mechanical strength make CNT one of the most suitable materials as the current collector for fibrous batteries.<sup>[213,214]</sup> A free-standing MWCNT anode was previously investigated for prismatic lithium-ion battery; it showed a significantly higher discharge capacity of 960 mAh g<sup>-1</sup> (at a discharging current of 200 mA g<sup>-1</sup>) compared

with that in commonly used graphite (372 mAh g<sup>-1</sup>).<sup>[214]</sup> The electrochemical performance of the MWCNT was further enhanced by incorporating active materials, such as MWCNT/Si core-shell design, as demonstrated by Lin et al.<sup>[215]</sup> The results offered an improved discharge capacity of 1670 mAh g<sup>-1</sup>. Zhang et al. further reduced the particle size of silicon and deployed inactive Cu<sub>3</sub>Si as adhesive between the Si and MWCNT, further enhancing the discharge capacity of MWCNT/Si to 2533 mAh g<sup>-1</sup> with a significant improvement in cycling stability.<sup>[216]</sup> Different from these studies that utilized lithium wire as the counter-electrode, Ren et al. deployed metal oxide/MWCNT composite as cathode (MWCNT/LiMn<sub>2</sub>O<sub>4</sub>) and anode (MWCNT/Li<sub>4</sub>Ti<sub>5</sub>O<sub>12</sub>) and revealed an energy density of 27 Wh kg<sup>-1</sup> (an order of magnitude higher than its planar structured counterpart) and 97% performance retention after 1000 cycles of bending. CNT can be undoubtedly regarded as the most promising electrode and current collector material for fibrous batteries. However, the hydrophobicity of CNT needs to be considered when selecting suitable electrolyte to avoid poor electrochemical performance due to the incompatibility between the electrolyte and electrode.

### 5.2.3. Solid-State Electrolytes

The electrolyte used in current batteries could be separated into aqueous and nonaqueous electrolyte, where the former is water-based and the latter includes ionic liquid and aprotic

**Table 6.** Electrochemical performance summary of some fibrous batteries. Adapted with permission.<sup>[3]</sup> Copyright 2020, John Wiley & Sons.

Design	Cathode (anode)	V <sub>oc</sub> [V]	Energy density	Specific capacity	Capacity retention/cycles/ current density	Refs.	
Parallel	MWCNT/Si (lithium wire)	0.02–1.2	N/A	1168 mAh g <sup>-1</sup> at 2.0 A g <sup>-1</sup>	58%/50/0.6C	[215]	
	CNT/LiMn <sub>2</sub> O <sub>4</sub> (CNT/Li <sub>4</sub> Ti <sub>5</sub> O <sub>12</sub> )	1.5–3.3	27 Wh kg <sup>-1</sup> 17.7 mWh cm <sup>-3</sup>	138 mAh g <sup>-1</sup> at 0.01 mA	85%/100/0.05 mA	[217]	
	CNT/MoS <sub>2</sub> (lithium wire)	0.01–3.0	N/A	1084 mAh g <sup>-1</sup> at 0.5 A g <sup>-1</sup>	>1250 mAh g <sup>-1</sup> /100/0.2 A g <sup>-1</sup>	[218]	
	Titania/rGO (lithium wire)	1.0–3.0	N/A	126 mAh g <sup>-1</sup> at 0.0170 mA	70%/200/0.0085 mA	[219]	
	LiMn <sub>2</sub> O <sub>4</sub> /CNT (PI/CNT)	0–1.2	48.93 Wh kg <sup>-1</sup> 14.30 mWh cm <sup>-3</sup>	86 mAh g <sup>-1</sup> at 600C	90%/200/10C	[220]	
	CNT/Na <sub>0.44</sub> MnO <sub>2</sub> (NaTi <sub>2</sub> (PO <sub>4</sub> ) <sub>3</sub> @C)	0–1.6	25.7 mWh cm <sup>-3</sup>	46 mAh g <sup>-1</sup> at 0.1 A g <sup>-1</sup>	76%/100/0.2 A g <sup>-1</sup>	[221]	
	CNT@MnO <sub>2</sub> (CNT@Zn)	0.8–1.85	53.8 mWh cm <sup>-3</sup>	302.1 mAh g <sup>-1</sup> at 60 mA g <sup>-1</sup>	98.5%/500/2 A g <sup>-1</sup>	[10]	
Twisted	NCHO@yarn (Zn@yarn)	1.2–2.0	8 mWh cm <sup>-3</sup>	16.6 mAh cm <sup>-3</sup> at 31 mA cm <sup>-3</sup>	60%/1000/31 mA cm <sup>-3</sup>	[222]	
	Mn–NiO <sub>x</sub> (Zn@Li–RTiO <sub>2</sub> )	1.0–2.0	34 mWh cm <sup>-3</sup>	19.6 mAh cm <sup>-3</sup> at 1.4 A cm <sup>-3</sup>	95%/2000/11.2 A cm <sup>-3</sup>	[211]	
	Ni–NiO fiber (Zn fiber)	1.5–2.0	0.67 mWh cm <sup>-3</sup>	116.1 μAh cm <sup>-3</sup> at 3.7 A g <sup>-1</sup>	99.6%/10 000/22.2 A g <sup>-1</sup>	[212]	
	RuO <sub>2</sub> /N-CNTs (lithium wire)	2.0–4.6	N/A	1981 mAh g <sup>-1</sup> at 320 mA g <sup>-1</sup>	100 cycles (>600 h)	[223]	
	Mn–NiO (Mn–Fe <sub>2</sub> O <sub>3</sub> )	0.4–2.0	61.0 mWh cm <sup>-3</sup>	46.0 mAh cm <sup>-3</sup> at 2.5 A cm <sup>-3</sup>	91.2%/30 000/20 A cm <sup>-3</sup>	[224]	
	CoP@Ni(OH) <sub>2</sub> (S–α-Fe <sub>2</sub> O <sub>3</sub> )	0–1.6	81.0 mWh cm <sup>-3</sup>	0.203 mAh cm <sup>-3</sup> at 3 mA cm <sup>-2</sup>	85.3%/3000/30 mA cm <sup>-2</sup>	[225]	
	NiZnCoP/CNTF (Fe <sub>2</sub> O <sub>3</sub> /OCNTF)	0–1.6	30.61 mWh cm <sup>-3</sup>	0.092 mAh cm <sup>-2</sup> at 1 mA cm <sup>-2</sup>	88.6%/3000/2 mA cm <sup>-2</sup>	[226]	
	Coaxial	CNT/LiMn <sub>2</sub> O <sub>4</sub> (CNT–Si/CNT)	2.0–4.3	242 mWh g <sup>-1</sup> 99.3 mWh cm <sup>-3</sup>	106.5 mAh g <sup>-1</sup>	87%/100/148 mAh g <sup>-1</sup>	[227]
		rGO/sulfur/SSF (lithium wire)	1.8–2.8	N/A	335 mAh g <sup>-1</sup> at 167.5 mA g <sup>-1</sup>	56%/90/0.1C	[228]
		LiCo <sub>2</sub> –CMF (Li <sub>4</sub> Ti <sub>5</sub> O <sub>12</sub> –CMF)	1.5–2.8	215 mWh cm <sup>-3</sup>	131 mAh g <sup>-1</sup> at 1C	N/A	[229]
LiFePO <sub>4</sub> –CF (Li <sub>4</sub> Ti <sub>5</sub> O <sub>12</sub> )		1.0–2.5	6 mWh cm <sup>-3</sup>	3.1 μAh cm <sup>-3</sup> ar 26 μA cm <sup>-2</sup>	85%/100/26 μA cm <sup>-2</sup>	[230]	
	Aligned CNT (Li <sub>x</sub> Si/CNT)	2.1–4.0	512 Wh kg <sup>-1</sup>	500 mAh g <sup>-1</sup> at 0.1 mA	500 mAh g <sup>-1</sup> /100/0.1 mA	[231]	

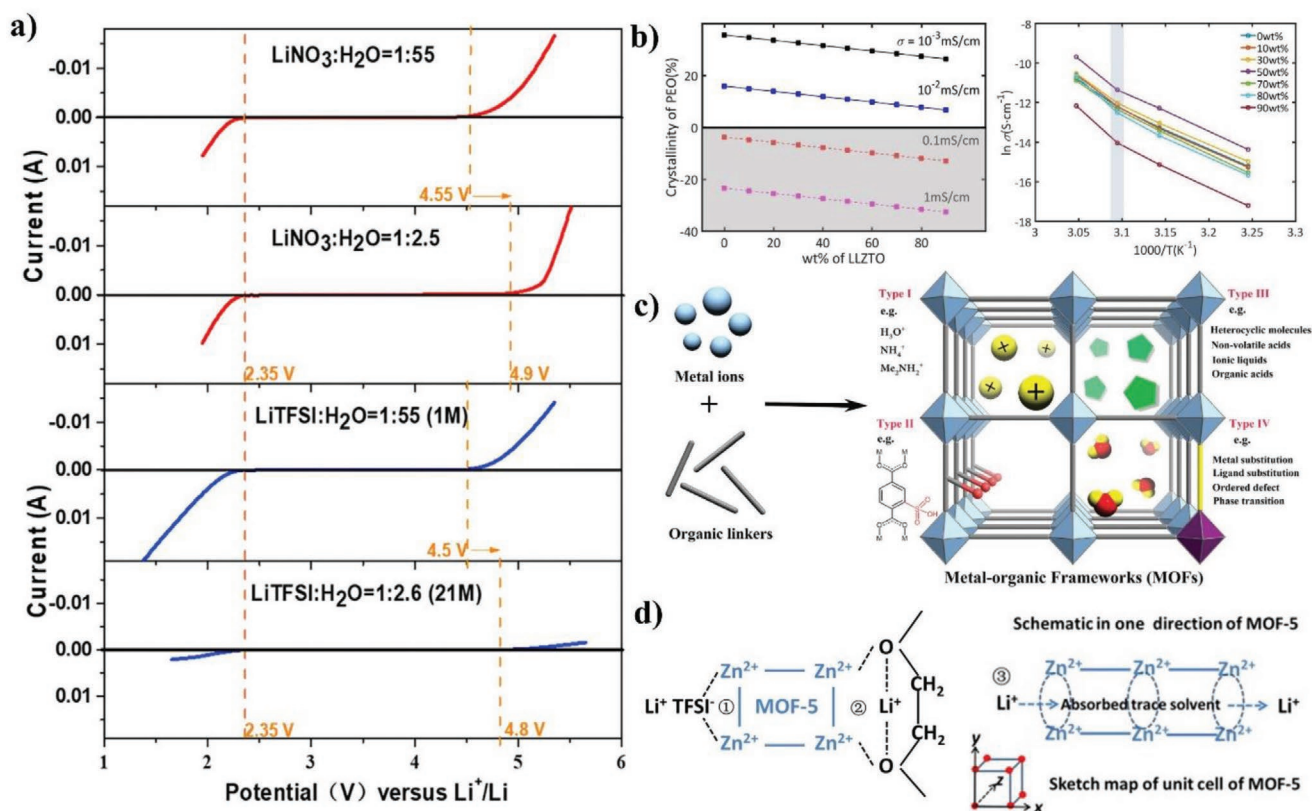


**Figure 23.** a) Comparison of differences in the potential window of aqueous electrolyte with different concentrations of  $\text{LiNO}_3$  and  $\text{LiTFSI}$ , showing an enhancement in electrochemical stability window when the presence of water molecules was reduced. Reproduced with permission.<sup>[232]</sup> Copyright 2018, Elsevier. b) Effect of crystallinity of polyethylene oxide polymer on the ionic conductivity of the lithium ions. Reproduced with permission.<sup>[237]</sup> Copyright 2020, Elsevier. c) The diffusion of ions through the space within the metal-organic framework. Reproduced with permission.<sup>[238]</sup> Copyright 2020, Wiley. d) Illustration of the anchoring of anion within the metal-organic framework due to the interaction with the metal ions, leading to higher lithium-ion transference number. Reproduced with permission.<sup>[239]</sup> Copyright 2013, Elsevier.

electrolytes. One major drawback with aqueous electrolytes is the low electrochemical stability window, where the electrolysis of  $\text{H}_2\text{O}$  took place at 1.23 V, leading to severe deterioration in the electrochemical performance of rechargeable batteries when charged to voltage higher than 1.23 V.<sup>[232]</sup> Through theoretical analysis, Zheng et al. demonstrated that the electrochemical stability window could be improved by reducing the water content in the aqueous electrolyte (Figure 23a).<sup>[232]</sup> A recently successful approach to mitigate this drawback has been introduced by adopting water-in-salt tactic, where ionic salts are dissolved in water to or higher than their solubility limit.<sup>[233,234]</sup> Through this approach, all the water molecules were involved in solvating the ionic ions and eliminated “free” water molecules, leading to significant increase in electrochemical stability window to 3 V (compared to 1.23 V in salt-in-water counterparts).<sup>[234]</sup> Meanwhile, nonaqueous electrolytes have been the electrolyte of choice in commercialized lithium-ion batteries owing to their superior ionic conductivity ( $10^1$ – $10^{-1}$  S  $\text{cm}^{-1}$ ) and high electrochemical stability window for high-voltage rechargeable batteries.<sup>[235]</sup> These electrolytes included a mixture of methyl ethyl carbonate, ethylene carbonate, dimethyl carbonate, and diethyl carbonate, with lithium containing salt ( $\text{LiPF}_6$ ,  $\text{LiTFSI}$ ,  $\text{LiCl}$ ,  $\text{LiClO}_4$ ,  $\text{LiBF}_4$ , etc.).<sup>[236]</sup> The usage of aqueous and nonaqueous electrolytes required proper sealing

owing to the hygroscopic nature and reactivity of lithium ions with ambient atmosphere as they are flammable and explosive in nature. Even though fibrous rechargeable batteries could be encapsulated, worn-out encapsulation due to frequent mechanical deformation could result in electrolyte leakage, a phenomenon not acceptable in wearable electronics.

In this aspect, solid-state electrolyte is much preferred over aqueous electrolyte because of 1) no leakage when encapsulation is worn out; 2) ease in fabrication, where electrolyte could be coated onto the active materials instead of injection at the end of fabrication; and 3) the separator that could be completely removed. Some most commonly deployed solid-state electrolytes could be categorized into gel-polymer electrolyte,<sup>[240]</sup> MOF,<sup>[241]</sup> and ionic conducting ceramic.<sup>[242]</sup> With the removal of aqueous water molecules, the electrochemical stability window of the solid-state electrolyte was significantly improved, allowing the development of 5 V batteries without severe electrolyte decomposition.<sup>[243]</sup> The elimination of organic liquids also eradicates the flammability concerns and greatly improves the safety of batteries.<sup>[244]</sup> Even though solid-state electrolytes offer high electrochemical stability window, they suffer from poor mechanical stability (as in the case of ionic conducting ceramic) and low ionic conductivity (as in the case of gel-polymer electrolyte). Efforts were taken to incorporate ionic

conducting ceramic and gel-polymer electrolytes by forming a composite polymeric electrolyte with high ionic conductivity while preserving the mechanical flexibility. For example, Liu et al. demonstrated an improvement in the ionic conductivity of PAN-LiClO<sub>4</sub> gel-polymer electrolyte ( $2.1 \times 10^{-7}$  S cm<sup>-1</sup>) to  $2.4 \times 10^{-4}$  S cm<sup>-1</sup> by incorporating 15 wt% Li<sub>0.33</sub>La<sub>0.557</sub>TiO<sub>3</sub> as filler.<sup>[245]</sup> Zhao et al. adopted a similar approach by incorporating 0.3% graphene oxide into the gel-polymer electrolyte (mixture of LiTFSI, EMITFSI, PVDF-HFP, and dimethylformamide) to achieve a lithium-ion transference number of as high as 0.79, approaching unity, which is favorable for high electrochemical performance.<sup>[246]</sup> The incorporation of filler was reported to disrupt the crystallinity of polymer molecules, thus allowing enhanced ion conductivity (Figure 23b). A similar effect could also be observed through the incorporation of plasticizer.<sup>[247]</sup>

Other than gel-polymer electrolytes, MOFs offer superior electrochemical performance as the electrolyte. Due to the strong interaction with central metal ions, the anions of ionic salt (such as TFSI<sup>-</sup>, ClO<sub>4</sub><sup>-</sup>, BF<sub>4</sub><sup>-</sup>, and PF<sub>6</sub><sup>-</sup>) were anchored and immobilized, leading to high lithium-ion mobility (Figure 23c,d).<sup>[248]</sup>

However, MOFs were investigated to mainly mitigate dendrite growth at the lithium metal anode. Thus far, the application of metal-oxide framework as the electrolyte in flexible planar or fiber batteries is lacking. Overall, the poor intrinsic ionic conductivity could be regarded as the main obstacle for the widespread adoption of solid-state electrolytes. Even after numerous efforts to enhance the ionic conductivity of gel-polymer electrolytes, their ionic conductivity is still far from satisfactory compared with that of metal-oxide analogues (in the range of  $10^{-1}$ – $10^{-5}$  S cm<sup>-1</sup>). The capability to deposit a thin-layer metal-oxide electrolyte, either through vapor deposition or sputtering, could offer high electrochemical performance while retaining mechanical flexibility.

Deploying active materials with high gravimetry or volumetric specific capacity, such as alloying type anode and conversion type cathode, could be a suitable approach to increase energy density. By using sulfur as the electrode (with a gravimetry specific capacity of  $\approx 1600$  mAh g<sup>-1</sup>), Fang et al. demonstrated a lithium-sulfur fibrous battery with an energy density of  $\approx 1500$  Wh kg<sup>-1</sup>.<sup>[249]</sup> The next major development for fibrous batteries could be based on high gravimetry capacity materials as cathode and anode. Besides, encapsulating fibrous batteries is another area that is lacking research. In most cases, the gel-polymer electrolyte completely covers the electrodes, thus serving as an encapsulate. However, gel-polymers are not rigid and they could be displaced under pressure, leading to a high likelihood of short circuiting. Suitable encapsulates for fibrous batteries could be developed on the basis of technology advancement achieved in planar structured flexible batteries,<sup>[250]</sup> with few extra considerations as follows: the encapsulate needs to 1) withstand extensive friction during frequent body movement, 2) possess normal yarn features for enhanced wearing experience, and 3) be mechanically strong from being torn or worn out, even at small thickness, to preserve the overall diameter of fibrous batteries. Finally, planar structured counterparts could be developed on a 2D polymer substrate using the available production line of rechargeable batteries. However, the fibrous batteries based on a 1D wired polymeric or conductive substrate

is incompatible with the current battery production line. Thus, a new facilities/production line capable of fabricating fibrous batteries on a large scale need to be constructed.

In summary, with the advancement of technologies moving toward Internet-of-Things applications where portability matters the most, fiber-shaped or wearable batteries would play a major role as the energy source for future electronics. Undoubtedly, the configuration of the fiber-shaped batteries is a vital aspect to be look into, where both parallel and twisted configurations can be easily manufactured compared to coaxial configuration. However, bending and twisting the fiber-shaped batteries could alter the distance between the cathode and anode, causing poor performance as well as short-circuiting if both electrodes are too close to each other. Besides, the effective surface area of the electrode in these two configurations is very low, leading to low energy density. Even though coaxial configuration could overcome all these drawbacks, the mechanical properties (Young's modulus) of each component need to be tailored such that no one components will failed while bending. In the case where lithium wire is utilized in the coaxial configurations, the polymeric electrolyte remains functional while the core could sustain from mechanical fatigue, rendering the fiber-shaped battery functionless. Other than the design configuration of the fiber-shaped batteries, its tap density is yet another puzzle to be solved. Fiber-shaped batteries utilized numerous supportive materials that are electrochemically inactive to preserve their functionalities, such as polymer additives to ensure the flexibility of the electrode, etc., which severely deteriorate the specific volumetric capacity and energy density of the batteries. The volume changes of the electrode during both charging and discharging need to be critically studied due to the fact that the components could be detached from each other, increasing the shunt resistance and deteriorating the electrochemical performance of the batteries. Undoubtedly, fiber-shaped batteries is still in its early stage of development and promising advancement can be envisaged. More efforts are needed to advance fiber-shaped batteries to its new height, especially in discovering suitable materials for each component.

## 6. Other Fiber-Shaped Functional Devices

In addition to energy harvesting and storage devices, fiber-shaped architectures are also common for a range of functional devices. In this section, we highlight some key results from various fiber-based functional systems such as sensors (Section 6.1), LEDs (Section 6.2), and chromatic devices (Section 6.3). These functional devices are an important part of fiber-based integrated system for a self-standing complex electronic device (see Section 7).

### 6.1. Fiber-Shaped Sensors

Sensing devices based on fiber-shaped technology have been widely investigated for medical applications, due to their ability to effectively monitor health conditions via physiological signal sensing. Smart systems with the ability to sense multiple inputs while retaining their flexibility, stretchability, portability,

and wearability have been successfully demonstrated. The progress of the last decade has led to the fabrication of commercial devices for real-time monitoring. Next-generation technologies are also being built from textiles, incorporating sensors that harness movement and heat to generate power and become self-powered, while having high electrical conductivity and mechanical robustness. Physical and chemical sensors are the main types of fiber-shaped sensing devices, which are based on electrical signal detection.<sup>[251]</sup>

### 6.1.1. Conductive-Fiber Physical Sensors

These fiber-shaped sensing devices consist of conductive materials used for their sensing abilities, not only on fibers but also on fabrics too. Their conductivity must be changed from an environmental or mechanical stimulant to obtain an electrical signal from them. Various materials have been used for conductive-fiber sensors, including CPs, carbon materials, nanowires, and liquid metals.<sup>[252]</sup> They could be used as sensors for measuring temperature, because they could showcase a linear change in resistivity under temperature change. By using PEDOT:PSS as a dye, Lee et al. developed a temperature-sensing

device that exhibited negative temperature coefficient characteristics with the resistance linearly decreasing with the increase in temperature. The linearity was 99.8% for temperature ranging from  $-50$  up to  $80$  °C.<sup>[253]</sup> In addition, rGO fibers that contained metallic Cu and semiconducting CuI particles were used by Yeo et al. to fabricate sensors that could be chemically sensitive and temperature insensitive or the opposite by controlling the Cu concentration in the fibers.<sup>[254]</sup> Wu et al. also presented a method for designing and fabricating flexible multimode electronic textiles on the basis of functionalized silkworm fiber coiled yarns (Figure 24a–c). A combination of CNTs and an ionic liquid was used, which resulted in a sensitivity of  $1.23\% \text{ } ^\circ\text{C}^{-1}$  and very good stability (Figure 24d). The change in capacitance of each cross-point of two yarns results in a sensitivity sensing of  $0.136 \text{ kPa}^{-1}$ . This combo textile sensor could sense temperature and pressure independently with a position precision of  $1 \text{ mm}^2$ .<sup>[255]</sup> Moreover, Lee et al. demonstrated an intrinsic strain-insensitive fiber-type temperature sensor with compressed microwrinkles. The sensor exhibited a sensitivity of  $0.93\% \text{ } ^\circ\text{C}^{-1}$  and a strain insensitivity up to 60% tensile strain. When the sensor was knitted into the fabric, a negligible change in resistance was observed with up to 180% strain. The temperature responsive device was fabricated on a fiber

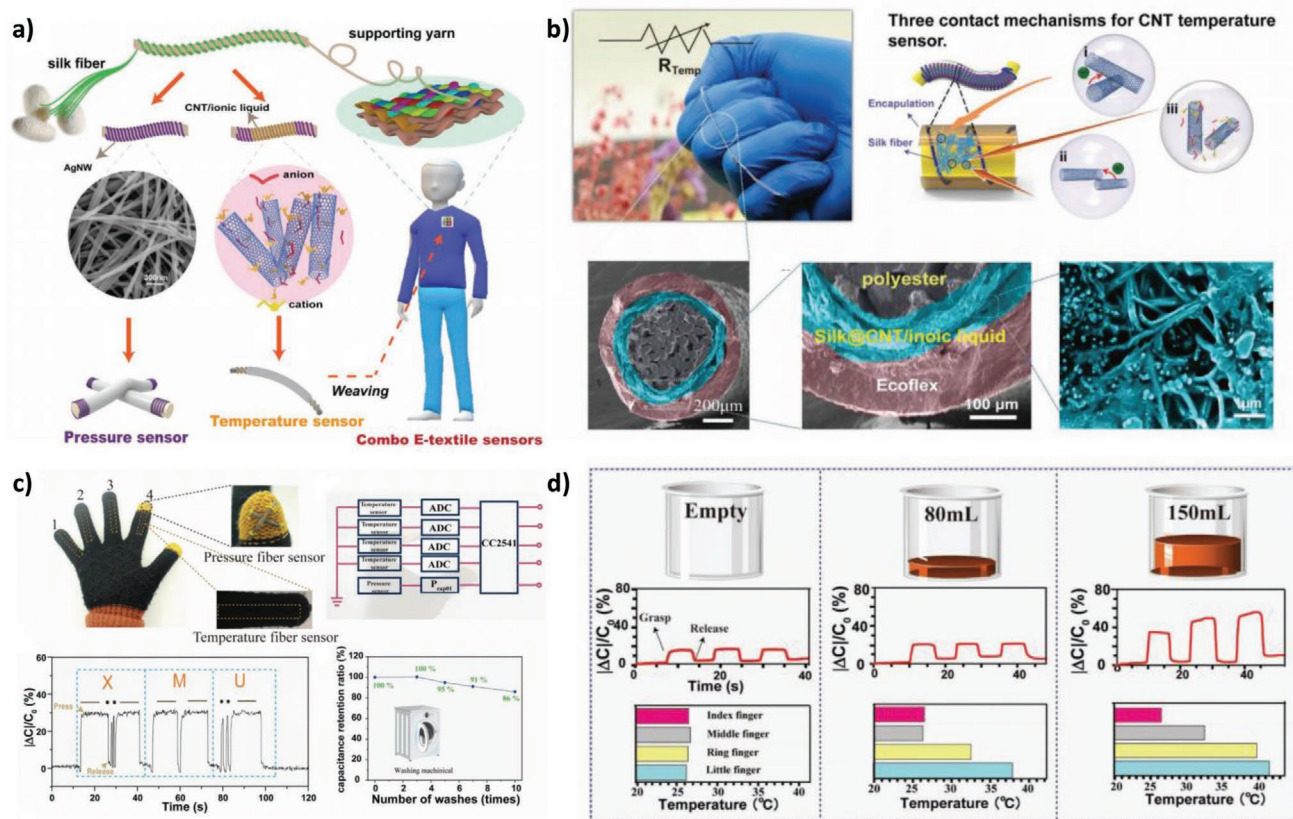


**Figure 24.** a) Schematic of the strategy of fabrication of silk fiber-wrapped combo temperature–pressure sensors: Coiling supporting yarns by silkworm silk fibers; coating the silk fibers coiled yarns with temperature or pressure sensing materials; coating the protection or dielectric layers on the functional yarns/fibrous sensors; and weaving the fibrous sensors into a combo two-layer multimode sensors textile. b) Composite temperature sensors and conductive mechanisms using different sensing materials. c) Schematic illustration and multimode sensing performance of the smart gloves having fibrous pressure and temperature sensors embedded. d) Schematic diagram of the beaker with different capacities and corresponding electrical signal variations for pressure sensor and temperature distribution. Reproduced with permission.<sup>[255]</sup> Copyright 2019, John Wiley & Sons.

surface via dip-coating, after a prestrain, followed by lamination of an elastic protective layer and it was integrated into a smart glove with a wireless transmitter to track continuous changes of the temperature without deformations.<sup>[256]</sup> A highly flexible and durable fiber-shaped temperature sensor was also developed by Hilal and Han, who fabricated a G/Ni-based temperature device (D-1) with a positive temperature coefficient of resistance of 0.0108 ( $^{\circ}\text{C}^{-1}$ ), a high repeatability and a linear response to temperature changes. The device also retained 75% of its characteristics after 10 000 bending cycles of an 11.42 mm radius, while maintaining its resistance for a 40–90% humidity level. When exposed to various gases for 20 min, the resistance remained unchanged.<sup>[257]</sup>

Carbon-based fibers could be also used as humidity sensors as their electrical resistivity undergoes significant changes upon the chemisorption of water molecules when exposed to different relative humidity measures. Liang et al. developed a single fiber self-powered generator unit, which was less than 1 mm long with a diameter of 80  $\mu\text{m}$  and could provide 355 mV in response to the variations in humidity, for use as a self-powered humidity sensor.<sup>[258]</sup> Another application for conductive-fiber physical sensors is the monitoring of bioelectrical signals, such as electromyograms.<sup>[259]</sup> The first electrocardiogram sensors were based on wet Ag/AgCl electrodes in direct contact with the skin through the use of an electrolyte gel. However, because this geometry was inconvenient and it led to allergies, dry electrodes were later developed to be used without the need of an electrolyte gel. Yokus and Jur fabricated dry electrodes via screen printing of conductive inks and the output showed results comparable to those of wet electrodes.<sup>[260]</sup>

One of the most studied type of conductive-fiber sensors are the strain sensors. They are used for tracking vital signs such as blood pressure, oxygen saturation and heart rate, or even movement with very high accuracy.<sup>[261]</sup> One of the first strain-sensing fabrics were developed by Scilingo et al.<sup>[262]</sup> who coated fabrics with conductive polymer polypyrrole (PPv), which exhibited piezoresistive and thermoresistive properties, in order to detect human body gestures. Yang et al. used CNTs as a coating on fabric, to improve its mechanical properties leading to fast response and great stability. The sensors were used to track real-time human motions, while exhibiting a strong electric heating effect.<sup>[263]</sup> Machine washable and scalable sensors with materials applicable in the textile industry were fabricated by Zhao et al.,<sup>[264]</sup> through loom weaving of Cu–PET and PI–Cu–PET yarns, generating triboelectric charges for self-powered human respiratory sensing. The triboelectric effect was also utilized by Ning et al., who developed flexible and stretchable coaxial F-TENGs with 0.63 mm diameter, by depositing conductive Ag NWs/CNTs and encapsulated PDMS on the fiber to convert mechanical stimuli to electric signaling.<sup>[127]</sup>

In an attempt to improve the stability of these devices, Li et al. fabricated textile-based stretchable sensors with the use of Ag nanocrystals that showcased good sensitivity, rapid response, and excellent durability.<sup>[265]</sup> A polyamide monofilament yarn that was dip coated with GO and reduced via a green chemical reduction method was produced by Tas et al.<sup>[266]</sup> The seven-layer graphene-coated polyamide monofilament yarn had a low sheet resistance at 3.09  $\text{k}\Omega \text{sq}^{-1}$  and the 90° and 180° bent yarns had 3.57 and 3.81  $\text{k}\Omega \text{sq}^{-1}$  sheet resistance, respectively,

making them a promising candidate for their use in sensing devices. Chen et al. demonstrated a Ni/active material-coated flexible electrode with different dimensionalities, namely, 1D fiber-shaped, 2D plane, and 3D spatial, as various tensile and compressive strain sensors, for monitoring human health and movement. They concluded that any kind of absorbent fiber material could be coated with Ni/CNT via “dipping-electroless plating” method, thus making those compressible or stretchable substrates demonstrate very good conductivity and good electromechanical properties to be used as wearable smart textiles with electrical functionalities.<sup>[267]</sup>

Highly stretchable MWCNT-decorated TPU fibers with a porous microstructure were developed by Yu et al. through a scalable strategy by wet-spinning and ultrasonication. The use of MWCNTs on the TPU fiber provided great sensing capabilities with a high gauge factor and a large workable sensing range at 300% strain, a very good durability of 10 000 cycles, a light weight of 0.85  $\text{g cm}^{-3}$ , and a fast response of 200 ms, while being insensitive to torsion, temperature, and humidity changes.<sup>[268]</sup> A fibrous strain sensor for detecting various human movements was recently developed via coaxial wet-spun approach by Yue et al. It exhibited a stretchable black/thermoplastic PU with porous and core–sheath structure. It also obtained an ultrahigh sensitivity with a maximum gauge factor of 20084, a fast response time of 200 ms, a large strain range of more than 200% and a good durability of more than 11 000 cycles.<sup>[269]</sup>

One of the main challenges faced by flexible strain sensors is the development of a multifunctional sensor with simultaneous ultralow detection limit, a broad sensing range, and a high reproducibility. Moreover, most sensors rely on external power supply, which limits their practical application. Therefore, an increasing need to design and develop self-powered fiber-shaped stretchable sensors is present, something that remains very challenging. Lu et al. reported a CNT/flexible fiber-shaped strain sensor with a highly elastic rubber fiber core tightly wounded by a spring-like polypropylene fiber as shell. The sensor achieved a combination of ultralow detection limit of 0.01%, a sensing range of 200%, and a repeatability of 20 000 cycles, while its response time was less than 70 ms for stretching and releasing.<sup>[270]</sup> A multifunctional coaxial energy fiber for energy harvesting, storage, and sensing was recently reported by Han et al., who developed an energy fiber consisting of as F-TENG, as SC and a pressure sensor in a coaxial geometry. It displayed a  $\approx 96.6\%$  retention of cyclic stability, a maximum power of 2.5  $\mu\text{W}$ , and a sensitivity of 1.003  $\text{V kPa}^{-1}$ .<sup>[271]</sup> An integrated multifunctional sensor was also prepared by Pan et al., who created an all-in-one stretchable coaxial-fiber sensor that simultaneously detects strain and stores energy via an SC. It was fabricated on an elastic fiber with a maximum voltage of 1.8 V by using manganese dioxide and PPv as positive and negative electrodes, respectively, on aligned CNT sheets. It delivered an energy density of 1.42  $\text{mWh cm}^{-3}$ , very good flexibility, 85.1% capacitance retention after stretching for 6000 cycles at a strain of 200%, and great durability at repeated unloading/loading of 40% strain for 10 000 cycles on one single charge.<sup>[272]</sup> Zhao et al. recently reported an all-in-one coaxial fiber-shaped asymmetric SC device, fabricated by a multi-ink 3D printing technology, where they designed the

internal structure of the coaxial needles and controlled the rheology and feed rate of the multi-ink; the device could be integrated with a mechanical unit and pressure sensor.<sup>[273]</sup> Printing was also used by Tang et al. who developed a low-cost coaxial printing technique to fabricate stretchable and flexible fibers for wearable strain sensors. The dimensions of the printed fibers could be controlled with the change in pressure of the used inks. The fabricated CNT-based sensors exhibited good sensitivity, a stretchability of 150% and waterproof performance, while being able to detect a 0.1% change in strain and having a high durability of over 15 000 cycles.<sup>[274]</sup>

For wearable sensors, having real-time feedback is important to help track and display the measured signals. Expressing force directly by themselves is a significant advantage for wearable sensors. Therefore, integrating visualized feedback with sensors is highly desirable and photonic and fluorescence signals are one of the most intuitive and effective methods to deliver those signals. Zhou et al.<sup>[275]</sup> recently developed a fiber-shaped light-emitting pressure sensor that visualizes and simultaneously detects a force stimulus. It was made using a sheath composed of a micropatterned polymer composite hollow fiber and a fiber electrode core. The electroluminescent phosphors present in the sheath, served as pressure-sensing and light-emitting layers. It showed a high capacitive sensitivity of 16.81 N<sup>-1</sup> and real-time electroluminescence intensity changes. This fiber-shaped sensor was also flexible and robust and was woven into a smart textile worn on human skin to track human activities. Finally, Zhang et al. recently integrated a high-performance UV photodetector with the heterostructure: AZO/ZnO NRs/polyvinylcarbazole/PEDOT:PSS on human hair. They obtained a flexible UV-image sensor with a fast response time, high photoresponsivity, and excellent flexibility; it consisted of seven display pixels that could produce accurate images of numbers from 0 to 9.<sup>[276]</sup>

### 6.1.2. Conductive-Fiber Chemical Sensors

Another important aspect of health monitoring is the tracking of chemical and biological parameters, such as metabolites, electrolytes, and various biomarkers. Conductive-fiber chemical sensors have been developed to monitor health at a molecular level. A chemical sensor has two units, a receptor that transforms the concentration of an analyte into a chemical output signal, and a transducer that converts the generated signal to a readable value.<sup>[277]</sup> Wang et al. reported a strategy to obtain highly flexible electrochemical fabrics from sensing fiber units, for detecting various physiological signals such as glucose, Na<sup>+</sup>, K<sup>+</sup>, Ca<sup>2+</sup>, and pH, with maintained structural integrity and detection ability.<sup>[14]</sup> A fast one-step process for producing PEDOT:PSS fibers without the insulating PSS component was developed by Zhang et al. They tested these fibers in various environments such as boiling water and sonication, and showed that the fibers could withstand mechanical stressing, thereby making them a good candidate for sensitive touch sensors and body moisture tracking.<sup>[278]</sup> Zhao et al. also demonstrated an elastic Au fiber-based three-electrode electrochemical device for wearable textile glucose biosensing, where a functionalized Prussian blue and glucose oxidase Au fiber was used

as the working electrode and a unmodified Au fiber was used as the counter-electrode. The textile glucose sensors demonstrated a linear range of  $0 \times 10^{-6}$  to  $500 \times 10^{-6}$  M and a sensitivity of 11.7  $\mu\text{A mm}^{-1} \text{cm}^{-2}$ .<sup>[279]</sup>

Fiber-shaped In<sub>2</sub>O<sub>3</sub> crystalline nanofibers were achieved by Wang et al.<sup>[280]</sup> via electrospun and calcination route. They exposed the nanofibers to acetic acid vapors with concentrations ranging from 500 ppb to 2000 ppm at a temperature of 250 °C and obtained an ultrahigh response of 66.7 at 2000 ppm, a low response of 25 s and a recovery time of 37 s at 100 ppm. The sensor showcased a low detection limit and it could reach 500 ppb, making it a good candidate for acetic acid detection. Wang et al. proposed a method to construct a potentiometric ion sensor on a surface strain redistributed elastic fiber with high stretchability and good sensing stability to design highly stretchable and stable biochemical sensors that could be used in textiles for wearable monitoring. In this method, the sensing materials on a unilateral bead region were unchanged during 0–200% stretching, thus being able to perform stable functions while ignoring the stretching of the fiber.<sup>[281]</sup>

Yang et al. reported the development of organic electrochemical transistors (OECTs)<sup>[282]</sup> on nylon fibers and revealed very stable performance during bending tests (**Figure 25**). The authors coated multilayer films with Cr/Au/PEDOT:PSS on nylon fibers and used them as source/drain electrodes, showing excellent bending stability for use in various chemical and biological sensing applications, with high sensitivity and selectivity. OECTs are a promising candidate for high-sensitive monitoring because they take advantage of the local amplification effect.<sup>[283]</sup> Reports on deep-tissue detection are very few. However, Wu et al. recently developed a fiber-shaped all-in-one OECT on the basis of CNTFs to track biochemical parameters, such as H<sub>2</sub>O<sub>2</sub>, glucose, dopamine, and glutamate. They demonstrated high sensitivity and stability in the physiological environment and reported a seven-day dopamine sensing *in vivo*.<sup>[284]</sup> Finally, a fiber-shaped hydrogen gas sensor was developed by Zhu et al., which they electrochemically grew a palladium sensing layer on a conductive PEDOT:PSS fiber electrode. The PEDOT:PSS@Pd fiber sensor provided flexibility, light weight, knittability, high mechanical strength, and a good H<sub>2</sub> sensing performance at room temperature, under mechanical bending stress, thus making it a good candidate for wearable sensor devices for fast H<sub>2</sub> leak detection.<sup>[285]</sup>

In summary, despite the recent advancements in the field of fiber-shaped devices, there are not yet many commercially available systems. The fiber-shaped sensors are one of the few fiber-shaped devices that have been integrated into functional applications, however, they are still limited to signal detection and monitoring. The combination of an energy harvester device along with a sensor, making it self-powered, is a great advantage since they can be used for long periods and in demanding conditions. In the future, more sensing abilities are awaited from those devices, when the existing challenges are successfully addressed.

## 6.2. Fiber-Shaped LEDs and Other Lighting Devices

Fiber-shaped LEDs are another important functional device that enable the fabrication of light-emitting textiles and those with

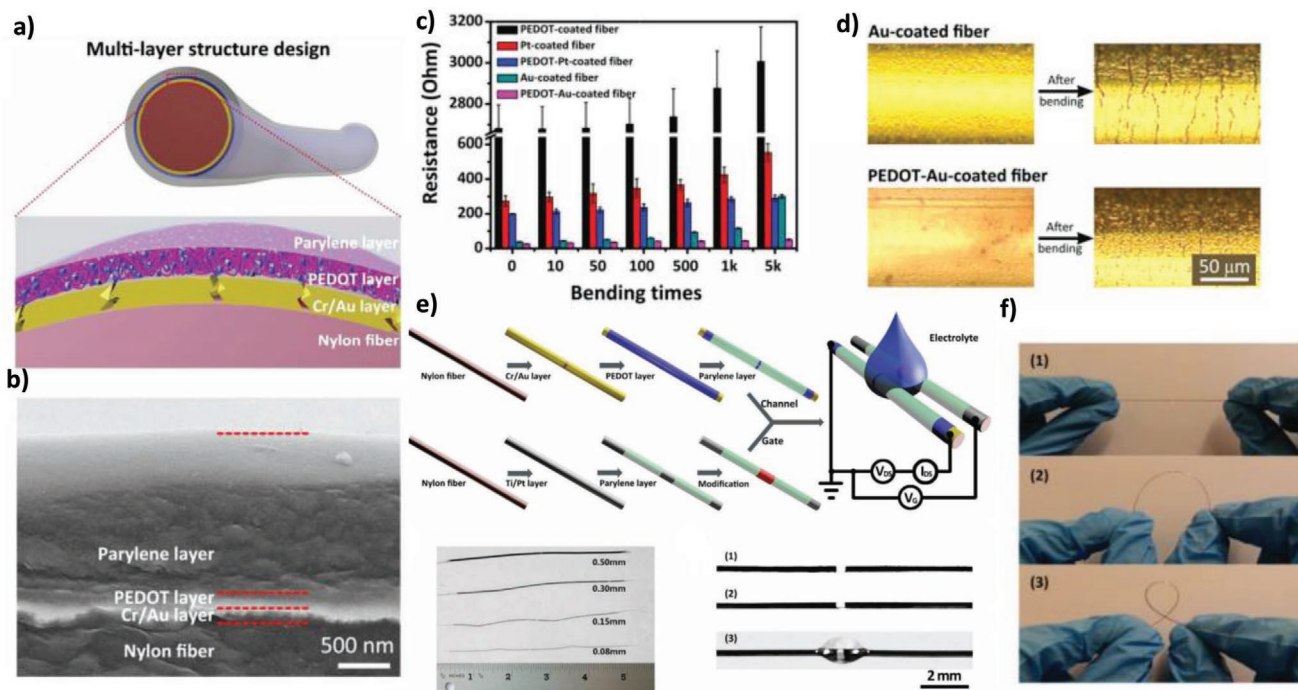


**Figure 25.** a) The design of a core-shell conductive nylon fiber with Cr/Au/PEDOT:PSS/parylene coating. b) SEM image of the cross-section of a core-shell conductive nylon fiber. c) Resistance versus bending times of five kinds of conductive fibers, including Cr/Au, Cr/Au/PEDOT:PSS, PEDOT:PSS, Ti/Pt, and Ti/Pt/PEDOT:PSS-coated fibers. d) Photos of Cr/Au and Cr/Au/PEDOT:PSS-coated fibers before and after 1000 bending tests. e) The fabrication process of functionalized fiber-based channel and gate for an OECT (top). Photograph of fiber-based devices with different diameters: 0.08, 0.15, 0.30, and 0.50 mm (bottom, left). Photograph of a fiber channel 1) before and 2) after coating a PEDOT:PSS layer, and 3) with the adhesion of a drop of water to demonstrate the hydrophilic property on its surface (bottom, right). f) Photograph of a fiber device with different bending statuses: 1) origin, 2) moderate bending, and 3) big bending. Reproduced with permission.<sup>[282]</sup> Copyright 2018, John Wiley & Sons.

Li-Fi communication capabilities. In an LED, electrons and holes are injected in an emitting semiconductor that emits light by radiative recombination. High injection rates and low levels of nonradiative recombination are needed,<sup>[286]</sup> indicating that careful optimization of the materials and the LED structure is instrumental to fabricate highly efficient LED. Typical efficient LED could make use of up to seven layers (plus a substrate) with different functions: one transparent electrode, a hole transport layer (HTL), a hole injection layer (HIL), an emitter layer (EML), an electron injection layer, an electron transport layer (ETL), and a second electrode. Given that LED efficiency is also limited by light outcoupling,<sup>[287]</sup> transparent electrodes are often combined with an antireflection layer to maximize the light output. Furthermore, as the emission of a LED is mainly monochromatic, the fabrication of white LED requires either doping a host matrix with different emitters (for organic LEDs (OLEDs)) or using an additional layer of phosphorous to extend the emission spectrum across the visible light region. Most organic or hybrid LEDs are rather sensitive to oxygen and water, thus proper encapsulation is also needed to achieve durable devices. The complexity of this structure, the use of thin layers, the need for a flexible and mechanically stable structure, and with the requirement of a transparent electrode make the fabrication of fiber-shaped LED a challenging task.

LEDs could be fabricated with inorganic, organic, and hybrid semiconductors. While all of them could be fabricated on flexible substrates,<sup>[288,289]</sup> the wide range of mechanical stresses

experienced in a wearable textile promotes the use of softer materials. OLED, polymer LED (PLED), or perovskite LED (PeLED) are promising candidates in this area because they are known to be flexible and/or stretchable,<sup>[290]</sup> and compatible with solution processing on fiber-shaped materials. Even if vacuum depositions are feasible on fiber-based substrates,<sup>[291]</sup> the use of solution processing is more in line with the scope of producing a large volume of fibers required for a textile. Given the complexity of the fabrication of LEDs, alternative fiber-based lighting devices with simplified structures as light-emitting electrochemical cells (LECs) and alternating current electroluminescence (ACEL) have been evaluated. Three figures of merit could be used to evaluate the quality of LEDs: luminance or brightness ( $\text{cd m}^{-2}$ ), external quantum efficiency (EQE, %), and current efficiency ( $\text{cd A}^{-1}$ ). For a detailed description of these parameters, we refer to a comprehensive review article.<sup>[287]</sup> As a reference, state-of-the-art flexible LEDs have a luminance above  $10\,000\text{ cd m}^{-2}$ , with efficiency in the range of  $130\text{ cd A}^{-1}$  with an EQE of above 60%.<sup>[289]</sup>

### 6.2.1. Fiber-Shaped LEDs

The first fiber-based LED was patented in 2001 by Anil Raj Duggal.<sup>[292]</sup> It showed a structure where the active layers were wrapped around a core, having a transparent conductor on the outer side. The patent already described a method to deal

with the low conductivity of transparent electrodes, adding a thin strip of metal on one side of the fiber. The low conductivity of this layer could be an obstacle to developing long electroluminescent fibers. O'Connor et al. published in 2007 the first paper on fiber-shaped organic LED (Figure 26a).<sup>[291]</sup> The stack of layers of the LED was deposited by thermal evaporation around a polyimide (PI) fiber of 20  $\mu\text{m}$ . Even if solution processing may be more convenient for large-scale production on fibers, the possibility of using the same fabrication process used for highly efficient LEDs is interesting. The fiber was axially rotated at 30 rpm during evaporation to achieve a uniform deposition. The device required the deposition of seven layers, highlighting the complexity of transferring OLED over fiber-based substrates. Nevertheless, compared with planar OLED with the same structure (deposited on silicon or PI), the drop in EQE was rather limited at low driving voltages (i.e., below 5 V). Interestingly, the fiber-based OLED did not show any change in the emission spectrum at different angles. This effect is clearly visible on planar devices due to microcavity effects. One limitation of this structure is the use of thin metals as the light outcoupling electrode, due to the complexity of depositing a transparent electrode over the stack deposited on a fiber. Axially rotating evaporation could provide full coverage of the fiber. However, a transparent electrode is needed on top of the stack.

A possible method to overcome this issue and develop bottom emitting fiber LED was presented in 2018 by Ko et al.<sup>[293]</sup> They developed a method to deposit an OLED stack on a portion of the outer shell of hollow fibers (Figure 26b). After partially embedding the fibers on a PDMS substrate, they deposited the stack starting from an indium tin oxide layer as a transparent electrode. After the deposition of the other layers and the metal electrode, the fibers were detached from the PDMS and ready to be used. The hollow structure was shown to improve the light extraction efficiency with respect to planar OLED, enabling an improvement of EQE from 2.25% to 4.6%. The fibers also exhibited a high luminance of up to 6300  $\text{cd m}^{-2}$  and an efficiency of 11  $\text{cd A}^{-1}$ . However, even if these fibers present high performances, their fabrication process might hinder the scaling up the production of long fibers. As a solution to this problem, Kwon et al. demonstrated a method to deposit most of the layers of a PLED by dip-coating, a technique suitable for mass production of e-textiles.<sup>[11b]</sup> Starting from a PET fiber they deposited PEDOT:PSS and a poly(phenylvinylene) super yellow emitter. The top electrode was made by the deposition of LiF/Al on one side of the fiber, obtaining a bright bottom emissive fiber-shaped PLED. The fibers displayed a high luminance of up to 1458  $\text{cd m}^{-2}$  at 10 V, with a luminous efficiency between 2 and 3  $\text{cd A}^{-1}$ . Even though the efficiency is not very high,

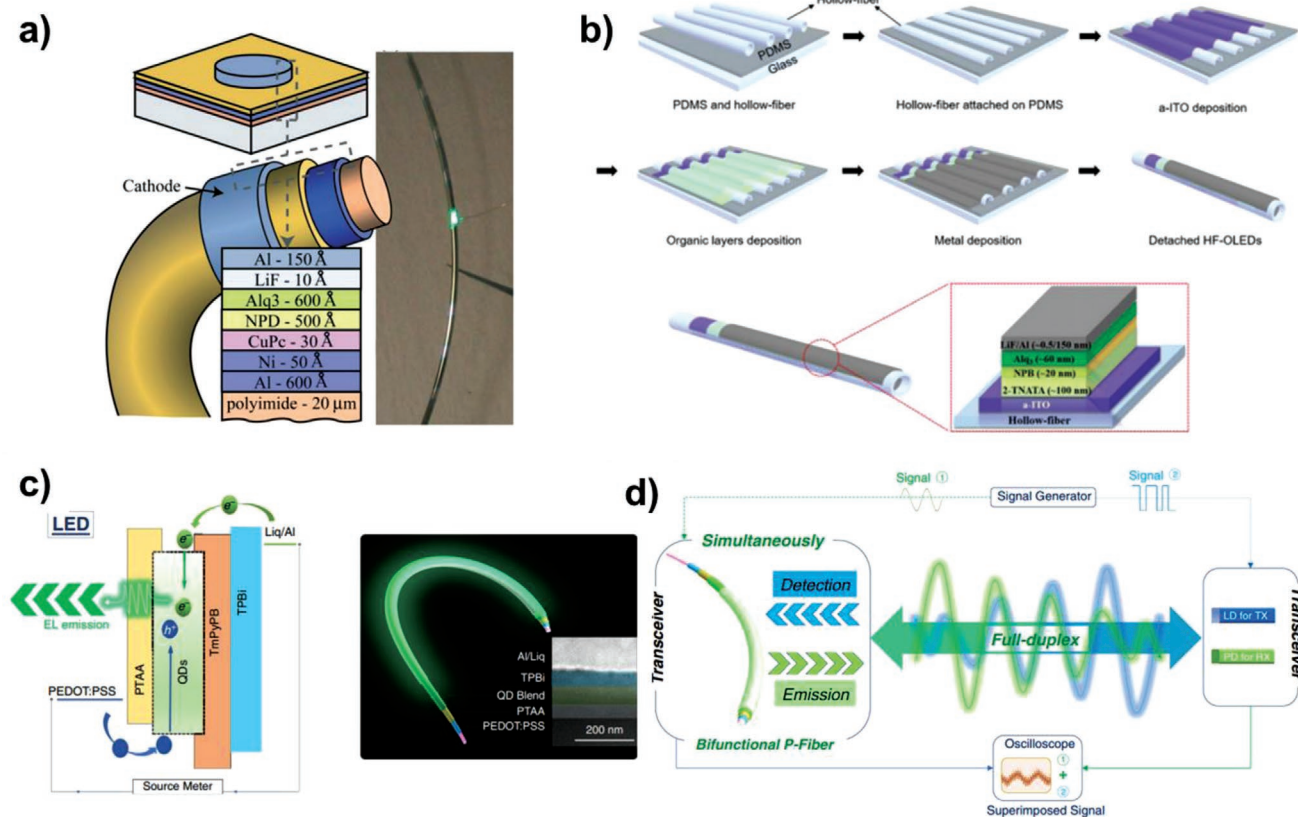


**Figure 26.** a) Structure and photograph of the first OLED fiber reported in literature. The photograph shows a fiber wrapped around a rod emitting in green. Reproduced with permission.<sup>[291]</sup> Copyright 2007, John Wiley & Sons. b) Scheme of the fabrication of a hollow fiber LED. Reproduced with permission.<sup>[293]</sup> Copyright 2018, The Royal Society of Chemistry. c) Scheme and cross-sectional SEM of a PeLED fiber based on quantum dots blended with charge injectors. d) Scheme of the implementation of PeLED fiber in a LiFi full-duplex communication. Reproduced with permission.<sup>[296]</sup> Copyright 2020, Nature Publishing Group.

the luminance already satisfied the range required for conventional display applications, e.g., smart phones.<sup>[294]</sup> In 2018, the same group reported significant improvement on this type of structure.<sup>[295]</sup> By optimizing the structure (i.e., including a low-temperature solution-processable zinc oxide–polyethylenimine (ZnO:PEI) nanocomposite layer in between the PEDOT and the emitter), they achieved a high luminance of above 10 000 cd m<sup>2</sup> at 10 V and an efficiency of 11 cd A<sup>-1</sup> at ≈6 V. In terms of luminance, the fiber showed even better performance compared to planar OLED. The fiber was also hand-woven into textiles to prove the integration in clothes.

Finally, considering that hybrid metal halide perovskites emerged as a very promising candidate for PV and LED application, Shan et al. demonstrated the fabrication of a PeLED fiber (Figure 26c).<sup>[296]</sup> In this case, dip-coating was used for the deposition of all the layers (bottom electrode, HTL, emitter blend, and ETL) beside the top metal electrode. The emitter layer was composed of perovskite QDs blended with the charge injectors, namely, polytriarylamine for holes and 1,3,5-tri[(3-pyridyl)-phen-3-yl]benzene for electrons. The fiber had a luminance of up to 300 cd m<sup>-2</sup> with an efficiency of 1.67 cd A<sup>-1</sup>. Even if these values are still considerably lower than those in OLED and PLED fibers, the PeLED has some specific advantages. Compared with the other electroluminescent materials. The perovskite materials show a very narrow emission spectrum that could be beneficial for display applications. To support this application, the same paper demonstrated the fabrication of blue and red PeLED fiber by changing the composition of the perovskite QDs. The PeLED could be used also as a photodetector, which enables its use in Li-Fi communication (Figure 26d). The authors demonstrated that the fiber could be used simultaneously as a receiver and as a transmitter with a bandwidth of 50 kb s<sup>-1</sup>, thus obtaining a full-duplex Li-Fi communication suitable for transmitting audio signals.

In summary, fiber-shaped LEDs based on organic and perovskite semiconductor materials are developed. Although there performance parameters are far lower than their planar state-of-the-art counterparts,<sup>[287,297]</sup> fiber-shaped LEDs are advantageous due to their super flexibility and light-weight. Super yellow fiber-shaped OLEDs have demonstrated brightness above 10 000 cd m<sup>-2</sup> (Table 7). Currently, the research focus on fiber-shaped LEDs is considerably low and most report do not consider a standard protocol to report figure of merits, which makes it difficult to compare with their planar counterparts. For example, photoluminescence quantum yield is an important parameter to quantify optical quality of emitter layer, which

is never reported for any fiber-shaped LED. Current efficiency of fiber-shaped LEDs is an order of magnitude lower than, for example, best performing planar perovskite LED.<sup>[298]</sup> This suggests that the defects in the emitter film as well as the device heterojunctions require future optimization. Also, the current fiber-shaped LEDs only report green or yellow emission; there are no reports on blue, red, or near infrared emission. Future research should also target blue and red emission so that a solid-state white light source might be realized by mixing different colors.

### 6.2.2. Fiber-Shaped ACELs and LECs

Before the advent of LED fibers, the only fiber-shaped lighting devices were based on phosphorus layers sandwiched in between insulators and two electrodes.<sup>[292]</sup> They are based on ACEL and they emit light upon the application of an alternating voltage to stimulate the emission from the phosphorus. This makes ACEL devices less suitable for wearable electronics due to the high voltage requirements and the need for alternating current (requires an inverter if used with a battery). Even if these devices suffer from low brightness compared with LED, recent works continued the investigation into this topic. Liang et al. developed ACEL based on a PET fiber by using Ag NWs as the inner and outer electrodes, ZnS as phosphor and silicone as an insulator.<sup>[299]</sup> All the constituent layers were deposited by dip-coating (Figure 27a), enabling the rapid fabrication of many fibers. The thin layers and the use of silicone provide the fiber with high mechanical stability, being able to have a stable emission upon tensile stress of up to 547 MPa, withstanding test as bending with 2 mm radius and resistance to artificial human sweat. The fiber showed a wide emission spectrum and it required relatively high voltages to achieve high luminance, e.g., 60 and 195 V (frequency of 2 kHz) to achieve brightness of 19 and 202 cd m<sup>-2</sup>, respectively. Sun et al. demonstrated an ACEL fiber that could be easily dissolved in water to ease the recycling process.<sup>[300]</sup> They used a PVA fiber, Ag NWs as electrodes, and phosphorous (ZnS:Cu and ZnS:Cu,Mn) that were blended in PVP. In this manner, the insulating layer could be deposited together with the emitter, thereby simplifying the fabrication process. In addition, high voltages were needed to achieve high luminance (100 cd m<sup>-2</sup> at 300 V), but the authors showed that such voltage did not cause heating even after 3 h of continuous operation. The transparent electrodes could also be prepared by carbon-based materials as aligned CNT sheets

**Table 7.** Figure of merit of fiber-shaped LEDs.

Device architecture	Fiber thickness [mm]	EL emission peak [nm]	Current efficiency [cd A <sup>-1</sup> ]	Luminance [cd m <sup>-2</sup> ]	EQE [%]	Refs.
PI/Al/Ni/CuPc/NPD/Alq <sub>3</sub> /LiF/Al	20	≈550			0.18	[291]
HF/a-ITO/2-TNATA/NPB/Alq <sub>3</sub> /LiF/Al		518	11	6300	4.6	[293]
PET/PEDOT:PSS/SY <sup>a</sup> /LiF/Al	300	550	3	1458	–	[11b]
PET/PEDOT:PSS/ZnO:PEI/SY <sup>a</sup> /MoO <sub>3</sub> /Al/Al <sub>2</sub> O <sub>3</sub>	90–300	Super yellow	11	13 937	–	[295]
PEDOT:PSS/PTAA/perovskite QDs/TmPyPB/TPBi/Liq/Al		516	1.67	100		[296]

<sup>a</sup>)SY = super yellow (SY, Merck Co., Mw = 1668000 g mol<sup>-1</sup>).

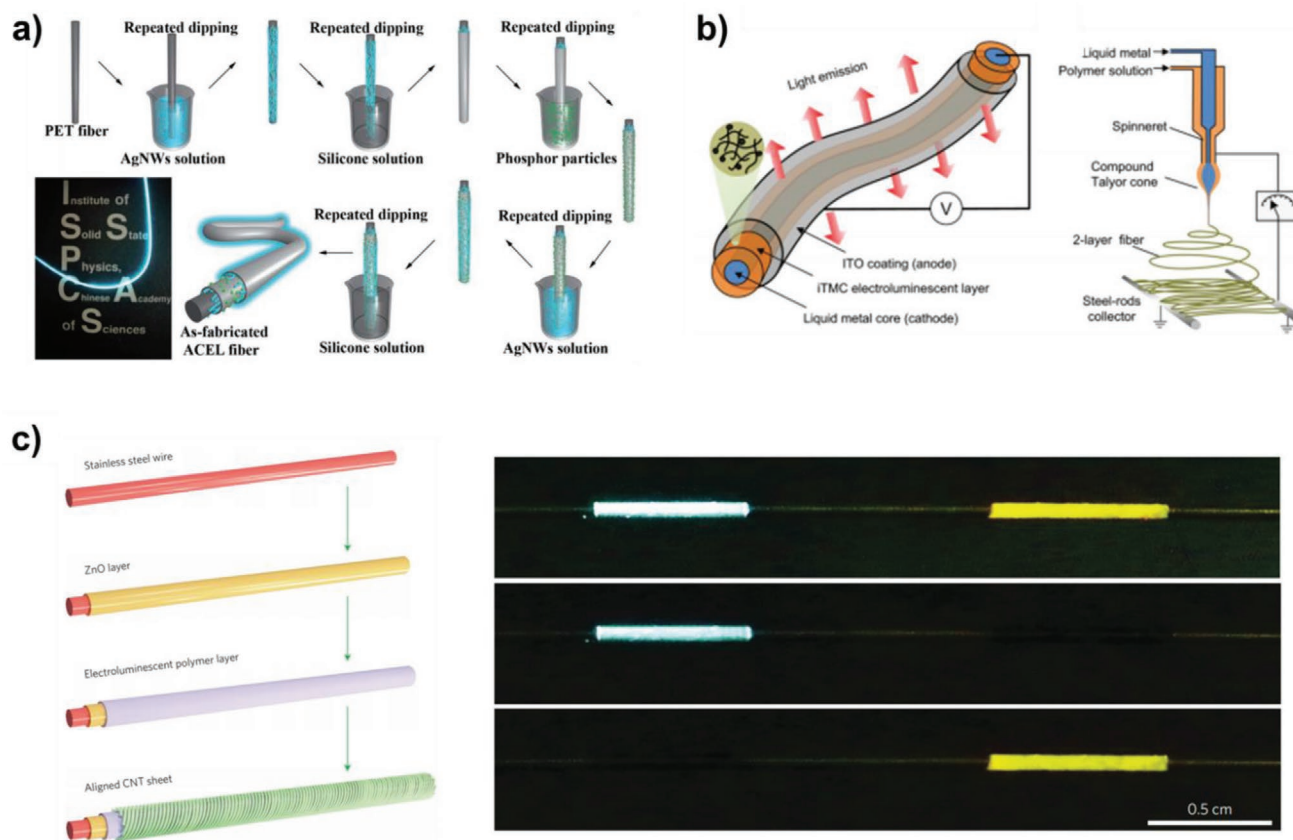


**Figure 27.** a) Fabrication process of an ACEL electroluminescent fiber by a sequence of dip-coating steps. In the bottom left subpanel, it is possible to observe a picture of the fiber during emission. Reproduced with permission<sup>[299]</sup> Copyright 2017, John Wiley & Sons. b) Structure and scheme of the fabrication process of an LEC nanofiber based on iTMC emitters. Reproduced with permission<sup>[303]</sup> Copyright 2012, American Chemical Society. c) (Left) Structure and fabrication scheme of an LEC fiber based on an LEP. (Right) Picture of the emission from the fiber using two different LEPs. Reproduced with permission<sup>[302]</sup> Copyright 2015, Nature Publishing Group.

wrapped around a fiber.<sup>[301]</sup> When this material is combined with an elastic fiber and a silicone elastomer, the resulting ACEL fiber could also be stretched up to 200% without losses in the luminance.

Another method to fabricate electroluminescent fibers with good luminance at low voltages is the use of LECs. In this case, an organic emitting layer that contains mobile ions is sandwiched among two electrodes. The emitter could be either an ionic transition-metal complex (iTMCs) or a light-emitting polymer (LEP), and both type of materials were implemented in fibers. Zhang et al. demonstrated highly efficient fiber-shaped polymer LEC<sup>[302]</sup> by using a steel wire coated with ZnO, an LEP, and a CNT sheet wrapped around it (Figure 27c). These devices demonstrated major improvement compared with ACEL fibers, with a high luminance of  $600 \text{ cd m}^{-2}$  at 13 V (with driving currents of  $70 \text{ mA cm}^{-2}$ ). While the efficiency was not particularly high ( $0.83 \text{ cd m}^{-2}$ , EQE of 0.35%), the low voltage and high luminance made these approaches more suitable for wearable electronics than ACEL fiber. The size of LEC fiber could also be strongly reduced by fabricating nanofiber-based iTMCs (Figure 27b) with a modified electrospinning method.<sup>[303]</sup> By using a liquid metal core, fabricating fiber with a diameter below  $1 \mu\text{m}$  it was possible, with a maximum luminance of  $23 \text{ cd m}^{-2}$  and an EQE of 0.27% at 6 V. Structures based on

ACEL fibers are generally could be more robust than fiber-shaped LEDs that enables the use of transparent conductive electrodes. However, they are not as bright as fiber LEDs and they require high voltages for light emission, thus preventing safe application in wearables. LECs could be a good compromise among LED and ACEL fibers because they could provide compatibility with vacuum-free production, and a sufficient brightness at low voltages.

### 6.3. Fiber-Shaped Chromatic Devices

Chromatic devices capable of reversibly changing their optical properties under external stimulations have attracted great attention and undergone rapid development in the last few decades due to their various potential applications, such as optical components,<sup>[304]</sup> sensors,<sup>[305]</sup> detectors,<sup>[306]</sup> displays,<sup>[307]</sup> and wearable electronics.<sup>[308]</sup> Significant research efforts have been devoted to the chromatic devices that change colors in response to electric field, specific light wavelength, thermal heating, pH level, and mechanical stress. Among these applications, the wearable chromatic electronics represent the most active one as they provide new opportunities for intelligent human-machine interactions.<sup>[309]</sup> Therefore, fiber-shaped chromatic devices are

more preferred as this type of device could be woven to textiles with breathability.<sup>[310]</sup> As color changes could be triggered via different stimulations, chromatic devices could be divided into different classifications. In this part, the recent progress of state-of-the-art fiber-shaped chromatic devices, including mechanochromic, thermochromic, and electrochromic devices, was discussed.

### 6.3.1. Mechanochromic Fibers

As the name implies, mechanochromic fibers could reversibly change their colors under mechanical deformations of the fiber. These colors could be generated from the stress-driven chemical transformations,<sup>[311]</sup> and the mechanical deformation-induced changes in periodic lattice constants of the structure-colored materials.<sup>[312]</sup> Compared with chromic fibers utilizing stress-driven mechanochemical transformations, mechanochromic fibers with structural color have received increasing interest for their applications in wearable electronics because they are safe to use and simple to implement in various

platforms.<sup>[313]</sup> For example, a novel mechanochromic fiber was prepared by simply depositing polymer microspheres (polystyrene microspheres) onto an elastic PDMS fiber (Figure 28a).<sup>[308]</sup> The color of the fiber could be tuned by varying the size and the center-to-center distance of the polymer microspheres (Figure 28b). Figure 28c shows that the mechanochromic fibers possessed reversible and rapid multicolor changes (i.e., red, green, and blue) during the stretch and release actions. High sensitivity and stability were maintained after 1000 deformation cycles. Furthermore, these elastic photonic-crystal fibers could be woven into patterns and smart fabrics for various display and sensing applications (Figure 28d).

Commercially available polymer fibers were also employed to prepare dye-free mechanochromic fibers.<sup>[314]</sup> Core-shell microspheres, coated on the commercially available black spandex fibers were arranged into a photonic crystal structure to display brilliant colors covering the visible light region. The colors of the commercially available black spandex fibers could be easily controlled by varying the diameters of the core-shell microspheres. Interestingly, the high elasticity of such fibers can be used to vary the center-to-center distance between the

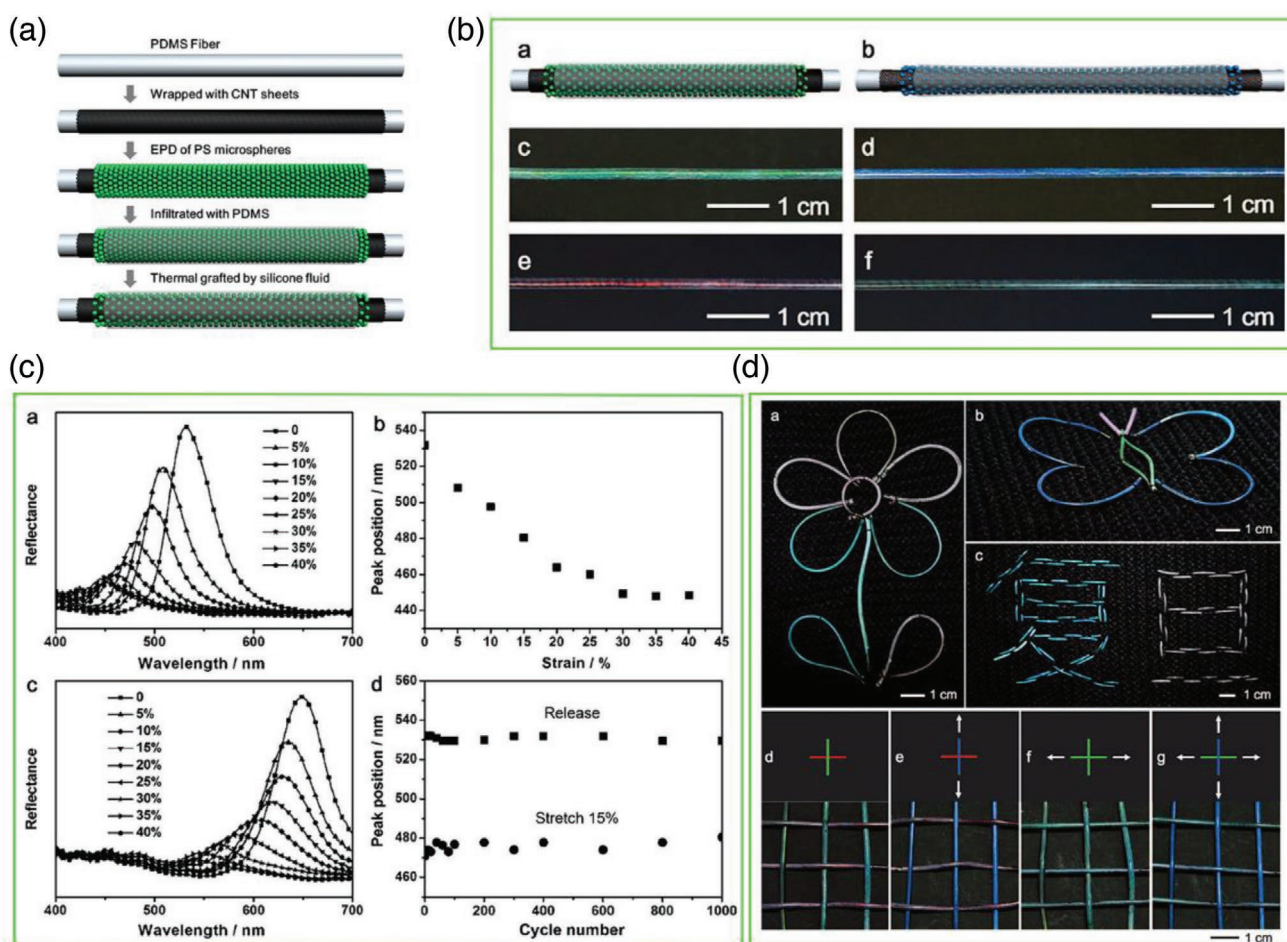


**Figure 28.** a) Schematic illustration to the preparation of the mechanochromic photonic crystal fiber. b) Schematic illustration of the mechanochromic fibers and the photographs of the mechanochromic fibers made from 200 and 240 nm PS (polystyrene) microspheres before and after stretching. c) Mechanochromic performance of the elastic photonic-crystal fibers. d) Chromatic patterns and fabric are made from elastic photonic-crystal fibers. Reproduced with permission.<sup>[308]</sup> Copyright 2015, John Wiley & Sons.

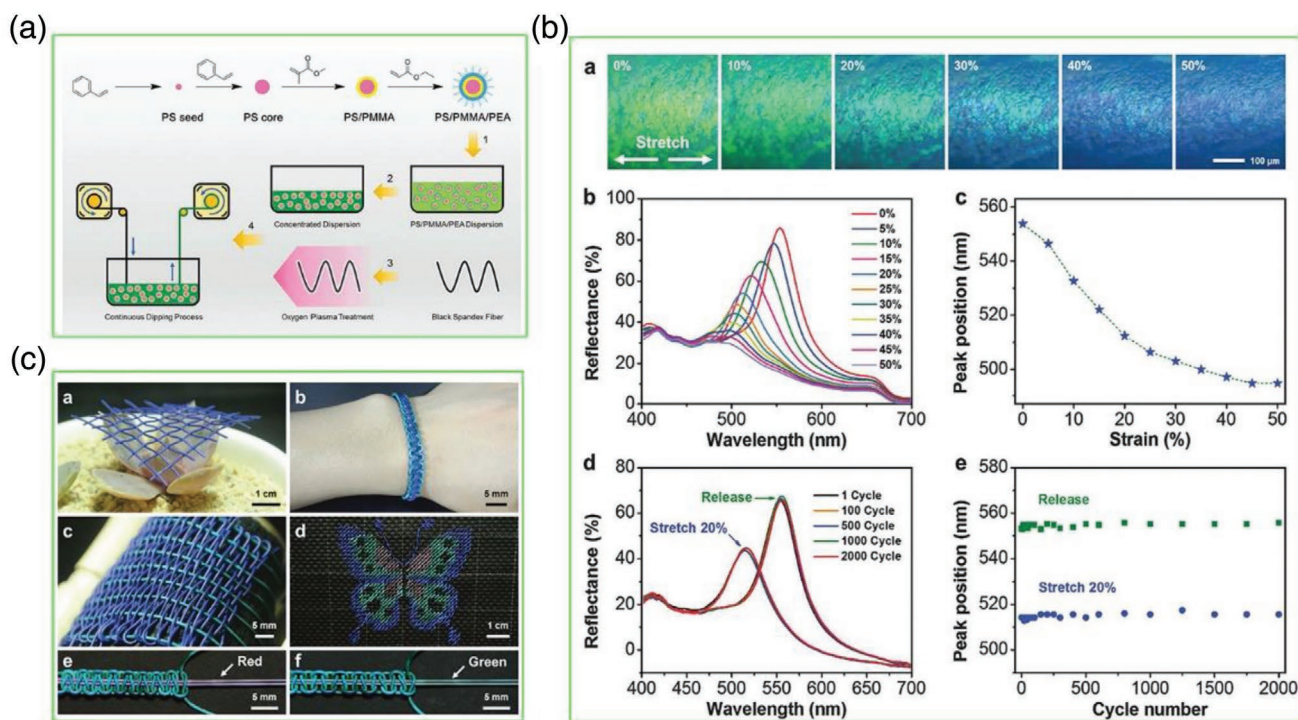


**Figure 29.** a) Schematic illustration of the steps used in preparation of mechanochromic fibers: 1) synthesis of core–shell microspheres; 2) concentration of microsphere dispersions; 3) surface modification of spandex fibers; 4) continuous deposition of microspheres onto the spandex fibers. b) Mechanochromic performance of the photonic crystal fiber made from polystyrene/poly(methyl methacrylate)/poly(ethyl acrylate) core–shell microspheres with a diameter of 273 nm. c) Photographs of chromatic patterns and textiles made from the mechanochromic fibers. Reproduced with permission.<sup>[314]</sup> Copyright 2016, The Royal Society of Chemistry.

core–shell microspheres leading to distinct color change under stretching. **Figure 29a** shows the continuous fabrication process of the mechanochromic fibers.

Such a simple fabrication process not only offers a great potential as an alternative to the traditional dyeing technique but also presents a promising commercialization platform for the smart wearable textile industry. **Figure 29b** reveals that the color of a mechanochromic fiber could be changed from green to blue with increasing strains from 0% to 50%. **Figure 29c** shows that the mechanochromic fibers provide unique advantages in many applications, such as textiles and displays, because they are easily woven into color-tunable patterned textiles

### 6.3.2. Thermochromic Fibers

Thermochromic materials exhibit a reversible color change in response to a change in temperature. Such materials have various applications, including smart windows,<sup>[315]</sup> adaptive camouflage,<sup>[316]</sup> and displays.<sup>[317]</sup> Thermochromic materials could also be employed to make chromatic fibers, where flexible architectures offer novel functionalities. The conventional method used to fabricate thermochromic fibers is by spinning a mixture consisting of a polymer powder and a thermochromic microcapsule. Zhang et al. used a typical single-screw extruder spinning machine to spin the mixture of commercially available

polypropylene and thermochromic microcapsule particles.<sup>[318]</sup> The resultant composite polypropylene fibers were shown to exhibit vivid temperature-dependent colors when such fibers were exposed to different temperatures (**Figure 30a**). As the color changes in the above mentioned thermochromic fibers are triggered by the ambient temperature change, precisely controlling the ambient temperatures on demand is often challenging. Therefore, controlling the temperature of the thermochromic fiber controlled by using an electric heater, is the easiest strategy to change the color on demand.<sup>[319]</sup> Such class of thermochromic fibers is referred to as electrothermal chromatic fibers, where the temperature is controlled via Joule heating.<sup>[320]</sup> Li et al. reported a stretchable and multicolor electrothermal chromatic fiber that was based on RGO.<sup>[25]</sup> Interestingly, this electrothermal chromatic fiber was functionalized to become elastic and conductive.

**Figure 30b** depicts the fabrication process of the electrothermal chromatic fiber. This simple fabrication process holds a great promise for future continuous fabrication of long fibers. **Figure 30c** reveals the multilayered sheath–core structure of the electrothermal chromatic fiber. The PE–rGO–TiO<sub>2</sub> component served as the Joule heating component, while the commercially available thermochromic ink serves as the color-changing module. **Figure 30d** shows that the dark-green color of the electrothermal chromatic fiber could be bleached under Joule heating and stretching due to the increased resistance. The infrared (i.e., thermal) images also clearly showed that the

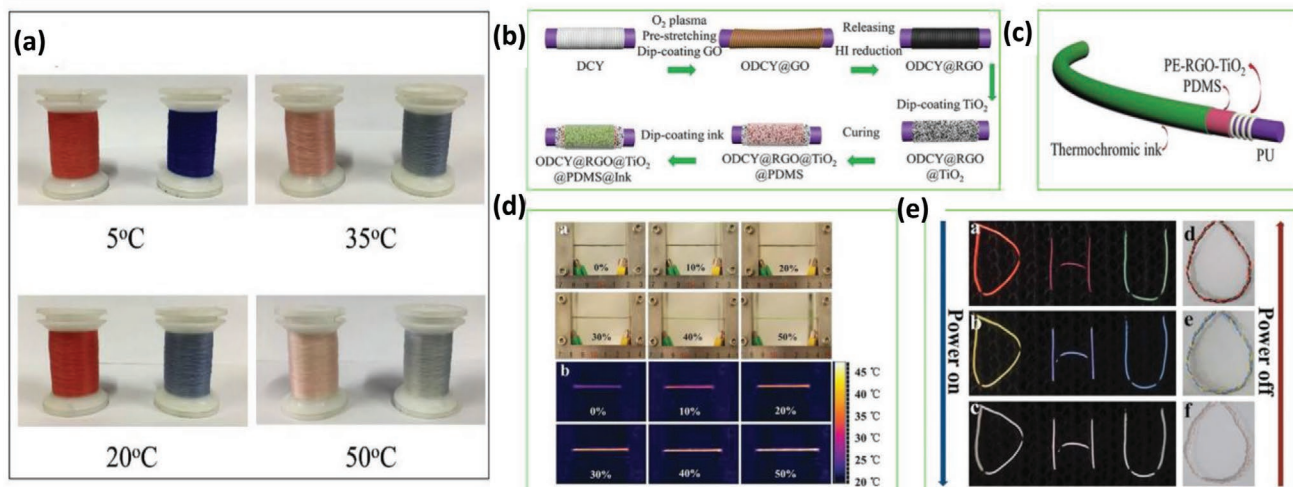


**Figure 30.** a) Color change of thermosensitive fibers under various temperatures. Reproduced with permission.<sup>[318]</sup> Copyright 2019, Elsevier. b) Schematic illustrations of the fabrication process of an electrothermal chromatic fiber. c) Schematic illustration of the structure of the stretchable electrothermal chromatic fiber. d) Digital photographs and their corresponding thermal images of stretchable electrothermal chromatic fibers during the stretching process at a constant current density of  $142 \text{ mA cm}^{-1}$ . e) Electrothermal chromatic fibers formed into letter patterns when being woven into textiles. Reproduced with permission.<sup>[25]</sup> Copyright 2017, The Royal Society of Chemistry.

color change in the fiber was due to temperature change. Different commercially thermochromic inks exhibiting various heat-dependent colors could be notably used to access other colors (Figure 30e) for smart clothing. Another representative example of electrothermal chromatic fiber was reported by Lu et al.<sup>[321]</sup> As shown in Figure 31a, the elastic conductive fiber was made via layer-by-layer assembly of the CNTs and silage NWs onto PDMS fibers. The elastic electrothermal chromatic

fiber was prepared by in situ polymerization of diacetylene monomer on the PDMS-based elastic conductive fiber where a protective layer (i.e., silicone layer) was coated on top of polydiacetylene. Figure 31b shows that the fiber could be used to prepare a “Chinese knot” and can be easily wound on a glass rod. The fiber can be woven into smart fabric patterns due to its excellent stretchability and flexibility, while still preserving its excellent chromatic properties (Figure 31c).

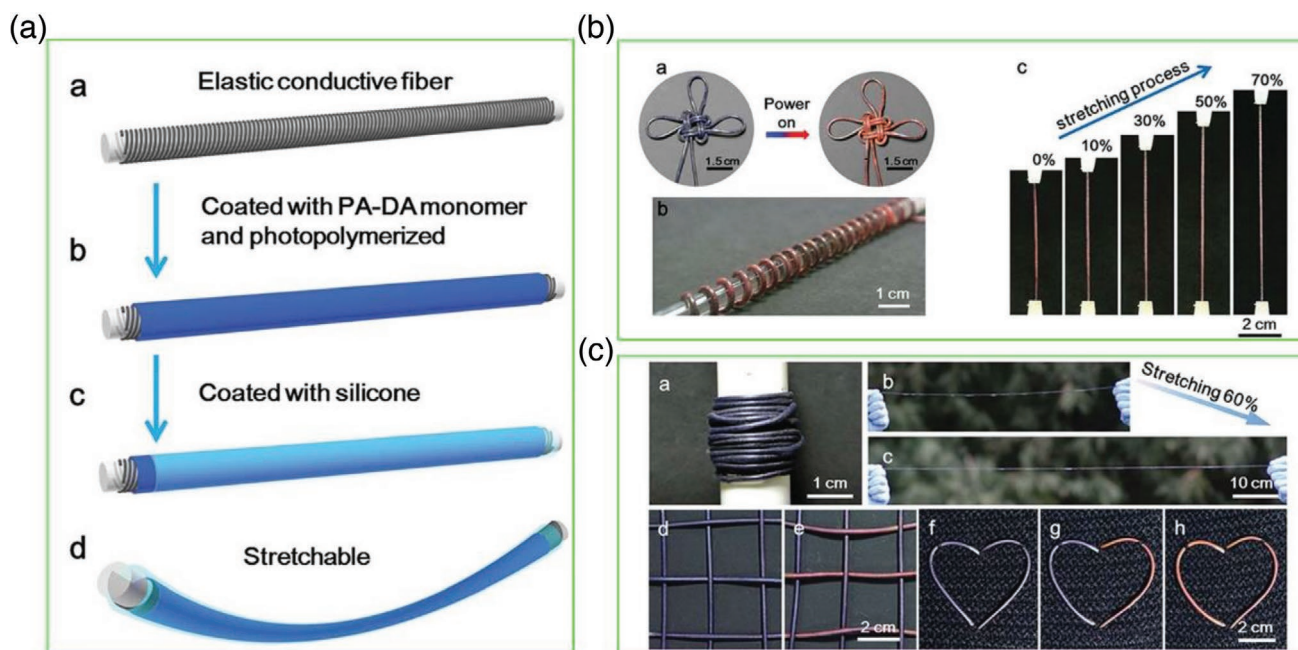


**Figure 31.** a) Schematic illustration of the preparation process of the electrothermal chromatic fiber. b) Flexible and stretchable characterizations of the electrothermal chromatic fiber. c) Photographs of the electrothermal chromatic fibers and woven smart fabric patterns. Reproduced with permission.<sup>[321]</sup> Copyright 2016, The Royal Society of Chemistry.

### 6.3.3. Electrochromic Fibers

Electrochromic materials, which are the most representative chromatic materials, could reversibly change colors or optical properties through redox reactions under an applied electric field.<sup>[322–324]</sup> These electrochromic materials demonstrated a great promise in many applications, including smart windows,<sup>[18,33,323,325,326]</sup> and displays.<sup>[307,327]</sup> With the demand for wearable electronics, new applications and functionalities were enabled via electrochromic materials. The combination of electrochromic technology with flexible and wearable technology is expected to lead to novel electrochromic devices that have great potential for use in future smart clothes and implantable displays.<sup>[328]</sup> Among the wearable technologies, electrochromic fibers with compelling optical properties are considered the most promising technology for next-generation wearable electronics.<sup>[310]</sup>

Given that a typical planar electrochromic device requires two parallel electrodes assembled as one electrochemical cell,<sup>[324,326]</sup> the main challenge for an electrochromic fiber is the realization and assembly of the two electrodes on the fiber surface.<sup>[332]</sup> Li et al. demonstrated red, green, and blue electrochromic fibers by utilizing commercially available stainless steel wires (SSWs) and electrochromic polymers.<sup>[17]</sup> As shown in **Figure 32a**, various electrochromic polymers (i.e., poly(3,4-ethylenedioxythiophene), poly(3-methylthiophene), and

poly(2,5-dimethoxyaniline)) were electropolymerised on the surface of the core SSWs, which served as working electrode in the fiber-shaped electrochromic device. Next, the core SSWs were dipped into the polymer gel electrolyte and dried at ambient temperature. Finally, another SSW with smaller diameter was wrapped onto the working electrode, where the electrolyte layer served as a spacer to avoid short circuit between the two electrodes. As depicted in **Figure 32b**, under the application of a voltage between the electrodes, different electrochromic polymers coated on the SSWs displayed different colors. Another example of electrochromic fibers utilized PANI-coated aligned CNT as the two electrodes. Here, an elastic fiber served as the matrix to enable fiber stretching.<sup>[329]</sup> **Figure 32c,d** illustrates electrochromic fiber-shaped electrical energy storing supercapacitors that could be woven into fabrics to display designed patterns.

By using dual helix metal electrodes along a plastic fiber substrate and subsequently depositing tungsten oxide ( $\text{WO}_3$ ) and poly(3-methylthiophene) (P3MT) separately on the two electrodes, Zhou et al. fabricated freestanding electrochromic fibers with rapid response times ( $\approx 5$  s) and high coloration efficiency.<sup>[330]</sup> They used the structure with parallel coil electrodes on a single fiber to demonstrate multicolor electrochromic fibers. As illustrated in **Figure 33a**, two adhesive tapes were wrapped as a mask onto a polyvinyl chloride fiber. Next, a thin layer of Au was deposited onto the fiber's exposed surface to

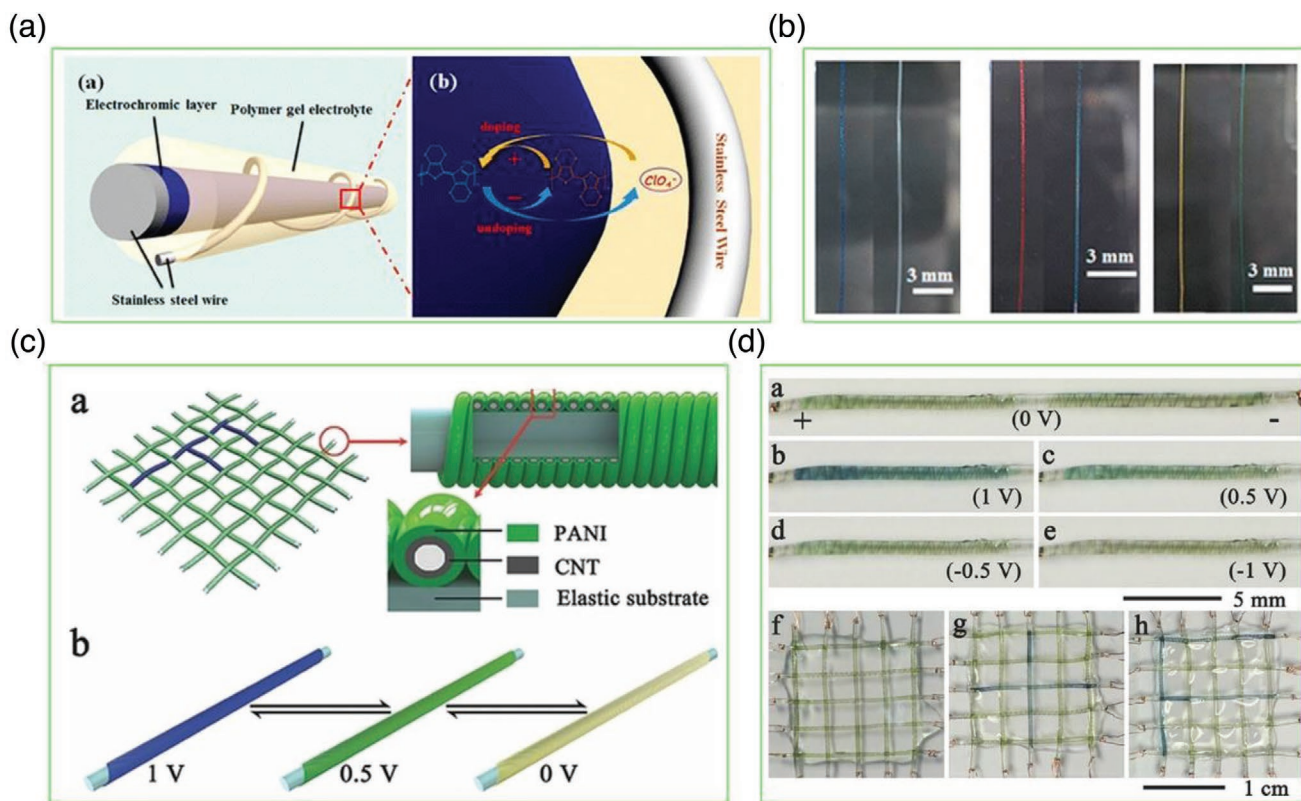


**Figure 32.** a) Illustration of the structure of the electrochromic fibers and the electrochromic mechanism for poly(3,4-ethylenedioxythiophene) electrochromic layer. b) Digital photographs of the electrochromic fibers using various electrochromic polymers. Reproduced with permission.<sup>[17]</sup> Copyright 2014, American Chemical Society. c) Schematic illustration of the structure and color display function of the electrochromic, wearable fiber-shaped supercapacitor. d) Chromatic transitions during the charge–discharge process. Reproduced with permission.<sup>[329]</sup> Copyright 2014, John Wiley & Sons.

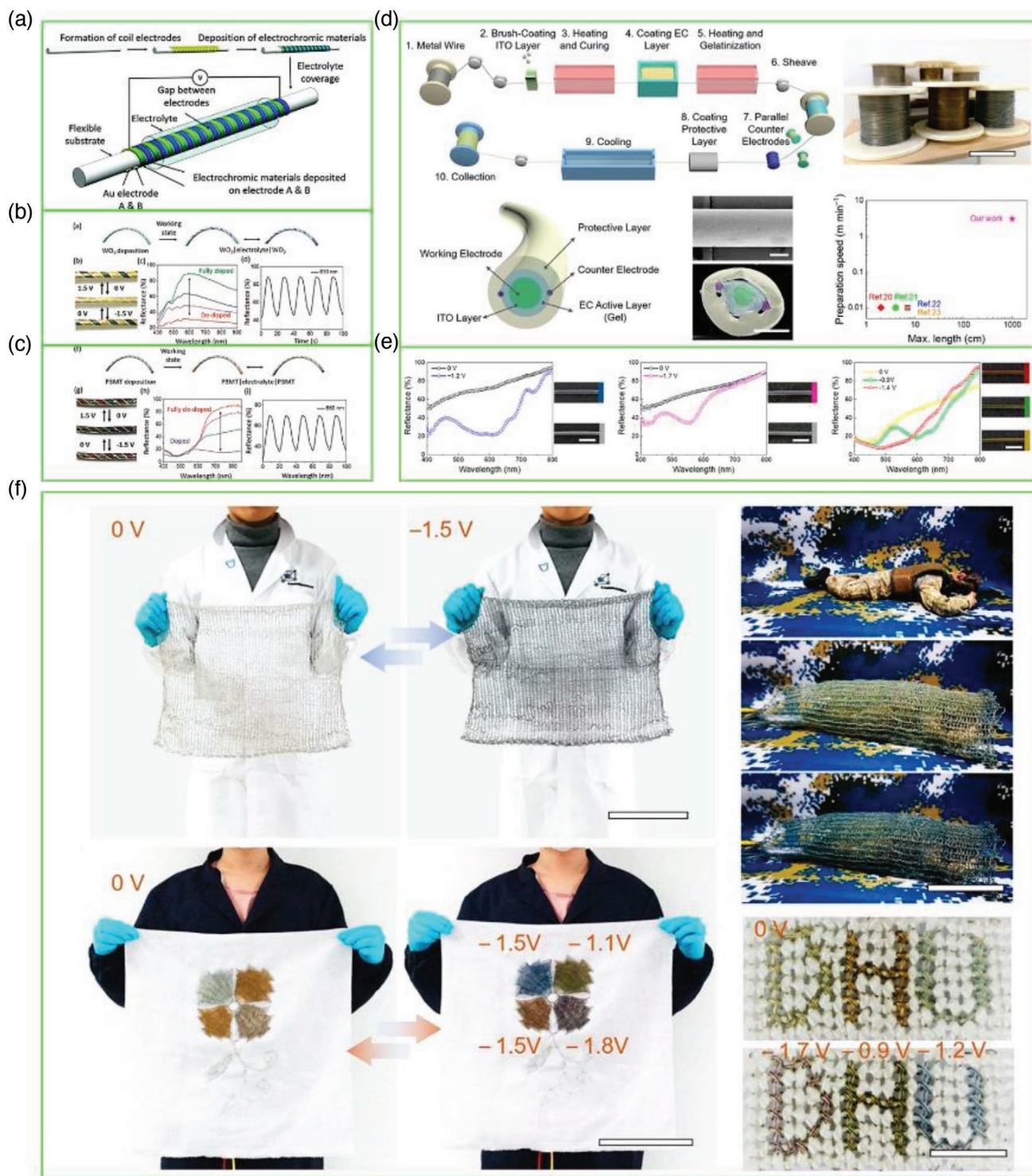


**Figure 33.** a) Schematic representation of the preparation process of parallel coil electrodes. Electrochromic properties of the electrochromic fibers using b) tungsten oxide and c) poly(3-methylthiophene) as active materials. Reproduced with permission.<sup>[330]</sup> Copyright 2018, John Wiley & Sons. d) Schematic illustration of the continuous fabrication process of the electrochromic fibers having a parallel dual-counter-electrode configuration. e) The different colors of the electrochromic using different viologens. f) Some representative applications of the electrochromic fibers. Reproduced with permission.<sup>[331]</sup> Copyright 2020, American Chemical Society.

form two coiled parallel Au electrodes.  $\text{WO}_3$  and P3MT were electrodeposited onto the Au layers to realize the electro-

chromic functionality, followed by covering the entire fiber with a solid electrolyte ( $\text{LiClO}_4/\text{PMMA}$ ). Considering different

electrochromic materials exhibit different colors. The  $\text{WO}_3$ -based electrochromic fibers display reversible color switching between gold and dark green colors, while the P3MT-based electrochromic fibers display color switching between dark green and red colors. As shown in Figure 33b,c, the reflectance spectra and the switching profiles validate the excellent electrochromic performance of the electrochromic fibers, including the large optical difference and the rapid switching times.

Recently, Fan et al. demonstrated the first continuously fabricated long electrochromic fibers.<sup>[331]</sup> The electrochromic fibers achieved multiple uniform and rapid color-switching by introducing various electrochromic materials (viologens) and a unique device configuration. Figure 33d schematically illustrates the continuous fabrication process of the electrochromic fibers, which can easily produce hundreds of meters long electrochromic fibers. Such a continuous fabrication process enables the construction of parallel dual-counter-electrode structure. This process is critical for realizing uniform electric field needed for rapid and uniform color-switching. Furthermore, such a continuous fabrication process is compatible with numerous electrochromic materials that can be switched between various colors (e.g., blue, magenta, green, and dull red) (Figure 33e). Hundreds of meters long electrochromic fibers can be easily woven into textiles for various applications, including military camouflage and wearable displays (Figure 33f).

In summary, although mechanochromic fibers, thermochromic fibers, and electrochromic fibers having excellent chromatic properties were achieved (Table 8), these fibers still suffer

durability issues for real-world applications. The identification of their practical applications needs further investigation. In addition, the integration of other functionalities (e.g., energy harvest, energy storage, sensors, and shape memory) with the chromatic fibers may facilitate new opportunities for the development of next-generation chromatic fibers.

## 7. Fiber-Based Integrated Systems

Integrated systems represent an ensemble of two or more energy conversion (solar cells, NGs and so on), storage (SCs and batteries), or others (sensors, photodetectors, smart windows, and so on) systems. Ideally, two or more systems are combined as a single unit in a way that the output of one system works as the input to the other. Some examples of such integrated systems include i) a self-powered storage system employing a solar cell connected to a storage unit, ii) a combination of photodetector and sensor, iii) wearable textile that involves fiber-shaped NGs, solar cells, and SCs, and iv) self-powered photodetectors storage units such as SCs are used to power photodetectors.<sup>[100,157,188,333,334,335]</sup> It must be noted that combining more than two systems as a single unit might make the fabrication of such a device complex. Integrated energy conversion and storage systems represent one of the most commonly employed type of such systems allowing photogenerated energy to be captured and stored in a single unit. In one of the early reports, a photocapacitor comprising a DSSC and activated carbon in contact with an

**Table 8.** Summary of fiber-shaped chromatic devices.

Type of chromatic fibers	Materials	Fabrication method	Advantages	Disadvantages	Cycle stability	Refs.
Mechanochromic fibers	PS microspheres	Electrodeposition	Good stretchability Obvious color shift	Nonuniform color distribution Less compatibility with fabrication of long fibers	1000	[308]
Mechanochromic fibers	PS@PMMA microspheres	Continuous dipping	Good compatibility with fabrication of long fibers Rapid color switching	Complexity in fabrication	2000	[314]
Thermochromic fibers	Thermochromic microcapsule	Spinning	Ease of fabrication Good compatibility with fabrication of long fibers	Limited stretchability	60	[318]
Thermochromic fibers	Commercial thermochromic inks	Dipping	Good stretchability Obvious color shift	Less compatibility with fabrication of long fibers	1000	[25]
Electrothermal chromatic fibers	Polydiacetylene	Dipping	Good stretchability Obvious color shift	Less compatibility with fabrication of long fibers	1000	[321]
Electrochromic fibers	Poly(3,4-ethylenedioxythiophene), etc.	Electrodeposition	Obvious color shift Color tunable via voltage	Limited stretchability Less weavability	NA	[17]
Electrochromic fibers	Polyaniline	Electropolymerization	Color tunable via voltage Good stretchability	Less compatibility with fabrication of long fibers	10 000	[329]
Electrochromic fibers	$\text{WO}_3$ , poly(3-methylthiophene)	Electrodeposition	Obvious color shift	Limited stretchability Less compatibility with fabrication of long fibers Less weavability	200	[330]
Electrochromic fibers	Viologens	Continuous dipping	Obvious color shift Good weavability Good compatibility with fabrication of long fibers	Limited stretchability	300	[331]

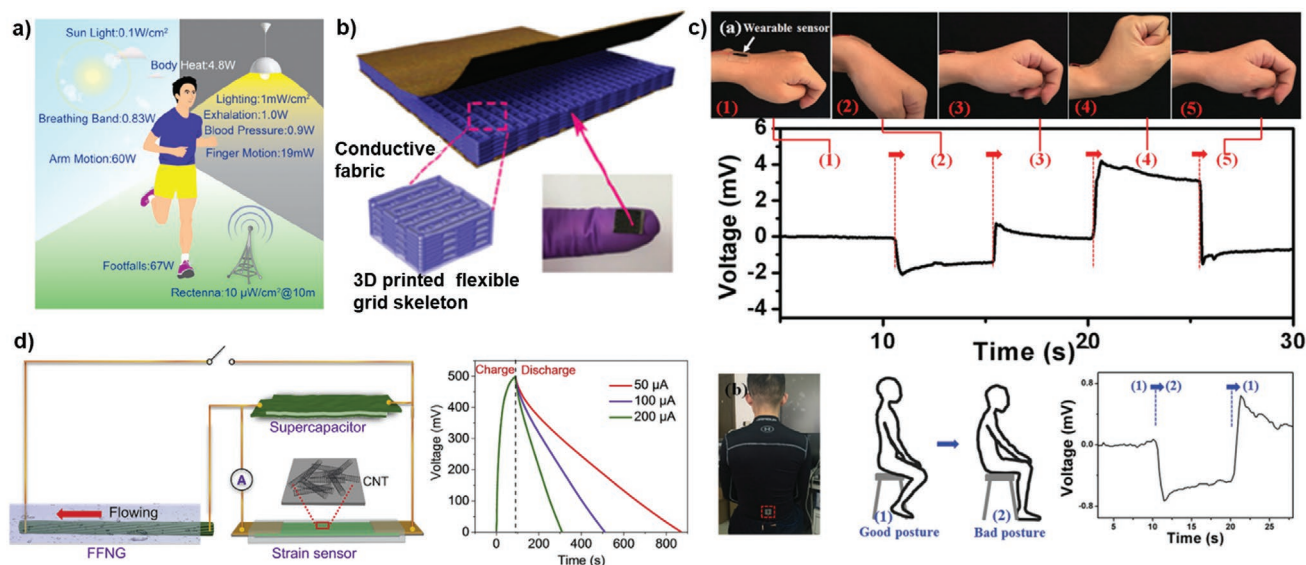


**Figure 34.** a) A list of potential energy harvesting sources from environment and human body that can potentially replace the need for energy storage units for wearable systems or enhance their lifetime. b) Three-dimensional printed flexible FTEG with a 3D grid skeleton and conductive fabric. Adapted with permission.<sup>[335]</sup> Copyright 2019, American Chemical Society. c) Applications of the piezoionic sensor as wearable sensor for the monitoring of large scale human motions. (Upper panel) Response signals of the wearable sensor for monitoring of the wrist bending with different directions. The photographs show that wearable sensor is attached on the wrist joint and the wrist joint moving process started from the flat state (1) to the finally flat state (5) (Middle panel). The generated voltage indicates that the direction as well as the amplitude of the wrist bending can be clearly detected and distinguished. (Bottom panel) Monitoring of the person's sitting posture by this wearable sensor. The wearable sensor is attached to the person's back, marked in the red box in the photograph. When the person's sitting posture is from good (marked as (1)) to bad (marked as (2)), the sensor could generate clear electrical signal in response to the change. Adapted with permission.<sup>[337]</sup> Copyright 2016, Wiley-VCH Verlag GmbH & Co. KGaA, Weinheim. d) An integrated system employing self-powered FFNG as energy harvester, SC as energy storage device, and a strain sensor. Charge-discharge curves of the integrated, self-powered device at different discharge currents. Adapted with permission.<sup>[338]</sup> Copyright 2020, Cell Press.

electrolyte, which stores the photogenerated charges at the double layer, was introduced.<sup>[336]</sup>

A common issue with conventional planar integrated system is their inflexibility for modern applications such as wearable textiles which requires omnidirectional flexibility in structure and design and also compatibility with mass production. Fiber- or wire-based systems are emerging as a successful alternative for future applications as they offer a wide flexibility over design and integration. These systems are soft, flexible, light-weight and are stretchable and therefore can be effectively integrated with human body (Figure 34a,b). These integrated systems can be used for a range of application such as to detect muscular motion (Figure 34c), continuous monitoring of body temperature and pressure, respiration monitoring, phototherapy, and so on.<sup>[335,337]</sup> Key issues such as mechanical robustness and complexity of integrating multiple systems as a single unit without compromising system efficiency, however, remain to be solved.

A common type of integrated systems combines energy harvesting and storage in a single fiber.<sup>[339]</sup> This has been achieved by using a stainless steel wire coated with polyaniline, which worked as a joint electrode materials to integrate DSSC and SC.<sup>[333]</sup> The system reported an overall energy conversion efficiency of 2.1%, higher than a previous report<sup>[339]</sup> employing ZnO and graphene NWs as a common electrode material. A more complex system can involve harvesting energy from multiple sources, such as from body motion in addition to the

sunlight. Wen et al.<sup>[100]</sup> reported a hybrid self-charging power textile system that uses NGs and DSSCs to harvest mechanical energy from body motion and solar energy from sunlight, respectively, and store them as chemical energy in FSCs. Thanks to the all-fiber-shaped architecture of the system, individually made DSSC, NG, and FSCs were woven into a textile structure in series/parallel connection. The flexibility and functionality of the integrated system was demonstrated at several indoor and outdoor conditions.

Another example of integrated system is integrating a storage system with a functional device such as sensors. Pan et al.<sup>[272]</sup> reported an all-in-one stretchable coaxial-fiber-based sensing system for strain detection. The complex device assembly involved multistep coating of PEDOT:PSS, MnO<sub>2</sub>, PPy, and CNTs around an elastic fiber such that the MnO<sub>2</sub>@PEDOT:PSS@CNT form a positive electrode comprises of PPy@CNT form a negative electrode. The single fiber-based integrated device yielded an energy density of 1.42 mWh cm<sup>-3</sup> and retained over 85% of initial capacitance value after 6000 bending cycles at a strain level of 200%. In another example, a self-powered integrated device for strain detection is demonstrated using MoS<sub>2</sub>-encapsulated CFs (Figure 34d).<sup>[338]</sup> Herein, fiber-shaped fluidic NGs delivered a stable output voltage of 540 mV and a power density of 10.8 W m<sup>-2</sup>. The integrated system achieved a maximum power conversion-energy efficiency of around 11% and a voltage output of 3.1 V, which they used to turn on a green LEDs and a commercial digital timer.

## 8. Conclusion and Outlook

Fiber-shaped electronic devices represent one of the most promising technology for the next-generation wearable electronics as they offer unprecedented versatile functionalities to the textiles. As wearable electronics are rapidly evolved and their applications expand, the field is continuing to attract more and more attention from both academia and industry. Few in-depth reviews with critical perspective on fiber-shaped electronics,<sup>[340]</sup> energy-related devices,<sup>[341]</sup> or rechargeable batteries are cited for further referencing and reading.<sup>[342]</sup> However, real-world applications of the fiber-shaped electronic devices are still at their infancy and require more research and development. In the next few years, researchers need to work closely with industry and to focus their attention on safety, packaging, and to develop robust fiber-shaped devices. It is envisioned that fiber-shaped electronic devices will open up new avenues in wearable electronics.

To achieve this goal, conductive fibers with superior electrical conductivity, softness, reversible mechanical deformation, and robustness are urgently needed. Also, the washing stability, breathability, and flexibility should be taken into consideration when weaving the conductive fibers for textiles. Up to now, various materials for the critical fiber component have been developed such as metal wires, nanowires, and nanoparticles possessing high electrical conductivity but limited flexibility and washability. Conducting polymers, carbon nanomaterials, such as CNTs and graphenes, binary and ternary metal oxides, MXenes, and their composites can be materials of choice to simultaneously achieve superior electrical conductivity and flexibility. While it is challenging to simultaneously achieve excellent electrical conductivity and superior stretchability and robustness in a pristine compound, hybrid materials are capable for synergizing or combining various functionalities in a single materials system. A unique opportunity of hybrid materials is in the proper development of MOFs into fibers. MOFs offer significant advantages from the two materials domains, viz., organic and inorganic; therefore, MOFs would be an excellent area to be further developed into functional fibers. Further, the current research on electronic fibers are majorly centered around electronic materials, thereby leaving a large gap with the current choice of textile polymers. Developing hybrid materials engaging the current choice of textile polymers are expected to open up a new era for the design and development of textile electronics.

Fiber-shaped LEDs and PVs are both benefited from the recent progress in planar counterparts based on solution-processed semiconductors, especially organic and halide perovskite ones. However, they still require the use of at least one thermal evaporation step to deposit the cathode, complicating the development of low-cost, large volume production. Compared to the planar devices they still lag in terms of efficiency, but the fast pacing progress in planar counterparts suggests that large improvements can be expected. Even so, the lack of an efficient fabrication process suitable for long fibers is preventing the demonstration of large-area electroluminescent and photovoltaic fabrics. A critical challenge is the solution processing of transparent electrodes, where CNTs, Ag NW, PEDOT-based layers, or graphene-based inks are expected to be a possible

solution to this problem. Besides, proof of long-term stability should be provided to exploit these technologies on commercial products. A big challenge for the long-term stability consists in the implementation of an efficient encapsulation compatible with woven textiles. Single fiber encapsulation or fabric encapsulation needs to ensure the durability of the fibers under environmental factors as water or oxygen as well as under mechanical stress, and are particularly needed for LED/PV-based fibers. Even if there are several approaches for flexible encapsulation of LED/PV, large efforts will be needed to develop a process suitable to mass production of electroluminescent fibers.

Fiber-based physical and chemical sensors have already provided efficient sensing functions in wearable, portable, and implantable electronics. Importantly, the recent developments in fiber-shaped nanogenerators that convert mechanical pressure into electrical energy suggests that self-powered systems to monitor human health, structural deformation, environmental conditions, etc., are not far in the future. Monolithic integration of an energy harvester with the sensing element onto a fiber-shaped device will open new prospects by taking advantage of human motions, fluid flow, or mechanical vibrations to produce the energy required for the smart sensing element. Few research works have been accomplished in this area, however, efficient operation and, importantly, scalability for industrialization is yet to be reached.

Fiber-shape SCs have accomplished much progress in recent years. To attain higher performance devices, the selection of proper active material, fiber or current collector, electrolyte, and device layout are of predominant criteria. The four types of FSCs have their own pros and cons. All-inclusive, PFSCs are simple to assemble and RFSCs furnish highest performance among all the five FSCs. The improper assembly of device layouts and packaging can lead to short circuit or device failure in FSCs. Concisely, a high performance reliable FSC should have two fiber electrodes that maintain uniform distance between them to avoid the occurrence of short circuit, meanwhile the interaction surface area between the cathode and anode must be significant. Pivotal attention has to be on fabricating fibers, different from conventional carbon-based yarns with enhanced stretchability to withstand repeated wear and tear, and to synthesize electrolytes with high ionic mobility, biocompatibility and nontoxicity. Active materials with 3D structure and high porosity are solution to design FSC electrodes with less weight and high specific capacitance. Furthermore, asymmetric hybrid FSCs would avail broad potential range with magnified energy density. Ultimately, FSCs should maintain all its basic structural criteria like flexibility, mechanical strength, lightweight, weavability, firm encapsulation along with excellent electrochemical performances, i.e., good specific capacitance, high energy density, and reliable cyclic stability.

Low energy density could be one of the major disadvantages of existing fibrous batteries. In order to achieve higher energy density, more active materials would be required to store more charges. However, depositing more active materials will certainly increase the overall diameter of the devices, which will lead to poor mechanical flexibility as well as difficulties in weaving. Even though the most versatile route is to make all the battery components flexible, the realistic scenarios could be far more complex than what had been considered. Taking the

typical bending deformation as examples, the top components are subjected to tensile stress along the bending tangential direction with compressive stress at the bottom components. In order to retain favorable performance, the battery components need to sustain electrochemical performance and mechanical integrity under both tensile and compressive force which limits the overall performance of the existing devices.

Fiber-shaped chromatic devices represent one of the most promising smart technology for the next-generation wearable electronics as they offer unprecedented versatile functionalities of the textiles. As wearable electronics develop and their applications expand, the field is continuing to attract more and more attention from both academia and industry. However, real-world applications of the fiber-shaped chromatic devices are still at their infancy and require more research and development. In the next few years, researchers need to work closely with industry and to focus their attention on safety, packaging, and to develop robust fiber-shaped chromatic devices.

In general, although much progress has been already accomplished in all of the discussed areas of fiber-shaped electronics—in some more than the others—these devices still suffer from several drawbacks, including 1) low compatibility with the current textile industry where yarns/threads play a pivotal role, 2) impermeable to air, leading to poor wearing experiences, and 3) limited flexibility depending on the substrates and encapsulation deployed. As fiber-shaped electronics must be knitted or woven into flexible clothing, they must fulfil certain criteria to ensure successful development and commercialization of the fibrous device, including 1) low internal resistance especially along the length of the fiber, which could extend up to hundreds of meters, 2) easy fabrication techniques with efficient short-circuit prevention, 3) successful insertion of flexible active element for high efficiency, 4) allow implementation of suitable separator (where needed) for better short-circuit prevention, 5) proper encapsulation, 6) final yarn/thread with diameter identical to the normal yarns, 7) excellent mechanical performance for weaving with a machine, and 8) final yarns/thread that look soft and fibrous instead of plastic. The proper understanding of the device design, working mechanism, and difficulties in achieving the true performance can lead the researchers toward the realization of real-time application from laboratory to industry level. Furthermore, integration of two or more type of electronic devices onto fibers or textiles possess even more strict requirements and necessitates optimization of each constituent and of the integration methods applied. Despite the many materials and devices limitations need to be overcome, it is envisioned that fiber-shaped electronic devices will soon open up new avenues in wearable electronics.

## Acknowledgements

M.V., A.S., and P.A. acknowledge support of this work by the project "Development of Materials and Devices for Industrial, Health, Environmental and Cultural Applications" (MIS 5002567), which is implemented under the "Action for the Strategic Development on the Research and Technological Sector," funded by the Operational Programme "Competitiveness, Entrepreneurship and Innovation" (NSRF 2014-2020) and cofinanced by Greece and the European Union (the European Regional Development Fund). R.J. and J.K.L. acknowledge

the UMP grant (RDU 203301) for complex NIR absorbing perovskites. A.R. and L.S.-M. acknowledge the Indo-German joint project grant (Department of Science and Technology (DST), India, Project No: INT/FRC/DAAD/P-09/2018 and Deutscher Akademischer Austauschdienst (DAAD), Germany, Project No: 57389570) for flexible supercapacitors.

Open access funding enabled and organized by Projekt DEAL.

## Conflict of Interest

The authors declare no conflict of interest.

## Keywords

bendable electronic devices, electrospinning, fiber electronics, flexible electronics, wearable electronics

Received: May 8, 2021

Revised: June 10, 2021

Published online:

- [1] M. Zohair, K. Moyer, J. Eaves-Rathert, C. Meng, J. Waugh, C. L. Pint, *ACS Nano* **2020**, *14*, 2308.
- [2] Y. Jang, S. M. Kim, G. M. Spinks, S. J. Kim, *Adv. Mater.* **2020**, *32*, 2070034.
- [3] F. Mo, G. Liang, Z. Huang, H. Li, D. Wang, C. Zhi, *Adv. Mater.* **2020**, *32*, 1902151.
- [4] a) X. Li, Z.-H. Lin, G. Cheng, X. Wen, Y. Liu, S. Niu, Z. L. Wang, *ACS Nano* **2014**, *8*, 10674; b) Z. Liu, D. Qi, G. Hu, H. Wang, Y. Jiang, G. Chen, Y. Luo, X. J. Loh, B. Liedberg, X. Chen, *Adv. Mater.* **2018**, *30*, 1704229; c) Q. Shi, J. Sun, C. Hou, Y. Li, Q. Zhang, H. Wang, *Adv. Fiber Mater.* **2019**, *1*, 3.
- [5] J. Deng, Y. Zhang, Y. Zhao, P. Chen, X. Cheng, H. Peng, *Angew. Chem., Int. Ed.* **2015**, *54*, 15419.
- [6] Y. Xing, Y. Xu, Q. Wu, G. Wang, M. Zhu, *J. Mater. Chem. C* **2021**, *9*, 439.
- [7] Z. Li, Z. L. Wang, *Adv. Mater.* **2011**, *23*, 84.
- [8] X. Fang, Z. Yang, L. Qiu, H. Sun, S. Pan, J. Deng, Y. Luo, H. Peng, *Adv. Mater.* **2014**, *26*, 1694.
- [9] a) A. M. Zamarayeva, A. E. Ostfeld, M. Wang, J. K. Duetz, I. Deckman, B. P. Lechêne, G. Davies, D. A. Steingart, A. C. Arias, *Sci. Adv.* **2017**, *3*, e1602051; b) L. Ma, S. Chen, D. Wang, Q. Yang, F. Mo, G. Liang, N. Li, H. Zhang, J. A. Zapfen, C. Zhi, *Adv. Energy Mater.* **2019**, *9*, 1803046.
- [10] H. Li, Z. Liu, G. Liang, Y. Huang, Y. Huang, M. Zhu, Z. Pei, Q. Xue, Z. Tang, Y. Wang, B. Li, C. Zhi, *ACS Nano* **2018**, *12*, 3140.
- [11] a) Z. Zhang, L. Cui, X. Shi, X. Tian, D. Wang, C. Gu, E. Chen, X. Cheng, Y. Xu, Y. Hu, J. Zhang, L. Zhou, H. H. Fong, P. Ma, G. Jiang, X. Sun, B. Zhang, H. Peng, *Adv. Mater.* **2018**, *30*, 1800323; b) S. Kwon, W. Kim, H. Kim, S. Choi, B.-C. Park, S.-H. Kang, K. C. Choi, *Adv. Electron. Mater.* **2015**, *1*, 1500103; c) W. Miao, *Chem. Rev.* **2008**, *108*, 2506.
- [12] G. Chen, G. Wang, X. Tan, K. Hou, Q. Meng, P. Zhao, S. Wang, J. Zhang, Z. Zhou, T. Chen, Y. Cheng, B. S. Hsiao, E. Reichmanis, M. Zhu, *Natl. Sci. Rev.* **2020**, nwa209.
- [13] a) J. Zhao, Y. Zhang, Y. Huang, J. Xie, X. Zhao, C. Li, J. Qu, Q. Zhang, J. Sun, B. He, Q. Li, C. Lu, X. Xu, W. Lu, L. Li, Y. Yao, *Adv. Sci.* **2018**, *5*, 1801836; b) Y. Jia, X. Yue, Y. Wang, C. Yan, G. Zheng, K. Dai, C. Liu, C. Shen, *Composites, Part B* **2020**, *183*, 107696; c) A. Canales, S. Park, A. Kiliyas, P. Anikeeva, *Acc. Chem. Res.* **2018**, *51*, 829.
- [14] L. Wang, L. Wang, Y. Zhang, J. Pan, S. Li, X. Sun, B. Zhang, H. Peng, *Adv. Funct. Mater.* **2018**, *28*, 1804456.

- [15] a) G. Qu, J. Cheng, X. Li, D. Yuan, P. Chen, X. Chen, B. Wang, H. Peng, *Adv. Mater.* **2016**, *28*, 3646; b) J. Ren, L. Li, C. Chen, X. Chen, Z. Cai, L. Qiu, Y. Wang, X. Zhu, H. Peng, *Adv. Mater.* **2013**, *25*, 1155.
- [16] P. Li, Z. Jin, L. Peng, F. Zhao, D. Xiao, Y. Jin, G. Yu, *Adv. Mater.* **2018**, *30*, 1800124.
- [17] K. Li, Q. Zhang, H. Wang, Y. Li, *ACS Appl. Mater. Interfaces* **2014**, *6*, 13043.
- [18] H. Li, W. Zhang, A. Y. Elezzabi, *Adv. Mater.* **2020**, *32*, 2003574.
- [19] Y. Huang, Y. Huang, W. Meng, M. Zhu, H. Xue, C. S. Lee, C. Zhi, *ACS Appl. Mater. Interfaces* **2015**, *7*, 2569.
- [20] G. Shao, R. Yu, X. Zhang, X. Chen, F. He, X. Zhao, N. Chen, M. Ye, X. Y. Liu, *Adv. Funct. Mater.* **2020**, *30*, 2003153.
- [21] S. Lee, S. Shin, S. Lee, J. Seo, J. Lee, S. Son, H. J. Cho, H. Algadi, S. Al-Sayari, D. E. Kim, T. Lee, *Adv. Funct. Mater.* **2015**, *25*, 3114.
- [22] Z. Yang, Z. Zhai, Z. Song, Y. Wu, J. Liang, Y. Shan, J. Zheng, H. Liang, H. Jiang, *Adv. Mater.* **2020**, *32*, 1907495.
- [23] C. Xiang, W. Lu, Y. Zhu, Z. Sun, Z. Yan, C. C. Hwang, J. M. Tour, *ACS Appl. Mater. Interfaces* **2012**, *4*, 131.
- [24] G. Cai, M. Yang, J. Pan, D. Cheng, Z. Xia, X. Wang, B. Tang, *ACS Appl. Mater. Interfaces* **2018**, *10*, 32726.
- [25] Q. Li, K. Li, H. Fan, C. Hou, Y. Li, Q. Zhang, H. Wang, *J. Mater. Chem. C* **2017**, *5*, 11448.
- [26] J. Wu, Z. Wang, W. Liu, L. Wang, F. Xu, *ACS Appl. Mater. Interfaces* **2019**, *11*, 44735.
- [27] L. Li, K. Wang, H. Fan, X. Zhu, J. Mu, H. Yu, Q. Zhang, Y. Li, C. Hou, H. Wang, *Mater. Horiz.* **2021**, *8*, 1711.
- [28] A. Chhetry, H. Yoon, J. Y. Park, *J. Mater. Chem. C* **2017**, *5*, 10068.
- [29] C. Zhu, X. Guan, X. Wang, Y. Li, E. Chalmers, X. Liu, *Adv. Mater. Interfaces* **2018**, *6*, 1801547.
- [30] F. Sun, M. Tian, X. Sun, T. Xu, X. Liu, S. Zhu, X. Zhang, L. Qu, *Nano Lett.* **2019**, *19*, 6592.
- [31] Y. Zhang, W. Zhang, G. Ye, Q. Tan, Y. Zhao, J. Qiu, S. Qi, X. Du, T. Chen, N. Liu, *Adv. Mater. Technol.* **2019**, *5*, 1900880.
- [32] a) H. Z. Li, J. W. Chen, M. Q. Cui, G. F. Cai, A. L. S. Eh, P. S. Lee, H. Z. Wang, Q. H. Zhang, Y. G. Li, *J. Mater. Chem. C* **2016**, *4*, 33; b) H. Li, J. Li, C. Hou, D. Ho, Q. Zhang, Y. Li, H. Wang, *Adv. Mater. Technol.* **2017**, *2*, 1700047.
- [33] H. Li, L. McRae, C. J. Firby, A. Y. Elezzabi, *Adv. Mater.* **2019**, *31*, 1807065.
- [34] Y.-L. Tong, B. Xu, X.-F. Du, H.-Y. Cheng, C.-F. Wang, G. Wu, S. Chen, *Macromol. Mater. Eng.* **2018**, *303*, 1700664.
- [35] W. Li, Y. Zhou, Y. Wang, L. Jiang, J. Ma, S. Chen, F. L. Zhou, *Adv. Electron. Mater.* **2020**, *7*, 2000865.
- [36] X. Wang, G. Chen, L. Cai, R. Li, M. He, *ACS Appl. Mater. Interfaces* **2021**, *13*, 8952.
- [37] X. Chen, H. Lin, P. Chen, G. Guan, J. Deng, H. Peng, *Adv. Mater.* **2014**, *26*, 4444.
- [38] J. Mu, C. Hou, G. Wang, X. Wang, Q. Zhang, Y. Li, H. Wang, M. Zhu, *Adv. Mater.* **2016**, *28*, 9491.
- [39] J. Wang, C. Yan, K. J. Chee, P. S. Lee, *Adv. Mater.* **2015**, *27*, 2876.
- [40] a) D. Baran, R. S. Ashraf, D. A. Hanifi, M. Abdelsamie, N. Gasparini, J. A. Rohr, S. Holliday, A. Wadsworth, S. Lockett, M. Neophytou, C. J. Emmott, J. Nelson, C. J. Brabec, A. Amassian, A. Salleo, T. Kirchartz, J. R. Durrant, I. McCulloch, *Nat. Mater.* **2017**, *16*, 363; b) J. Y. Kim, J. W. Lee, H. S. Jung, H. Shin, N. G. Park, *Chem. Rev.* **2020**, *120*, 7867; c) X. Zheng, Y. Hou, C. Bao, J. Yin, F. Yuan, Z. Huang, K. Song, J. Liu, J. Troughton, N. Gasparini, C. Zhou, Y. Lin, D.-J. Xue, B. Chen, A. K. Johnston, N. Wei, M. N. Hedhili, M. Wei, A. Y. Alsalloum, P. Maity, B. Turedi, C. Yang, D. Baran, T. D. Anthopoulos, Y. Han, Z.-H. Lu, O. F. Mohammed, F. Gao, E. H. Sargent, O. M. Bakr, *Nat. Energy* **2020**, *5*, 131.
- [41] a) Q. Burlingame, X. Huang, X. Liu, C. Jeong, C. Coburn, S. R. Forrest, *Nature* **2019**, *573*, 394; b) Y. Cui, H. Yao, J. Zhang, T. Zhang, Y. Wang, L. Hong, K. Xian, B. Xu, S. Zhang, J. Peng, Z. Wei, F. Gao, J. Hou, *Nat. Commun.* **2019**, *10*, 2515; c) S. Liu, J. Yuan, W. Deng, M. Luo, Y. Xie, Q. Liang, Y. Zou, Z. He, H. Wu, Y. Cao, *Nat. Photonics* **2020**, *14*, 300; d) C. Yan, S. Barlow, Z. Wang, H. Yan, A. K. Y. Jen, S. R. Marder, X. Zhan, *Nat. Rev. Mater.* **2018**, *3*, 18003.
- [42] a) T. Chen, L. Qiu, Z. Yang, H. Peng, *Chem. Soc. Rev.* **2013**, *42*, 5031; b) M. Hatamvand, E. Kamrani, M. Lira-Cantú, M. Madsen, B. R. Patil, P. Vivo, M. S. Mehmood, A. Numan, I. Ahmed, Y. Zhan, *Nano Energy* **2020**, *71*, 104609; c) D. Zou, D. Wang, Z. Chu, Z. Lv, X. Fan, *Coord. Chem. Rev.* **2010**, *254*, 1169.
- [43] A. Fakharuddin, M. Vasilopoulou, A. Soultati, M. I. Haider, J. Briscoe, V. Fotopoulos, D. Di Girolamo, D. Davazoglou, A. Chronos, A. R. b. M. Yusoff, A. Abate, L. Schmidt-Mende, M. K. Nazeeruddin, *Sol. RRL* **2021**, *5*, 2000555.
- [44] M. Ebner, R. Schennach, H.-T. Chien, C. Mayrhofer, A. Zankel, B. Friedel, *Flexible Printed Electron.* **2017**, *2*, 014002.
- [45] Z. Zhang, Z. Yang, J. Deng, Y. Zhang, G. Guan, H. Peng, *Small* **2015**, *11*, 675.
- [46] Z. Zhang, Z. Yang, Z. Wu, G. Guan, S. Pan, Y. Zhang, H. Li, J. Deng, B. Sun, H. Peng, *Adv. Energy Mater.* **2014**, *4*, 1301750.
- [47] R. E. A. Ardhi, M. X. Tran, M. Wang, G. Liu, J. K. Lee, *J. Mater. Chem. A* **2020**, *8*, 2549.
- [48] a) F. Cai, T. Chen, H. Peng, *J. Mater. Chem.* **2012**, *22*, 14856; b) T. Chen, L. Qiu, Z. Cai, F. Gong, Z. Yang, Z. Wang, H. Peng, *Nano Lett.* **2012**, *12*, 2568; c) S. Pan, Z. Yang, H. Li, L. Qiu, H. Sun, H. Peng, *J. Am. Chem. Soc.* **2013**, *135*, 10622; d) S. Zhang, C. Ji, Z. Bian, P. Yu, L. Zhang, D. Liu, E. Shi, Y. Shang, H. Peng, Q. Cheng, D. Wang, C. Huang, A. Cao, *ACS Nano* **2012**, *6*, 7191.
- [49] S. Casadio, N. Sangiorgi, A. Sangiorgi, A. Dessi, L. Zani, M. Calamante, G. Reginato, A. Mordini, A. Sanson, *Sol. Energy Mater. Sol. Cells* **2021**, *224*, 110986.
- [50] X. Fu, H. Sun, S. Xie, J. Zhang, Z. Pan, M. Liao, L. Xu, Z. Li, B. Wang, X. Sun, H. Peng, *J. Mater. Chem. A* **2018**, *6*, 45.
- [51] X. Y. Gu, E. Z. Chen, M. Y. Ma, Z. Y. Yang, J. L. Bai, L. L. Chen, G. Z. Sun, Z. X. Zhang, X. J. Pan, J. Y. Zhou, E. Q. Xie, *J. Phys. D: Appl. Phys.* **2019**, *52*, 095502.
- [52] X. Y. Gu, E. Z. Chen, K. Wei, L. L. Chen, C. Y. Zhang, G. W. Sun, J. R. Tan, H.-S. Bi, H. Xie, G. Z. Sun, X. Gao, X. J. Pan, J. Y. Zhou, *Appl. Phys. Lett.* **2021**, *118*, 053102.
- [53] J. H. Kim, S. K. Hong, S.-J. Yoo, C. Y. Woo, J. W. Choi, D. Lee, J.-W. Kang, H. W. Lee, M. Song, *Dyes Pigm.* **2021**, *185*, 108855.
- [54] J. H. Kim, S.-J. Yoo, D. Lee, J. W. Choi, S.-C. Han, T. I. Ryu, H. W. Lee, M. Shin, M. Song, *Nano Res.* **2021**, <https://link.springer.com/article/10.1007/s12274-020-3278-7>.
- [55] a) A. Monreal-Bernal, J. J. Vilatela, R. D. Costa, *Carbon* **2019**, *141*, 488; b) X. Pu, W. Song, M. Liu, C. Sun, C. Du, C. Jiang, X. Huang, D. Zou, W. Hu, Z. L. Wang, *Adv. Energy Mater.* **2016**, *6*, 1601048.
- [56] H. Sun, H. Li, X. You, Z. Yang, J. Deng, L. Qiu, H. Peng, *J. Mater. Chem. A* **2014**, *2*, 345.
- [57] B. C. Xiao, L. Y. Lin, *J. Colloid Interface Sci.* **2020**, *571*, 126.
- [58] J. Yan, M. J. Uddin, T. J. Dickens, D. E. Daramola, O. I. Okoli, *Adv. Mater. Interfaces* **2014**, *1*, 1400075.
- [59] J. Zhang, Z. Wang, X. Li, J. Yang, C. Song, Y. Li, J. Cheng, Q. Guan, B. Wang, *ACS Appl. Energy Mater.* **2019**, *2*, 2870.
- [60] A. Balilonda, Q. Li, M. Tebyetekerwa, R. Tusiime, H. Zhang, R. Jose, F. Zabihi, S. Yang, S. Ramakrishna, M. Zhu, *Adv. Fiber Mater.* **2019**, *1*, 101.
- [61] B. Dong, J. Hu, X. Xiao, S. Tang, X. Gao, Z. Peng, D. Zou, *Adv. Mater. Technol.* **2019**, *4*, 1900131.
- [62] a) A. M. Elseman, C. Xu, Y. Yao, M. Elisabeth, L. Niu, L. Malavasi, Q. L. Song, *Sol. RRL* **2020**, *4*, 2000136; b) H. Hu, K. Yan, M. Peng, X. Yu, S. Chen, B. Chen, B. Dong, X. Gao, D. Zou, *J. Mater. Chem. A* **2016**, *4*, 3901; c) J. Liu, L. Zhu, S. Xiang, Y. Wei, M. Xie, H. Liu, W. Li, H. Chen, *Sustainable Energy Fuels* **2019**, *3*, 184; d) L. Song,

- M. A. Niedermeier, V. Körstgens, F. C. Löhner, Y. Chen, S. V. Roth, P. Müller-Buschbaum, *ACS Appl. Nano Mater.* **2020**, *3*, 5987.
- [63] H. Hu, B. Dong, B. Chen, X. Gao, D. Zou, *Sustainable Energy Fuels* **2018**, *2*, 79.
- [64] Q. Li, A. Balilonda, A. Ali, R. Jose, F. Zabihi, S. Yang, S. Ramakrishna, M. Zhu, *Sol. RRL* **2020**, *4*, 2000269.
- [65] L. Qiu, S. He, J. Yang, J. Deng, H. Peng, *Small* **2016**, *12*, 2419.
- [66] L. Xu, X. Fu, F. Liu, X. Shi, X. Zhou, M. Liao, C. Chen, F. Xu, B. Wang, B. Zhang, H. Peng, *J. Mater. Chem. A* **2020**, *8*, 5476.
- [67] a) D. W. Chang, H.-J. Choi, A. Filer, J.-B. Baek, *J. Mater. Chem. A* **2014**, *2*, 640; b) J. Gong, J. Liang, K. Sumathy, *Renewable Sustainable Energy Rev.* **2012**, *16*, 5848.
- [68] M. L. Rosenbluth, N. S. Lewis, *J. Phys. Chem.* **1989**, *93*, 3735.
- [69] a) P. R. H. Nightingale, M. Deshpande, *Int. J. Innovative Technol. Explor. Eng.* **2019**, *9*, 4956; b) A. Aslam, U. Mehmood, M. H. Arshad, A. Ishfaq, J. Zaheer, A. Ul Haq Khan, M. Sufyan, *Sol. Energy* **2020**, *207*, 874; c) P. Poulouse, P. Sreejaya, in 2018 Int. CET Conf. on Control, Communication, and Computing (IC4), IEEE, Piscataway, NJ **2018**, pp. 152–156.
- [70] a) J. R. Jennings, A. Ghicov, L. M. Peter, P. Schmuki, A. B. Walker, *J. Am. Chem. Soc.* **2008**, *130*, 13364; b) P. Roy, D. Kim, K. Lee, E. Spiecker, P. Schmuki, *Nanoscale* **2010**, *2*, 45; c) J. Wu, Z. Lan, J. Lin, M. Huang, Y. Huang, L. Fan, G. Luo, *Chem. Rev.* **2015**, *115*, 2136.
- [71] a) P. Joshi, L. Zhang, D. Davoux, Z. Zhu, D. Galipeau, H. Fong, Q. Qiao, *Energy Environ. Sci.* **2010**, *3*, 1507; b) D. Maheswari, D. Sreenivasan, *Appl. Solar Energy* **2015**, *51*, 112; c) A. Taleb, F. Mesguich, A. Hérisson, C. Colbeau-Justin, X. Yanpeng, P. Dubot, *Sol. Energy Mater. Sol. Cells* **2016**, *148*, 52.
- [72] X. He, Y. Guo, X. Li, J. Liu, *Chem. Eng. J.* **2020**, *396*, 125302.
- [73] T. Chen, L. Qiu, H. Li, H. Peng, *J. Mater. Chem.* **2012**, *22*, 23655.
- [74] D. Liu, Y. Li, S. Zhao, A. Cao, C. Zhang, Z. Liu, Z. Bian, Z. Liu, C. Huang, *RSC Adv.* **2013**, *3*, 13720.
- [75] Y. Bai, H. Yu, Z. Li, R. Amal, G. Q. Lu, L. Wang, *Adv. Mater.* **2012**, *24*, 5850.
- [76] S. Jiao, Z. Sun, J. Wen, Y. Liu, F. Li, Q. Miao, W. Wu, L. Li, Y. Zhou, *ACS Appl. Mater. Interfaces* **2020**, *12*, 48794.
- [77] K. Sharma, V. Sharma, S. S. Sharma, *Nanoscale Res. Lett.* **2018**, *13*, 381.
- [78] a) A. Porfarzollah, R. Mohammad-Rezaei, M. Bagheri, *J. Mater. Sci.: Mater. Electron.* **2019**, *31*, 2288; b) A. Scalia, F. Bella, A. Lamberti, C. Gerbaldi, E. Tresso, *Energy* **2019**, *166*, 789.
- [79] a) N. Gasparini, A. Salleo, I. McCulloch, D. Baran, *Nat. Rev. Mater.* **2019**, *4*, 229; b) A. Wadsworth, Z. Hamid, J. Kosco, N. Gasparini, I. McCulloch, *Adv. Mater.* **2020**, *32*, 2001763.
- [80] P. R. Berger, M. Kim, *J. Renewable Sustainable Energy* **2018**, *10*, 013508.
- [81] M. R. Lee, R. D. Eckert, K. Forberich, G. Dennler, C. J. Brabec, R. A. Gaudiana, *Science* **2009**, *324*, 232.
- [82] a) N. Gasparini, A. Wadsworth, M. Moser, D. Baran, I. McCulloch, C. J. Brabec, *Adv. Energy Mater.* **2018**, *8*, 1703298; b) J. Hou, O. Ingnas, R. H. Friend, F. Gao, *Nat. Mater.* **2018**, *17*, 119; c) A. Wadsworth, M. Moser, A. Marks, M. S. Little, N. Gasparini, C. J. Brabec, D. Baran, I. McCulloch, *Chem. Soc. Rev.* **2019**, *48*, 1596.
- [83] S. Savagatrup, A. D. Printz, T. F. O'Connor, A. V. Zaretski, D. Rodriguez, E. J. Sawyer, K. M. Rajan, R. I. Acosta, S. E. Root, D. J. Lipomi, *Energy Environ. Sci.* **2015**, *8*, 55.
- [84] a) K. Wang, Z. Jin, L. Liang, H. Bian, D. Bai, H. Wang, J. Zhang, Q. Wang, S. Liu, *Nat. Commun.* **2018**, *9*, 4544; b) K. L. Wang, R. Wang, Z. K. Wang, M. Li, Y. Zhang, H. Ma, L. S. Liao, Y. Yang, *Nano Lett.* **2019**, *19*, 5176; c) Y. Wang, T. Zhang, M. Kan, Y. Zhao, *J. Am. Chem. Soc.* **2018**, *140*, 12345; d) X. Yang, H. Yang, X. Hu, W. Li, Z. Fang, K. Zhang, R. Huang, J. Li, Z. Yang, Y. Song, *J. Mater. Chem. A* **2020**, *8*, 5308.
- [85] W.-J. Yin, J.-H. Yang, J. Kang, Y. Yan, S.-H. Wei, *J. Mater. Chem. A* **2015**, *3*, 8926.
- [86] a) P. Gao, M. Grätzel, M. K. Nazeeruddin, *Energy Environ. Sci.* **2014**, *7*, 2448; b) G. Xing, N. Mathews, S. Sun, S. S. Lim, Y. M. Lam, M. Grätzel, S. Mhaisalkar, T. C. Sum, *Science* **2013**, *342*, 344; c) J. S. Yun, A. Ho-Baillie, S. Huang, S. H. Woo, Y. Heo, J. Seidel, F. Huang, Y. B. Cheng, M. A. Green, *J. Phys. Chem. Lett.* **2015**, *6*, 875.
- [87] A. Balilonda, Q. Li, X. Bian, R. Jose, S. Ramakrishna, M. Zhu, F. Zabihi, S. Yang, *Chem. Eng. J.* **2021**, *410*, 128384.
- [88] J. A. Sichert, Y. Tong, N. Mutz, M. Vollmer, S. Fischer, K. Z. Milowska, R. Garcia Cortadella, B. Nickel, C. Cardenas-Daw, J. K. Stolarczyk, A. S. Urban, J. Feldmann, *Nano Lett.* **2015**, *15*, 6521.
- [89] J. Deng, L. Qiu, X. Lu, Z. Yang, G. Guan, Z. Zhang, H. Peng, *J. Mater. Chem. A* **2015**, *3*, 21070.
- [90] a) J. S. Heo, J. Eom, Y. H. Kim, S. K. Park, *Small* **2018**, *14*, 1703034; b) J. Lee, S. Jeon, H. Seo, J. T. Lee, S. Park, *Appl. Sci.* **2021**, *11*, 531.
- [91] L. Wang, X. Fu, J. He, X. Shi, T. Chen, P. Chen, B. Wang, H. Peng, *Adv. Mater.* **2020**, *32*, 1901971.
- [92] F. C. Krebs, *Sol. Energy Mater. Sol. Cells* **2009**, *93*, 394.
- [93] V. Annapureddy, H. Palneedi, G.-T. Hwang, M. Peddigari, D.-Y. Jeong, W.-H. Yoon, K.-H. Kim, J. Ryu, *Sustainable Energy Fuels* **2017**, *1*, 2039.
- [94] X. F. Zheng, C. X. Liu, Y. Y. Yan, Q. Wang, *Renewable Sustainable Energy Rev.* **2014**, *32*, 486.
- [95] G. Centi, G. Iaquaniello, S. Perathoner, *BMC Chem. Eng.* **2019**, *1*, 5.
- [96] S. Sripadmanabhan Indira, C. Aravind Vaithilingam, K. S. P. Oruganti, F. Mohd, S. Rahman, *Nanomaterials* **2019**, *9*, 773.
- [97] H. Xue, Q. Yang, D. Wang, W. Luo, W. Wang, M. Lin, D. Liang, Q. Luo, *Nano Energy* **2017**, *38*, 147.
- [98] J. Briscoe, S. Dunn, *Nano Energy* **2015**, *14*, 15.
- [99] G. Zhu, B. Peng, J. Chen, Q. Jing, Z. L. Wang, *Nano Energy* **2015**, *14*, 126.
- [100] Z. Wen, M.-H. Yeh, H. Guo, J. Wang, Y. Zi, W. Xu, J. Deng, L. Zhu, X. Wang, C. Hu, L. Zhu, X. Sun, Z. L. Wang, *Sci. Adv.* **2016**, *2*, e1600097.
- [101] Y. Qin, X. Wang, Z. L. Wang, *Nature* **2008**, *451*, 809.
- [102] Q. Liao, Z. Zhang, X. Zhang, M. Mohr, Y. Zhang, H.-J. Fecht, *Nano Res.* **2014**, *7*, 917.
- [103] L. Zhang, S. Bai, C. Su, Y. Zheng, Y. Qin, C. Xu, Z. L. Wang, *Adv. Funct. Mater.* **2015**, *25*, 5794.
- [104] S. Egusa, Z. Wang, N. Chocat, Z. M. Ruff, A. M. Stolyarov, D. Shemuly, F. Sorin, P. T. Rakich, J. D. Joannopoulos, Y. Fink, *Nat. Mater.* **2010**, *9*, 643.
- [105] H. J. Sim, C. Choi, C. J. Lee, Y. T. Kim, G. M. Spinks, M. D. Lima, R. H. Baughman, S. J. Kim, *Adv. Eng. Mater.* **2015**, *17*, 1270.
- [106] M. Baniasadi, J. Huang, Z. Xu, S. Moreno, X. Yang, J. Chang, M. A. Quevedo-Lopez, M. Naraghi, M. Minary-Jolandan, *ACS Appl. Mater. Interfaces* **2015**, *7*, 5358.
- [107] Y. B. Lee, J. K. Han, S. Noothongkaew, S. K. Kim, W. Song, S. Myung, S. S. Lee, J. Lim, S. D. Bu, K.-S. An, *Adv. Mater.* **2017**, *29*, 1604500.
- [108] A. Lund, K. Rundqvist, E. Nilsson, L. Yu, B. Hagström, C. Müller, *npj Flexible Electron.* **2018**, *2*, 9.
- [109] H. Gao, P. T. Minh, H. Wang, S. Minko, J. Locklin, T. Nguyen, S. Sharma, *Smart Mater. Struct.* **2018**, *27*, 095018.
- [110] F. Mokhtari, J. Foroughi, T. Zheng, Z. Cheng, G. M. Spinks, *J. Mater. Chem. A* **2019**, *7*, 8245.
- [111] A. Forouzan, M. Yousefzadeh, M. Latifi, R. Jose, *Macromol. Mater. Eng.* **2021**, *306*, 2000510.
- [112] K. Dong, Y.-C. Wang, J. Deng, Y. Dai, S. L. Zhang, H. Zou, B. Gu, B. Sun, Z. L. Wang, *ACS Nano* **2017**, *11*, 9490.
- [113] M. Liu, Z. Cong, X. Pu, W. Guo, T. Liu, M. Li, Y. Zhang, W. Hu, Z. L. Wang, *Adv. Funct. Mater.* **2019**, *29*, 1806298.

- [114] M. Zhang, M. Zhao, M. Jian, C. Wang, A. Yu, Z. Yin, X. Liang, H. Wang, K. Xia, X. Liang, J. Zhai, Y. Zhang, *Matter* **2019**, *1*, 168.
- [115] Y. Yang, L. Xie, Z. Wen, C. Chen, X. Chen, A. Wei, P. Cheng, X. Xie, X. Sun, *ACS Appl. Mater. Interfaces* **2018**, *10*, 42356.
- [116] J. Park, D. Kim, A. Y. Choi, Y. T. Kim, *APL Mater.* **2018**, *6*, 101106.
- [117] W. Gong, C. Hou, J. Zhou, Y. Guo, W. Zhang, Y. Li, Q. Zhang, H. Wang, *Nat. Commun.* **2019**, *10*, 868.
- [118] L. Xie, X. Chen, Z. Wen, Y. Yang, J. Shi, C. Chen, M. Peng, Y. Liu, X. Sun, *Nano-Micro Lett.* **2019**, *11*, 39.
- [119] J. Liu, N. Cui, T. Du, G. Li, S. Liu, Q. Xu, Z. Wang, L. Gu, Y. Qin, *Nanoscale Adv.* **2020**, *2*, 4482.
- [120] Z. Lin, Q. He, Y. Xiao, T. Zhu, J. Yang, C. Sun, Z. Zhou, H. Zhang, Z. Shen, J. Yang, Z. L. Wang, *Adv. Mater. Technol.* **2018**, *3*, 1800144.
- [121] Y. Yang, N. Sun, Z. Wen, P. Cheng, H. Zheng, H. Shao, Y. Xia, C. Chen, H. Lan, X. Xie, C. Zhou, J. Zhong, X. Sun, S.-T. Lee, *ACS Nano* **2018**, *12*, 2027.
- [122] T. Jing, B. Xu, Y. Yang, *Nano Energy* **2021**, *84*, 105867.
- [123] X. He, Y. Zi, H. Guo, H. Zheng, Y. Xi, C. Wu, J. Wang, W. Zhang, C. Lu, Z. L. Wang, *Adv. Funct. Mater.* **2017**, *27*, 1604378.
- [124] Y. Cheng, X. Lu, K. Hoe Chan, R. Wang, Z. Cao, J. Sun, G. Wei Ho, *Nano Energy* **2017**, *41*, 511.
- [125] H. J. Sim, C. Choi, S. H. Kim, K. M. Kim, C. J. Lee, Y. T. Kim, X. Lepró, R. H. Baughman, S. J. Kim, *Sci. Rep.* **2016**, *6*, 35153.
- [126] Z. Tian, J. He, X. Chen, T. Wen, C. Zhai, Z. Zhang, J. Cho, X. Chou, C. Xue, *RSC Adv.* **2018**, *8*, 2950.
- [127] C. Ning, K. Dong, R. Cheng, J. Yi, C. Ye, X. Peng, F. Sheng, Y. Jiang, Z. L. Wang, *Adv. Funct. Mater.* **2021**, *31*, 2006679.
- [128] T. Zhao, J. Li, H. Zeng, Y. Fu, H. He, L. Xing, Y. Zhang, X. Xue, *Nanotechnology* **2018**, *29*, 405504.
- [129] K. Dong, J. Deng, W. Ding, A. C. Wang, P. Wang, C. Cheng, Y.-C. Wang, L. Jin, B. Gu, B. Sun, Z. L. Wang, *Adv. Energy Mater.* **2018**, *8*, 1801114.
- [130] D. Kim, J. Park, Y. T. Kim, *ACS Appl. Energy Mater.* **2019**, *2*, 1357.
- [131] S. Balasubramaniam, A. Mohanty, S. K. Balasingam, S. J. Kim, A. Ramadoss, *Nano-Micro Lett.* **2020**, *12*, 85.
- [132] Y. Zhang, X. Zhang, K. Yang, X. Fan, Y. Tong, Z. Zhang, X. Lu, K. Mai, Q. Ni, M. Zhang, X. Chen, *J. Mater. Chem. A* **2018**, *6*, 12250.
- [133] J. Guo, Q. Zhang, J. Sun, C. Li, J. Zhao, Z. Zhou, B. He, X. Wang, P. Man, Q. Li, J. Zhang, L. Xie, M. Li, Y. Yao, *J. Power Sources* **2018**, *382*, 122.
- [134] Z. Wang, J. Cheng, Q. Guan, H. Huang, Y. Li, J. Zhou, W. Ni, B. Wang, S. He, H. Peng, *Nano Energy* **2018**, *45*, 210.
- [135] S. Cho, B. Patil, S. Yu, S. Ahn, J. Hwang, C. Park, K. Do, H. Ahn, *Electrochim. Acta* **2018**, *269*, 499.
- [136] a) Z. Xu, L. Peng, Y. Liu, Z. Liu, H. Sun, W. Gao, C. Gao, *Chem. Mater.* **2017**, *29*, 319; b) K.-E. Kim, B.-K. Jang, Y. Heo, J. H. Lee, M. Jeong, J. Y. Lee, J. Seidel, C.-H. Yang, *NPG Asia Mater.* **2014**, *6*, e81; c) Z. Xu, C. Gao, *Mater. Today* **2015**, *18*, 480.
- [137] a) W. Ma, S. Chen, S. Yang, M. Zhu, *RSC Adv.* **2016**, *6*, 50112; b) D. Yu, K. Goh, H. Wang, L. Wei, W. Jiang, Q. Zhang, L. Dai, Y. Chen, *Nat. Nanotechnol.* **2014**, *9*, 555.
- [138] X. Zheng, K. Zhang, L. Yao, Y. Qiu, S. Wang, *J. Mater. Chem. A* **2018**, *6*, 896.
- [139] C. Lu, J. Meng, J. Zhang, X. Chen, M. Du, Y. Chen, C. Hou, J. Wang, A. Ju, X. Wang, Y. Qiu, S. Wang, K. Zhang, *ACS Appl. Mater. Interfaces* **2019**, *11*, 31573.
- [140] W. Gong, B. Fugetsu, Z. Wang, T. Ueki, I. Sakata, H. Ogata, F. Han, M. Li, L. Su, X. Zhang, M. Terrones, M. Endo, *Carbon* **2019**, *154*, 169.
- [141] S. Liu, C. Xu, H. Yang, G. Qian, S. Hua, J. Liu, X. Zheng, X. Lu, *Small* **2020**, *16*, 1905778.
- [142] a) F. Jonas, W. Krafft, B. Muys, *Macromol. Symp.* **1995**, *100*, 169; b) G. Cai, P. Darmawan, M. Cui, J. Wang, J. Chen, S. Magdassi, P. S. Lee, *Adv. Energy Mater.* **2016**, *6*, 1501882.
- [143] a) R. Jalili, J. M. Razal, P. C. Innis, G. G. Wallace, *Adv. Funct. Mater.* **2011**, *21*, 3363; b) H. Okuzaki, M. Ishihara, *Macromol. Rapid Commun.* **2003**, *24*, 261.
- [144] B. Li, J. Cheng, Z. Wang, Y. Li, W. Ni, B. Wang, *J. Power Sources* **2018**, *376*, 117.
- [145] a) C. Li, H. Bai, G. Shi, *Chem. Soc. Rev.* **2009**, *38*, 2397; b) Y. Zhao, Y. Ding, Y. Li, L. Peng, H. R. Byon, J. B. Goodenough, G. Yu, *Chem. Soc. Rev.* **2015**, *44*, 7968.
- [146] M. Serrapede, A. Rafique, M. Fontana, A. Zine, P. Rivolo, S. Bianco, L. Chetibi, E. Tresso, A. Lamberti, *Carbon* **2019**, *144*, 91.
- [147] N. He, S. Patil, J. Qu, J. Liao, F. Zhao, W. Gao, *ACS Appl. Energy Mater.* **2020**, *3*, 2949.
- [148] C. Meng, Y. Qian, J. He, X. Dong, *J. Mater. Sci.: Mater. Electron.* **2020**, *31*, 19293.
- [149] P. Song, J. Tao, X. He, Y. Sun, X. Shen, L. Zhai, A. Yuan, D. Zhang, Z. Ji, B. Li, *Chem. Eng. J.* **2020**, *386*, 124024.
- [150] Z. Wang, F. Cao, K. Chen, Y. Yan, Y. Chen, Y. Zhang, X. Zhu, B. Wei, Y. Xiong, Z. Lv, *ChemSusChem* **2018**, *11*, 985.
- [151] J. Qi, X. Liu, Y. Sui, Y. He, Y. Ren, Q. Meng, F. Wei, X. Zhang, *J. Mater. Sci.: Mater. Electron.* **2019**, *30*, 667.
- [152] L. Gao, R. Fan, R. Xiao, K. Cao, P. Li, W. Wang, Y. Lu, *Appl. Surf. Sci.* **2019**, *475*, 1058.
- [153] S. Shahrokhian, L. Naderi, R. Mohammadi, *ACS Sustainable Chem. Eng.* **2018**, *6*, 14574.
- [154] Y. Zhang, R. Lin, Y. Fu, X. Wang, X. Yu, J. Li, Y. Zhu, S. Tan, Z. Wang, *Mater. Lett.* **2018**, *228*, 9.
- [155] T. S. Le, T. K. Truong, V. N. Huynh, J. Bae, D. Suh, *Nano Energy* **2020**, *67*, 104198.
- [156] C. Li, Z. Wang, S. Li, J. Cheng, Y. Zhang, J. Zhou, D. Yang, D.-G. Tong, B. Wang, *ACS Appl. Mater. Interfaces* **2018**, *10*, 18390.
- [157] X. Li, X. Li, J. Cheng, D. Yuan, W. Ni, Q. Guan, L. Gao, B. Wang, *Nano Energy* **2016**, *21*, 228.
- [158] J. Ni, S. Fu, C. Wu, J. Maier, Y. Yu, L. Li, *Adv. Mater.* **2016**, *28*, 2259.
- [159] Z. Wang, J. Cheng, J. Zhou, J. Zhang, H. Huang, J. Yang, Y. Li, B. Wang, *Nano Energy* **2018**, *50*, 106.
- [160] M. He, K. Fic, E. Frćkowiak, P. Novák, E. J. Berg, *Energy Environ. Sci.* **2016**, *9*, 623.
- [161] a) D. Wang, S. Liu, L. Jiao, G. Fang, G. Geng, J. Ma, *Carbon* **2017**, *119*, 30; b) G. Xiong, P. He, B. Huang, T. Chen, Z. Bo, T. S. Fisher, *Nano Energy* **2017**, *38*, 127.
- [162] Q. Liu, J. Zhou, C. Song, X. Li, Z. Wang, J. Yang, J. Cheng, H. Li, B. Wang, *Energy Storage Mater.* **2020**, *24*, 495.
- [163] B. Wang, X. Fang, H. Sun, S. He, J. Ren, Y. Zhang, H. Peng, *Adv. Mater.* **2015**, *27*, 7854.
- [164] S. Pan, J. Ren, X. Fang, H. Peng, *Adv. Energy Mater.* **2016**, *6*, 1501867.
- [165] J. Sun, P. Man, Q. Zhang, B. He, Z. Zhou, C. Li, X. Wang, J. Guo, J. Zhao, L. Xie, Q. Li, J. Sun, G. Hong, Y. Yao, *Appl. Surf. Sci.* **2018**, *447*, 795.
- [166] X. Wang, Q. Zhang, J. Sun, Z. Zhou, Q. Li, B. He, J. Zhao, W. Lu, C.-p. Wong, Y. Yao, *J. Mater. Chem. A* **2018**, *6*, 8030.
- [167] X. Wang, J. Sun, J. Zhao, Z. Zhou, Q. Zhang, C.-p. Wong, Y. Yao, *J. Phys. Chem. C* **2019**, *123*, 985.
- [168] M. Mo, C. Chen, H. Gao, M. Chen, D. Li, *Electrochim. Acta* **2018**, *269*, 11.
- [169] a) S. Bandyopadhyay, C. Singh, P. Jash, M. D. W. Hussain, A. Paul, A. Patra, *Chem. Commun.* **2018**, *54*, 6796; b) H. Li, J. Li, A. Thomas, Y. Liao, *Adv. Funct. Mater.* **2019**, *29*, 1904785.
- [170] a) X.-C. Li, Y. Zhang, C.-Y. Wang, Y. Wan, W.-Y. Lai, H. Pang, W. Huang, *Chem. Sci.* **2017**, *8*, 2959; b) H. Zhang, Y. Zhang, C. Gu, Y. Ma, *Adv. Energy Mater.* **2015**, *5*, 1402175.
- [171] W. Lyu, W. Zhang, H. Liu, Y. Liu, H. Zuo, C. Yan, C. F. J. Faul, A. Thomas, M. Zhu, Y. Liao, *Chem. Mater.* **2020**, *32*, 8276.

- [172] X. Cheng, Z. Pan, J. Yang, Y. Zhong, X. Wang, C. Ye, J. Zhuang, Q. Huang, Q. Yongcai, W. Li, *J. Power Sources* **2019**, 427, 243.
- [173] J. Zhang, X. Liu, Q. Yin, Y. Zhao, J. Luo, J. Han, *ACS Omega* **2019**, 4, 11863.
- [174] Z. Zhang, D. Zhang, H. Lin, Y. Chen, *J. Power Sources* **2019**, 433, 226711.
- [175] A. Mohanty, D. Jaihindh, Y.-P. Fu, S. P. Senanayak, L. S. Mende, A. Ramadoss, *J. Power Sources* **2021**, 488, 229444.
- [176] a) Y. Gogotsi, B. Anasori, *ACS Nano* **2019**, 13, 8491; b) M. Shao, R. Zhang, Z. Li, M. Wei, D. G. Evans, X. Duan, *Chem. Commun.* **2015**, 51, 15880.
- [177] Z. Zhou, Q. Zhang, J. Sun, B. He, J. Guo, Q. Li, C. Li, L. Xie, Y. Yao, *ACS Nano* **2018**, 12, 9333.
- [178] Y. Ba, S. Zhou, S. Jiao, W. Pan, *J. Appl. Polym. Sci.* **2018**, 135, 46769.
- [179] M. Gorjanc, M. Mozetič, G. Primc, A. Vesel, K. Spasić, N. Puač, Z. L. Petrović, M. Kert, *Appl. Surf. Sci.* **2017**, 419, 224.
- [180] X. Zheng, L. Yao, Y. Qiu, S. Wang, K. Zhang, *ACS Appl. Energy Mater.* **2019**, 2, 4335.
- [181] Y. Zhao, D. Dong, Y. Wang, S. Gong, T. An, L. W. Yap, W. Cheng, *ACS Appl. Mater. Interfaces* **2018**, 10, 42612.
- [182] X. Gao, X. Xiao, B. Dong, J. Hu, S. Tang, W. Qi, D. Zou, *ChemistrySelect* **2019**, 4, 5355.
- [183] C. Liu, Q. Li, Q. Zhang, B. He, P. Man, Z. Zhou, C. Li, L. Xie, Y. Yao, *Electrochim. Acta* **2020**, 330, 135247.
- [184] a) Y. Zhang, W. Bai, X. Cheng, J. Ren, W. Weng, P. Chen, X. Fang, Z. Zhang, H. Peng, *Angew. Chem., Int. Ed.* **2014**, 53, 14564; b) N. S. Hudak, A. D. Schlichting, K. Eisenbeiser, *J. Electrochem. Soc.* **2017**, 164, A691.
- [185] B. Patil, S. Ahn, S. Yu, H. Song, Y. Jeong, J. H. Kim, H. Ahn, *Carbon* **2018**, 134, 366.
- [186] a) H. Li, Y. Gao, C. Wang, G. Yang, *Adv. Energy Mater.* **2015**, 5, 1401767; b) J. Kang, A. Hirata, L. Chen, S. Zhu, T. Fujita, M. Chen, *Angew. Chem., Int. Ed.* **2015**, 54, 8100.
- [187] X. Cao, Y. Liu, Y. Zhong, L. Cui, A. Zhang, J. M. Razal, W. Yang, J. Liu, *J. Mater. Chem. A* **2020**, 8, 1837.
- [188] J. Zhao, L. Li, Y. Zhang, C. Li, Q. Zhang, J. Peng, X. Zhao, Q. Li, X. Wang, J. Xie, J. Sun, B. He, C. Lu, W. Lu, T. Zhang, Y. Yao, *Energy Storage Mater.* **2018**, 15, 315.
- [189] S. Yu, B. Patil, H. Ahn, *Fibers Polym.* **2020**, 21, 465.
- [190] a) Q. Wang, X. Wang, J. Xu, X. Ouyang, X. Hou, D. Chen, R. Wang, G. Shen, *Nano Energy* **2014**, 8, 44; b) X. Chen, L. Qiu, J. Ren, G. Guan, H. Lin, Z. Zhang, P. Chen, Y. Wang, H. Peng, *Adv. Mater.* **2013**, 25, 6436; c) Y. Meng, Y. Zhao, C. Hu, H. Cheng, Y. Hu, Z. Zhang, G. Shi, L. Qu, *Adv. Mater.* **2013**, 25, 2326; d) J. Tao, N. Liu, W. Ma, L. Ding, L. Li, J. Su, Y. Gao, *Sci. Rep.* **2013**, 3, 2286; e) C. Choi, S. H. Kim, H. J. Sim, J. A. Lee, A. Y. Choi, Y. T. Kim, X. Lepró, G. M. Spinks, R. H. Baughman, S. J. Kim, *Sci. Rep.* **2015**, 5, 9387; f) J. Bae, M. K. Song, Y. J. Park, J. M. Kim, M. Liu, Z. L. Wang, *Angew. Chem., Int. Ed.* **2011**, 50, 1683.
- [191] S. Yu, B. Patil, H. Ahn, *J. Ind. Eng. Chem.* **2019**, 71, 220.
- [192] a) A. Burke, *J. Power Sources* **2000**, 91, 37; b) R. Kötz, M. Carlen, *Electrochim. Acta* **2000**, 45, 2483.
- [193] Z. Niu, L. Zhang, L. Liu, B. Zhu, H. Dong, X. Chen, *Adv. Mater.* **2013**, 25, 4035.
- [194] X. Wang, Z. Zhou, Z. Sun, J. Hah, Y. Yao, K.-S. Moon, J. Di, Q. Li, C.-p. Wong, *Nano-Micro Lett.* **2020**, 13, 4.
- [195] Z. Yang, Y. Jia, Y. Niu, Z. Yong, K. Wu, C. Zhang, M. Zhu, Y. Zhang, Q. Li, *Chem. Eng. J.* **2020**, 400, 125835.
- [196] H. Yuan, G. Wang, Y. Zhao, Y. Liu, Y. Wu, Y. Zhang, *Nano Res.* **2020**, 13, 1686.
- [197] a) Y. Hu, X. Sun, *J. Mater. Chem. A* **2014**, 2, 10712; b) G. Zhou, F. Li, H.-M. Cheng, *Energy Environ. Sci.* **2014**, 7, 1307; c) Z. Qi, H. Wang, *Research* **2020**, 2020, 2969510.
- [198] D. Yu, K. Goh, H. Wang, L. Wei, W. Jiang, Q. Zhang, L. Dai, Y. Chen, *Nat. Nanotechnol.* **2020**, 15, 811.
- [199] Y. Zhou, J. Fang, H. Wang, H. Zhou, G. Yan, Y. Zhao, L. Dai, T. Lin, *Adv. Electron. Mater.* **2018**, 4, 1800104.
- [200] Y. Zhou, Y. Zhao, J. Fang, T. Lin, *RSC Adv.* **2016**, 6, 110164.
- [201] Y. Fu, X. Cai, H. Wu, Z. Lv, S. Hou, M. Peng, X. Yu, D. Zou, *Adv. Mater.* **2012**, 24, 5713.
- [202] Z. Zhang, Z. Yang, Z. Wu, G. Guan, S. Pan, Y. Zhang, H. Li, J. Deng, B. Sun, H. Peng, *Adv. Energy Mater.* **2014**, 4, 1301750.
- [203] Y. Zhang, L. Wang, Z. Guo, Y. Xu, Y. Wang, H. Peng, *Angew. Chem., Int. Ed.* **2016**, 55, 4487.
- [204] X. Li, X. Chen, Z. Jin, P. Li, D. Xiao, *Mater. Chem. Front.* **2021**, 5, 1140.
- [205] a) H. Song, S.-Y. Jeon, Y. Jeong, *Carbon* **2019**, 147, 441; b) Q. Zhang, C. Li, Q. Li, Z. Pan, J. Sun, Z. Zhou, B. He, P. Man, L. Xie, L. Kang, X. Wang, J. Yang, T. Zhang, P. P. Shum, Q. Li, Y. Yao, L. Wei, *Nano Lett.* **2019**, 19, 4035.
- [206] S.-H. Park, W.-J. Lee, *RSC Adv.* **2015**, 5, 23548.
- [207] Y. Zhou, C.-H. Wang, W. Lu, L. Dai, *Adv. Mater.* **2020**, 32, 1902779.
- [208] Q. Meng, K. Wang, W. Guo, J. Fang, Z. Wei, X. She, *Small* **2014**, 10, 3187.
- [209] Y. Xu, Y. Zhang, Z. Guo, J. Ren, Y. Wang, H. Peng, *Angew. Chem., Int. Ed.* **2015**, 54, 15390.
- [210] Y. Huang, H. Hu, Y. Huang, M. Zhu, W. Meng, C. Liu, Z. Pei, C. Hao, Z. Wang, C. Zhi, *ACS Nano* **2015**, 9, 4766.
- [211] P. Li, Z. Jin, D. Xiao, *Energy Storage Mater.* **2018**, 12, 232.
- [212] Y. Zeng, Y. Meng, Z. Lai, X. Zhang, M. Yu, P. Fang, M. Wu, Y. Tong, X. Lu, *Adv. Mater.* **2017**, 29, 1702698.
- [213] a) C. Yi, X. Chen, F. Gou, C. M. Dmuchowski, A. Sharma, C. Park, C. Ke, *Carbon* **2017**, 125, 93; b) A. Takakura, K. Beppu, T. Nishihara, A. Fukui, T. Kozeki, T. Namazu, Y. Miyauchi, K. Itami, *Nat. Commun.* **2019**, 10, 3040.
- [214] a) D. Di Lecce, P. Andreotti, M. Boni, G. Gasparro, G. Rizzati, J.-Y. Hwang, Y.-K. Sun, J. Hassoun, *ACS Sustainable Chem. Eng.* **2018**, 6, 3225; b) A. C. Lim, H. S. Jadhav, H. J. Kwon, J. G. Seo, *ACS Omega* **2019**, 4, 4129.
- [215] H. Liang, W. Weng, J. Ren, L. Qiu, Z. Zhang, P. Chen, X. Chen, J. Deng, Y. Wang, H. Peng, *Adv. Mater.* **2014**, 26, 1217.
- [216] Z. Zhang, X. Han, L. Li, P. Su, W. Huang, J. Wang, J. Xu, C. Li, S. Chen, Y. Yang, *J. Power Sources* **2020**, 450, 227593.
- [217] J. Ren, Y. Zhang, W. Bai, X. Chen, Z. Zhang, X. Fang, W. Weng, Y. Wang, H. Peng, *Angew. Chem., Int. Ed.* **2014**, 53, 7864.
- [218] Y. Luo, Y. Zhang, Y. Zhao, X. Fang, J. Ren, W. Weng, Y. Jiang, H. Sun, B. Wang, X. Cheng, H. Peng, *J. Mater. Chem. A* **2015**, 3, 17553.
- [219] T. Hoshida, Y. Zheng, J. Hou, Z. Wang, Q. Li, Z. Zhao, R. Ma, T. Sasaki, F. Geng, *Nano Lett.* **2017**, 17, 3543.
- [220] Y. Zhang, Y. Wang, L. Wang, C.-M. Lo, Y. Zhao, Y. Jiao, G. Zheng, H. Peng, *J. Mater. Chem. A* **2016**, 4, 9002.
- [221] Z. Guo, Y. Zhao, Y. Ding, X. Dong, L. Chen, J. Cao, C. Wang, Y. Xia, H. Peng, Y. Wang, *Chem* **2017**, 3, 348.
- [222] Y. Huang, W. S. Ip, Y. Y. Lau, J. Sun, J. Zeng, N. S. S. Yeung, W. S. Ng, H. Li, Z. Pei, Q. Xue, Y. Wang, J. Yu, H. Hu, C. Zhi, *ACS Nano* **2017**, 11, 8953.
- [223] X. Lin, Q. Kang, Z. Zhang, R. Liu, Y. Li, Z. Huang, X. Feng, Y. Ma, W. Huang, *J. Mater. Chem. A* **2017**, 5, 3638.
- [224] Z. Jin, P. Li, Y. Jin, D. Xiao, *Energy Storage Mater.* **2018**, 13, 160.
- [225] Z. Pan, J. Yang, Y. Zhang, X. Gao, J. Wang, *J. Mater. Chem. A* **2020**, 8, 6406.
- [226] Q. Zhang, Z. Zhou, Z. Pan, J. Sun, B. He, Q. Li, T. Zhang, J. Zhao, L. Tang, Z. Zhang, L. Wei, Y. Yao, *Adv. Sci.* **2018**, 5, 1801462.
- [227] W. Weng, Q. Sun, Y. Zhang, H. Lin, J. Ren, X. Lu, M. Wang, H. Peng, *Nano Lett.* **2014**, 14, 3432.
- [228] R. Liu, Y. Liu, J. Chen, Q. Kang, L. Wang, W. Zhou, Z. Huang, X. Lin, Y. Li, P. Li, X. Feng, G. Wu, Y. Ma, W. Huang, *Nano Energy* **2017**, 33, 325.

- [229] Z. Wu, K. Liu, C. Lv, S. Zhong, Q. Wang, T. Liu, X. Liu, Y. Yin, Y. Hu, D. Wei, Z. Liu, *Small* **2018**, *14*, 1800414.
- [230] X. Qian, R. Qiu, C. Lu, Y. Qiu, Z. Wu, S. Wang, K. Zhang, *ACS Omega* **2020**, *5*, 4697.
- [231] Y. Zhang, Y. Jiao, L. Lu, L. Wang, T. Chen, H. Peng, *Angew. Chem., Int. Ed.* **2017**, *56*, 13741.
- [232] J. Zheng, G. Tan, P. Shan, T. Liu, J. Hu, Y. Feng, L. Yang, M. Zhang, Z. Chen, Y. Lin, J. Lu, J. C. Neuefeind, Y. Ren, K. Amine, L.-W. Wang, K. Xu, F. Pan, *Chem* **2018**, *4*, 2872.
- [233] a) M. Becker, R.-S. Kühnel, C. Battaglia, *Chem. Commun.* **2019**, 55, 12032; b) L. Chen, L. Cao, X. Ji, S. Hou, Q. Li, J. Chen, C. Yang, N. Eidson, C. Wang, *Nat. Commun.* **2020**, *11*, 2638.
- [234] V. L. Martins, R. M. Torresi, *Curr. Opin. Electrochem.* **2020**, *21*, 62.
- [235] a) P. B. Balbuena, *AIP Conf. Proc.* **2014**, *1597*, 82; b) E. Quartarone, P. Mustarelli, *J. Electrochem. Soc.* **2020**, *167*, 050508; c) R. Younesi, G. M. Veith, P. Johansson, K. Edström, T. Vegge, *Energy Environ. Sci.* **2015**, *8*, 1905.
- [236] a) E. R. Logan, J. R. Dahn, *Trends Chem.* **2020**, *2*, 354; b) L. Xia, L. Yu, D. Hu, G. Z. Chen, *Mater. Chem. Front.* **2017**, *1*, 584.
- [237] X. Mei, Y. Wu, Y. Gao, Y. Zhu, S.-H. Bo, Y. Guo, *Mater. Today Commun.* **2020**, *24*, 101004.
- [238] Y. Ye, L. Gong, S. Xiang, Z. Zhang, B. Chen, *Adv. Mater.* **2020**, *32*, 1907090.
- [239] C. Yuan, J. Li, P. Han, Y. Lai, Z. Zhang, J. Liu, *J. Power Sources* **2013**, *240*, 653.
- [240] a) N. Boaretto, L. Meabe, M. Martinez-Ibañez, M. Armand, H. Zhang, *J. Electrochem. Soc.* **2020**, *167*, 070524; b) X. Cheng, J. Pan, Y. Zhao, M. Liao, H. Peng, *Adv. Energy Mater.* **2018**, *8*, 1702184.
- [241] a) T. Chen, S. Chen, Y. Chen, M. Zhao, D. Losic, S. Zhang, *Mater. Chem. Front.* **2021**, *5*, 1771; b) A. E. Baumann, D. A. Burns, B. Liu, V. S. Thoi, *Commun. Chem.* **2019**, *2*, 86.
- [242] a) J. C. Bachman, S. Muy, A. Grimaud, H.-H. Chang, N. Pour, S. F. Lux, O. Paschos, F. Maglia, S. Lupart, P. Lamp, L. Giordano, Y. Shao-Horn, *Chem. Rev.* **2016**, *116*, 140; b) X. Miao, H. Wang, R. Sun, C. Wang, Z. Zhang, Z. Li, L. Yin, *Energy Environ. Sci.* **2020**, *13*, 3780.
- [243] a) Z. Wu, Z. Xie, J. Wang, T. Yu, X. Du, Z. Wang, X. Hao, A. Abudula, G. Guan, *Int. J. Hydrogen Energy* **2020**, *45*, 19601; b) H. Duan, M. Fan, W.-P. Chen, J.-Y. Li, P.-F. Wang, W.-P. Wang, J.-L. Shi, Y.-X. Yin, L.-J. Wan, Y.-G. Guo, *Adv. Mater.* **2019**, *31*, 1807789; c) Y. Xiao, Y. Wang, S.-H. Bo, J. C. Kim, L. J. Miarra, G. Ceder, *Nat. Rev. Mater.* **2020**, *5*, 105.
- [244] J. Zhou, T. Qian, J. Liu, M. Wang, L. Zhang, C. Yan, *Nano Lett.* **2019**, *19*, 3066.
- [245] W. Liu, N. Liu, J. Sun, P.-C. Hsu, Y. Li, H.-W. Lee, Y. Cui, *Nano Lett.* **2015**, *15*, 2740.
- [246] X. Zhao, C.-a. Tao, Y. Li, X. Chen, J. Wang, H. Gong, *Ionics* **2020**, *26*, 4299.
- [247] a) A. J. Nagajothi, R. Kannan, S. Rajashabala, *Ionics* **2018**, *24*, 1407; b) R. Arunkumar, R. S. Babu, M. Usha Rani, S. Rajendran, *Ionics* **2017**, *23*, 3097; c) G. Hirankumar, N. Mehta, *Heliyon* **2018**, *4*, e00992.
- [248] a) L. Li, M. Wang, J. Wang, F. Ye, S. Wang, Y. Xu, J. Liu, G. Xu, Y. Zhang, Y. Zhang, C. Yan, N. V. Medhekar, M. Liu, Y. Zhang, *J. Mater. Chem. A* **2020**, *8*, 8033; b) K. Deng, Q. Zeng, D. Wang, Z. Liu, Z. Qiu, Y. Zhang, M. Xiao, Y. Meng, *J. Mater. Chem. A* **2020**, *8*, 1557.
- [249] X. Fang, W. Weng, J. Ren, H. Peng, *Adv. Mater.* **2016**, *28*, 491.
- [250] H. Lee, K. Y. Lim, K.-B. Kim, J.-W. Yu, W. K. Choi, J.-W. Choi, *ACS Appl. Mater. Interfaces* **2020**, *12*, 11504.
- [251] C. Massaroni, P. Saccomandi, E. Schena, *J. Funct. Biomater.* **2015**, *6*, 204.
- [252] a) C. B. Cooper, K. Arutselvan, Y. Liu, D. Armstrong, Y. Lin, M. R. Khan, J. Genzer, M. D. Dickey, *Adv. Funct. Mater.* **2017**, *27*, 1605630; b) Y. Lu, J. Jiang, S. Yoon, K.-S. Kim, J.-H. Kim, S. Park, S.-H. Kim, L. Piao, *ACS Appl. Mater. Interfaces* **2018**, *10*, 2093; c) C. Choi, J. M. Lee, S. H. Kim, S. J. Kim, J. Di, R. H. Baughman, *Nano Lett.* **2016**, *16*, 7677.
- [253] J.-W. Lee, D.-C. Han, H.-J. Shin, S.-H. Yeom, B.-K. Ju, W. Lee, *Sensors* **2018**, *18*, 2996.
- [254] C. S. Yeo, H. Kim, T. Lim, H. J. Kim, S. Cho, K. R. Cho, Y. S. Kim, M. K. Shin, J. Yoo, S. Ju, S. Y. Park, *J. Mater. Chem. C* **2017**, *5*, 12825.
- [255] R. Wu, L. Ma, C. Hou, Z. Meng, W. Guo, W. Yu, R. Yu, F. Hu, X. Y. Liu, *Small* **2019**, *15*, 1901558.
- [256] J. Lee, D. W. Kim, S. Chun, J. H. Song, E. S. Yoo, J. K. Kim, C. Pang, *Adv. Mater. Technol.* **2020**, *5*, 2000073.
- [257] M. Hilal, J. I. Han, *IEEE Sens. J.* **2020**, *20*, 5146.
- [258] Y. Liang, F. Zhao, Z. Cheng, Q. Zhou, H. Shao, L. Jiang, L. Qu, *Nano Energy* **2017**, *32*, 329.
- [259] A. Balan, S. Ramasamy, *Sens. Rev.* **2018**, *38*, 412.
- [260] M. A. Yokus, J. S. Jur, *IEEE Trans. Biomed. Eng.* **2016**, *63*, 423.
- [261] C. Mattmann, F. Clemens, G. Tröster, *Sensors* **2008**, *8*, 3719.
- [262] E. P. Scilingo, F. Lorussi, A. Mazzoldi, D. De Rossi, *IEEE Sens. J.* **2003**, *3*, 460.
- [263] M. Yang, J. Pan, A. Xu, L. Luo, D. Cheng, G. Cai, J. Wang, B. Tang, X. Wang, *Polymers* **2018**, *10*, 568.
- [264] Z. Zhao, C. Yan, Z. Liu, X. Fu, L.-M. Peng, Y. Hu, Z. Zheng, *Adv. Mater.* **2016**, *28*, 10267.
- [265] Y. Li, Y. Li, M. Su, W. Li, Y. Li, H. Li, X. Qian, X. Zhang, F. Li, Y. Song, *Adv. Electron. Mater.* **2017**, *3*, 1700253.
- [266] M. Tas, Y. Altin, A. Celik Bedeloglu, *Diamond Relat. Mater.* **2019**, *92*, 242.
- [267] Y. Chen, B. Xu, J. Gong, J. Wen, T. Hua, C.-W. Kan, J. Deng, *ACS Appl. Mater. Interfaces* **2019**, *11*, 2120.
- [268] Y. Yu, Y. Zhai, Z. Yun, W. Zhai, X. Wang, G. Zheng, C. Yan, K. Dai, C. Liu, C. Shen, *Adv. Electron. Mater.* **2019**, *5*, 1900538.
- [269] X. Yue, Y. Jia, X. Wang, K. Zhou, W. Zhai, G. Zheng, K. Dai, L. Mi, C. Liu, C. Shen, *Compos. Sci. Technol.* **2020**, *189*, 108038.
- [270] L. Lu, Y. Zhou, J. Pan, T. Chen, Y. Hu, G. Zheng, K. Dai, C. Liu, C. Shen, X. Sun, H. Peng, *ACS Appl. Mater. Interfaces* **2019**, *11*, 4345.
- [271] J. Han, C. Xu, J. Zhang, N. Xu, Y. Xiong, X. Cao, Y. Liang, L. Zheng, J. Sun, J. Zhai, Q. Sun, Z. L. Wang, *ACS Nano* **2021**, *15*, 1597.
- [272] Z. Pan, J. Yang, L. Li, X. Gao, L. Kang, Y. Zhang, Q. Zhang, Z. Kou, T. Zhang, L. Wei, Y. Yao, J. Wang, *Energy Storage Mater.* **2020**, *25*, 124.
- [273] J. Zhao, H. Lu, Y. Zhang, S. Yu, O. I. Malyi, X. Zhao, L. Wang, H. Wang, J. Peng, X. Li, Y. Zhang, S. Chen, H. Pan, G. Xing, C. Lu, Y. Tang, X. Chen, *Sci. Adv.* **2021**, *7*, eabd6978.
- [274] Z. Tang, S. Jia, X. Shi, B. Li, C. Zhou, *Polymers* **2019**, *11*, 666.
- [275] X. Zhou, X. Xu, Y. Zuo, M. Liao, X. Shi, C. Chen, S. Xie, P. Zhou, X. Sun, H. Peng, *J. Mater. Chem. C* **2020**, *8*, 935.
- [276] X. Zhang, J. Li, W. Yang, B. Leng, P. Niu, X. Jiang, B. Liu, *ACS Appl. Mater. Interfaces* **2019**, *11*, 24459.
- [277] A. J. Bandodkar, J. Wang, *Trends Biotechnol.* **2014**, *32*, 363.
- [278] J. Zhang, S. Seyedin, S. Qin, P. A. Lynch, Z. Wang, W. Yang, X. Wang, J. M. Razal, *J. Mater. Chem. A* **2019**, *7*, 6401.
- [279] Y. Zhao, Q. Zhai, D. Dong, T. An, S. Gong, Q. Shi, W. Cheng, *Anal. Chem.* **2019**, *91*, 6569.
- [280] Y.-C. Wang, Z.-S. Sun, S.-Z. Wang, S.-Y. Wang, S.-X. Cai, X.-Y. Huang, K. Li, Z.-T. Chi, S.-D. Pan, W.-F. Xie, *J. Mater. Sci.* **2019**, *54*, 14055.
- [281] S. Wang, Y. Bai, X. Yang, L. Liu, L. Li, Q. Lu, T. Li, T. Zhang, *Talanta* **2020**, *214*, 120869.
- [282] A. Yang, Y. Li, C. Yang, Y. Fu, N. Wang, L. Li, F. Yan, *Adv. Mater.* **2018**, *30*, 1800051.
- [283] J. Rivnay, S. Inal, A. Salleo, R. M. Owens, M. Berggren, G. G. Malliaras, *Nat. Rev. Mater.* **2018**, *3*, 17086.

- [284] X. Wu, J. Feng, J. Deng, Z. Cui, L. Wang, S. Xie, C. Chen, C. Tang, Z. Han, H. Yu, X. Sun, H. Peng, *Sci. China: Chem.* **2020**, *63*, 1281.
- [285] Z. Zhu, C. Liu, F. Jiang, J. Liu, G. Liu, X. Ma, P. Liu, R. Huang, J. Xu, L. Wang, *J. Hazard. Mater.* **2021**, *411*, 125008.
- [286] A. Fakhruddin, W. Qiu, G. Croes, A. Devižis, R. Gegevičius, A. Vakhnin, C. Rolin, J. Genoe, R. Gehlhaar, A. Kadashchuk, V. Gulbinas, P. Heremans, *Adv. Funct. Mater.* **2019**, *29*, 1904101.
- [287] A. Fakhruddin, U. Shabbir, W. Qiu, T. Iqbal, M. Sultan, P. Heremans, L. Schmidt-Mende, *Adv. Mater.* **2019**, *31*, 1807095.
- [288] a) H. Zhang, J. A. Rogers, *Adv. Opt. Mater.* **2019**, *7*, 1800936; b) F. Zhao, D. Chen, S. Chang, H. Huang, K. Tong, C. Xiao, S. Chou, H. Zhong, Q. Pei, *J. Mater. Chem. C* **2017**, *5*, 531.
- [289] Z. B. Wang, M. G. Helander, J. Qiu, D. P. Puzzo, M. T. Greiner, Z. M. Hudson, S. Wang, Z. W. Liu, Z. H. Lu, *Nat. Photonics* **2011**, *5*, 753.
- [290] a) J. Liang, L. Li, X. Niu, Z. Yu, Q. Pei, *Nat. Photonics* **2013**, *7*, 817; b) Z. Wu, P. Li, Y. Zhang, Z. Zheng, *Small Methods* **2018**, *2*, 1800031.
- [291] B. O'Connor, K. H. An, Y. Zhao, K. P. Pipe, M. Shtein, *Adv. Mater.* **2007**, *19*, 3897.
- [292] A. R. Duggal, L. M. Levinson, European Patent, EP1180805A3, **2001**.
- [293] K.-J. Ko, H. B. Lee, H. M. Kim, G. J. Lee, S.-R. Shin, N. Kumar, Y. M. Song, J.-W. Kang, *Nanoscale* **2018**, *10*, 16184.
- [294] C. Murawski, K. Leo, M. C. Gather, *Adv. Mater.* **2013**, *25*, 6801.
- [295] S. Kwon, H. Kim, S. Choi, E. G. Jeong, D. Kim, S. Lee, H. S. Lee, Y. C. Seo, K. C. Choi, *Nano Lett.* **2018**, *18*, 347.
- [296] Q. Shan, C. Wei, Y. Jiang, J. Song, Y. Zou, L. Xu, T. Fang, T. Wang, Y. Dong, J. Liu, B. Han, F. Zhang, J. Chen, Y. Wang, H. Zeng, *Light: Sci. Appl.* **2020**, *9*, 163.
- [297] a) X.-K. Liu, W. Xu, S. Bai, Y. Jin, J. Wang, R. H. Friend, F. Gao, *Nat. Mater.* **2020**, *20*, 10; b) J. Song, K.-H. Kim, E. Kim, C.-K. Moon, Y.-H. Kim, J.-J. Kim, S. Yoo, *Nat. Commun.* **2018**, *9*, 3207; c) Y. Wada, H. Nakagawa, S. Matsumoto, Y. Wakisaka, H. Kaji, *Nat. Photonics* **2020**, *14*, 643; d) Y.-C. Wei, S. F. Wang, Y. Hu, L.-S. Liao, D.-G. Chen, K.-H. Chang, C.-W. Wang, S.-H. Liu, W.-H. Chan, J.-L. Liao, W.-Y. Hung, T.-H. Wang, P.-T. Chen, H.-F. Hsu, Y. Chi, P.-T. Chou, *Nat. Photonics* **2020**, *14*, 570.
- [298] Y.-H. Kim, S. Kim, A. Kakekhani, J. Park, J. Park, Y.-H. Lee, H. Xu, S. Nagane, R. B. Wexler, D.-H. Kim, S. H. Jo, L. Martínez-Sarti, P. Tan, A. Sadhanala, G.-S. Park, Y.-W. Kim, B. Hu, H. J. Bolink, S. Yoo, R. H. Friend, A. M. Rappe, T.-W. Lee, *Nat. Photonics* **2021**, *15*, 148.
- [299] G. Liang, M. Yi, H. Hu, K. Ding, L. Wang, H. Zeng, J. Tang, L. Liao, C. Nan, Y. He, C. Ye, *Adv. Electron. Mater.* **2017**, *3*, 1700401.
- [300] T. Sun, F. Xiu, Z. Zhou, C. Ban, T. Ye, Y. Ding, J. Liu, W. Huang, *J. Mater. Chem. C* **2019**, *7*, 1472.
- [301] Z. Zhang, X. Shi, H. Lou, X. Cheng, Y. Xu, J. Zhang, Y. Li, L. Wang, H. Peng, *J. Mater. Chem. C* **2018**, *6*, 1328.
- [302] Z. Zhang, K. Guo, Y. Li, X. Li, G. Guan, H. Li, Y. Luo, F. Zhao, Q. Zhang, B. Wei, Q. Pei, H. Peng, *Nat. Photonics* **2015**, *9*, 233.
- [303] H. Yang, C. R. Lightner, L. Dong, *ACS Nano* **2012**, *6*, 622.
- [304] C. Kortz, A. Hein, M. Ciobanu, L. Walder, E. Oesterschulze, *Nat. Commun.* **2019**, *10*, 4874.
- [305] a) M. Weston, A. D. Tjandra, R. Chandrawati, *Polym. Chem.* **2020**, *11*, 166; b) D. Galliani, L. Mascheroni, M. Sassi, R. Turrisi, R. Lorenzi, A. Scaccabarozzi, N. Stingelin, L. Beverina, *Adv. Opt. Mater.* **2015**, *3*, 1164.
- [306] L. Jiang, J. Wu, Q. Li, G. Deng, X. Zhang, Z. Li, K. Chen, K. S. Chiang, *J. Mater. Chem. C* **2019**, *7*, 6257.
- [307] W. Zhang, H. Li, W. W. Yu, A. Y. Elezzabi, *Light: Sci. Appl.* **2020**, *9*, 121.
- [308] X. Sun, J. Zhang, X. Lu, X. Fang, H. Peng, *Angew. Chem., Int. Ed. Engl.* **2015**, *54*, 3630.
- [309] a) H. H. Chou, A. Nguyen, A. Chortos, J. W. To, C. Lu, J. Mei, T. Kurosawa, W. G. Bae, J. B. Tok, Z. Bao, *Nat. Commun.* **2015**, *6*, 8011; b) J. Wang, M.-F. Lin, S. Park, P. S. Lee, *Mater. Today* **2018**, *21*, 508; c) H. F. Li, Z. J. Tang, Z. X. Liu, C. Y. Zhi, *Joule* **2019**, *3*, 613.
- [310] M. Liao, L. Ye, Y. Zhang, T. Chen, H. Peng, *Adv. Electron. Mater.* **2019**, *5*, 1800456.
- [311] J. Park, Y. Lee, M. H. Barbee, S. Cho, S. Cho, R. Shanker, J. Kim, J. Myoung, M. P. Kim, C. Baig, S. L. Craig, H. Ko, *Adv. Mater.* **2019**, *31*, 1808148.
- [312] a) H. Tan, Q. Lyu, Z. Xie, M. Li, K. Wang, K. Wang, B. Xiong, L. Zhang, J. Zhu, *Adv. Mater.* **2019**, *31*, 1805496; b) G. Chen, W. Hong, *Adv. Opt. Mater.* **2020**, *8*, 2000984.
- [313] a) H. Li, X. Sun, H. Peng, *ChemPhysChem* **2015**, *16*, 3761; b) S. Shang, Z. Liu, Q. Zhang, H. Wang, Y. Li, *J. Mater. Chem. A* **2015**, *3*, 11093.
- [314] J. Zhang, S. He, L. Liu, G. Guan, X. Lu, X. Sun, H. Peng, *J. Mater. Chem. C* **2016**, *4*, 2127.
- [315] a) X.-H. Li, C. Liu, S.-P. Feng, N. X. Fang, *Joule* **2019**, *3*, 290; b) Y. J. Ke, Y. Yin, Q. T. Zhang, Y. T. Tan, P. Hu, S. C. Wang, Y. C. Tang, Y. Zhou, X. L. Wen, S. F. Wu, T. J. White, J. Yin, J. Q. Peng, Q. H. Xiong, D. Y. Zhao, Y. Long, *Joule* **2019**, *3*, 858.
- [316] L. Xiao, H. Ma, J. Liu, W. Zhao, Y. Jia, Q. Zhao, K. Liu, Y. Wu, Y. Wei, S. Fan, K. Jiang, *Nano Lett.* **2015**, *15*, 8365.
- [317] T. Wu, T. Yin, X. Hu, G. Nian, S. Qu, W. Yang, *Adv. Opt. Mater.* **2020**, *8*, 2000031.
- [318] Y. Zhang, Z. Hu, H. Xiang, G. Zhai, M. Zhu, *Dyes Pigm.* **2019**, *162*, 705.
- [319] M. Yang, J. Pan, L. Luo, A. Xu, J. Huang, Z. Xia, D. Cheng, G. Cai, X. Wang, *Smart Mater. Struct.* **2019**, *28*, 085003.
- [320] H. Fan, Q. Li, K. Li, C. Hou, Q. Zhang, Y. Li, H. Wang, *Sci. China Mater.* **2020**.
- [321] X. Lu, Z. Zhang, X. Sun, P. Chen, J. Zhang, H. Guo, Z. Shao, H. Peng, *Chem. Sci.* **2016**, *7*, 5113.
- [322] a) Z. Wang, X. Wang, S. Cong, F. Geng, Z. Zhao, *Mater. Sci. Eng., R* **2020**, *140*, 100524; b) Y. Yue, H. Li, K. Li, J. Wang, H. Wang, Q. Zhang, Y. Li, P. Chen, *J. Phys. Chem. Solids* **2017**, *110*, 284; c) W. Zhang, H. Li, C. J. Firby, M. Al-Hussein, A. Y. Elezzabi, *ACS Appl. Mater. Interfaces* **2019**, *11*, 20378; d) S. Cong, Z. Wang, W. Gong, Z. Chen, W. Lu, J. R. Lombardi, Z. Zhao, *Nat. Commun.* **2019**, *10*, 678.
- [323] Y. Ke, J. Chen, G. Lin, S. Wang, Y. Zhou, J. Yin, P. S. Lee, Y. Long, *Adv. Energy Mater.* **2019**, *9*, 1902066.
- [324] a) H. Li, L. McRae, A. Y. Elezzabi, *ACS Appl. Mater. Interfaces* **2018**, *10*, 10520; b) H. Z. Li, J. M. Li, C. Y. Hou, D. Ho, Q. H. Zhang, Y. G. Li, H. Z. Wang, *Adv. Mater. Technol.* **2017**, *2*, 1700047.
- [325] a) H. Z. Li, C. J. Firby, A. Y. Elezzabi, *Joule* **2019**, *3*, 2268; b) S. Zhang, S. Cao, T. Zhang, J. Y. Lee, *Adv. Mater.* **2020**, *32*, 2004686; c) S. Cao, S. L. Zhang, T. R. Zhang, Q. F. Yao, J. Y. Lee, *Joule* **2019**, *3*, 1152.
- [326] H. Li, A. Y. Elezzabi, *Nanoscale Horiz.* **2020**, *5*, 691.
- [327] a) W. Zhang, H. Li, M. Al-Hussein, A. Y. Elezzabi, *Adv. Opt. Mater.* **2019**, *8*, 1901224; b) Z. Wang, X. Wang, S. Cong, J. Chen, H. Sun, Z. Chen, G. Song, F. Geng, Q. Chen, Z. Zhao, *Nat. Commun.* **2020**, *11*, 302.
- [328] a) C. Yan, W. Kang, J. Wang, M. Cui, X. Wang, C. Y. Foo, K. J. Chee, P. S. Lee, *ACS Nano* **2014**, *8*, 316; b) T. G. Yun, M. Park, D. H. Kim, D. Kim, J. Y. Cheong, J. G. Bae, S. M. Han, I. D. Kim, *ACS Nano* **2019**, *13*, 3141; c) H. Kai, W. Suda, Y. Ogawa, K. Nagamine, M. Nishizawa, *ACS Appl. Mater. Interfaces* **2017**, *9*, 19513; d) G. Yang, J. Ding, B. Yang, X. Wang, C. Gu, D. Guan, Y. Yu, Y.-M. Zhang, S. X.-A. Zhang, *J. Mater. Chem. C* **2019**, *7*, 9481; e) Y. Ding, M. A. Invernale, G. A. Sotzing, *ACS Appl. Mater. Interfaces* **2010**, *2*, 1588; f) M. A. Invernale, Y. Ding, G. A. Sotzing, *ACS Appl. Mater. Interfaces* **2010**, *2*, 296; g) H. Yu, M. Qi, J. Wang, Y. Yin, Y. He, H. Meng, W. Huang, *Electrochem. Commun.* **2019**, *102*, 31; h) T. An, Y. Ling, S. Gong, B. Zhu, Y. Zhao, D. Dong, L. W. Yap, Y. Wang, W. Cheng, *Adv. Mater. Technol.* **2019**, *4*, 1800473.

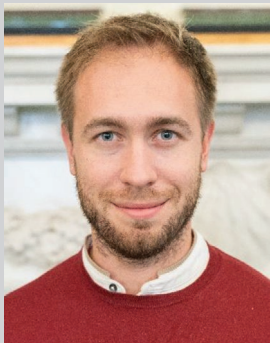
- [329] X. Chen, H. Lin, J. Deng, Y. Zhang, X. Sun, P. Chen, X. Fang, Z. Zhang, G. Guan, H. Peng, *Adv. Mater.* **2014**, *26*, 8126.
- [330] Y. Zhou, J. Fang, H. Wang, H. Zhou, G. Yan, Y. Zhao, L. Dai, T. Lin, *Adv. Electron. Mater.* **2018**, *4*, 1800104.
- [331] H. Fan, K. Li, X. Liu, K. Xu, Y. Su, C. Hou, Q. Zhang, Y. Li, H. Wang, *ACS Appl. Mater. Interfaces* **2020**, *12*, 28451.
- [332] S. Kwon, Y. H. Hwang, M. Nam, H. Chae, H. S. Lee, Y. Jeon, S. Lee, C. Y. Kim, S. Choi, E. G. Jeong, K. C. Choi, *Adv. Mater.* **2020**, *32*, 1903488.
- [333] Y. Fu, H. Wu, S. Ye, X. Cai, X. Yu, S. Hou, H. Kafafy, D. Zou, *Energy Environ. Sci.* **2013**, *6*, 805.
- [334] a) X. Wang, K. Jiang, G. Shen, *Mater. Today* **2015**, *18*, 265; b) J. Xu, G. Shen, *Nano Energy* **2015**, *13*, 131; c) J. S. Heo, J. Eom, Y.-H. Kim, S. K. Park, *Small* **2018**, *14*, 1703034.
- [335] X. Tao, *Acc. Chem. Res.* **2019**, *52*, 307.
- [336] T. Miyasaka, T. N. Murakami, *Appl. Phys. Lett.* **2004**, *85*, 3932.
- [337] a) Y. Liu, Y. Hu, J. Zhao, G. Wu, X. Tao, W. Chen, *Small* **2016**, *12*, 5074; b) J. Song, Y. Chen, K. Cao, Y. Lu, J. H. Xin, X. Tao, *ACS Appl. Mater. Interfaces* **2018**, *10*, 39839; c) J. Sun, Y. Huang, Y. N. Sze Sea, Q. Xue, Z. Wang, M. Zhu, H. Li, X. Tao, C. Zhi, H. Hu, *Mater. Today Energy* **2017**, *5*, 1; d) W. Zheng, X. Tao, B. Zhu, G. Wang, C. Hui, *Text. Res. J.* **2014**, *84*, 1791; e) X. Wang, X. Tao, R. C. H. So, L. Shu, B. Yang, Y. Li, *Smart Mater. Struct.* **2016**, *25*, 125022; f) J. Shen, X. Tao, D. Ying, C. Hui, G. Wang, *Text. Res. J.* **2013**, *83*, 730; g) J. Shen, C. Chui, X. Tao, *Biomed. Opt. Express* **2013**, *4*, 2925.
- [338] J. Yang, C. Yang, J. Cheng, A. Dai, T. Liu, Y. Yuan, K. Guo, D. Yuan, B. Wang, J. Lu, *Cell Rep. Phys. Sci.* **2020**, *1*, 100175.
- [339] J. Bae, Y. J. Park, M. Lee, S. N. Cha, Y. J. Choi, C. S. Lee, J. M. Kim, Z. L. Wang, *Adv. Mater.* **2011**, *23*, 3446.
- [340] X. Xu, S. Xie, Y. Zhang, H. Peng, *Angew. Chem., Int. Ed.* **2019**, *58*, 13643.
- [341] S. J. Varma, K. Sambath Kumar, S. Seal, S. Rajaraman, J. Thomas, *Adv. Sci.* **2018**, *5*, 1800340.
- [342] a) Z. Fang, J. Wang, H. Wu, Q. Li, S. Fan, J. Wang, *J. Power Sources* **2020**, *454*, 227932; b) L. Kong, C. Tang, H.-J. Peng, J.-Q. Huang, Q. Zhang, *SmartMat* **2020**, *1*; c) Y. Zhao, J. Guo, *InfoMat* **2020**, *2*, 866.



**Azhar Fakharuddin** obtained his Ph.D. in advanced materials from University Malaysia Pahang, where he worked on improving charge collection efficiency in dye-sensitized solar cells. He then joined the University of Konstanz, Germany, as an Alexander von Humboldt research fellow to work on interfaces and processes in perovskite/organic solar cells. He subsequently moved to IMEC, Belgium, to work on perovskite light-emitting diodes. Now, at the University of Konstanz, his current research focuses on novel materials and processes for high efficiency optoelectronic devices, mainly, solar cells and light-emitting diodes and their related device physics.



**Haizeng Li** is a full professor at the Institute of Frontier and Interdisciplinary Science, and the School of Energy and Power Engineering, Shandong University, China. He obtained his Ph.D. degree in 2016 from the State Key Laboratory for Modification of Chemical Fibers and Polymer Materials, China. He then started his postdoctoral research with Prof. Abdulhakem Y. Elezzabi at the University of Alberta, Canada. His current research interests include electrochromic devices, wearable electronics, energy storage, and radiative heat transfer.



**Nicola Gasparini** received his B.Sc. and M.Sc. in Chemistry and Organic Chemistry, and Photochemistry and Molecular Materials, respectively, from the University of Bologna, Italy. In 2014 he joined the group of Professor Brabec at the Institute of Materials for Electronics and Energy Technology of the Friedrich Alexander University Erlangen-Nürnberg and received his Ph.D. in 2017. After, he joined the King Abdullah University of Science and Technology as a postdoctoral fellow. Since September 2019, he is an independent researcher at Imperial College London, holding the Imperial College Research Fellowship. He made major scientific contributions regarding photophysical properties of organic semiconductors.



**Abd Rashid Bin Mohd Yusoff** completed his Ph.D. working with late Prof. Ivo Hümmelgen at Universidade Federal do Paraná, Brazil, in 2011. From 2011 to 2013, he was a postdoc fellow working with Prof. Jin Jang at Kyung Hee University. He then worked as a research professor in the same group until 2018, which was when he joined the Sêr SAM group at Swansea University as a senior research fellow with a focus on perovskite photovoltaics until 2020. He then moved to Pohang University of Science and Technology as a senior researcher focusing on perovskite functional and optoelectronic devices.



**Maria Vasilopoulou** received her degree in physics from the University of Athens and her Ph.D. in functional materials for nanolithography from the Chemical Engineering Department of the National Technical University of Athens. Then, she worked as a postdoctoral researcher at the National Center for Scientific Research Demokritos (NCSR-D), where she developed organic and inorganic materials for application as interfacial layers in organic solar cells and light-emitting diodes. She is currently a senior researcher at the Institute of Nanoscience and Nanotechnology of NCSR-D. Her research activity focuses on the area of the organic and halide perovskite optoelectronic devices.